

THE IMPLEMENTATION OF SIMULTANEOUS TRILATERATION TO MEASURE  
DYNAMIC THREE-DIMENSIONAL CONTOURS USING THE LASER BALL BAR

By

TONY L. SCHMITZ

A DISSERTATION PRESENTED TO THE GRADUATE SCHOOL  
OF THE UNIVERSITY OF FLORIDA IN PARTIAL FULFILLMENT  
OF THE REQUIREMENTS FOR THE DEGREE OF  
DOCTOR OF PHILOSOPHY

UNIVERSITY OF FLORIDA

1999

## ACKNOWLEDGMENTS

The author would like to thank his advisor, Dr. John Ziegert, for his ideas, patience, and affable administrative style. The author would also like to thank the renowned Dr. Jiri Tlusty, Dr. John Schueller, Dr. Ramakant Srivastava, and Dr. Ali Seireg for serving on his supervisory committee.

At the top of the list for "others to thank" are Dr. Chris Mize for his Laser Ball Bar design expertise and David Smith for his continual tutelage in the finer points of frequency analysis and signal processing. The author would also like to express his appreciation to Rick Glos of the Heidenhain Corporation for the loan of the KGM 101 Grid Encoder used for the STLBB verification tests.

This work was supported in part by the National Science Foundation under grant numbers DDM-935138 and DGE-9354980. Other financial support was supplied by the Department of Energy/National Academy of Engineering 1998 "Integrated Manufacturing Predoctoral Fellowship."

## TABLE OF CONTENTS

	page
ACKNOWLEDGMENTS.....	ii
LIST OF FIGURES.....	v
ABSTRACT .....	xi
CHAPTERS	
1 INTRODUCTION .....	1
2 LITERATURE REVIEW.....	9
Dynamic Measurements.....	9
Two-Dimensional Dynamic Measurement Tools .....	11
Software for Pre-Machining Contour Evaluation .....	18
3 DISPLACEMENT MEASURING INTERFEROMETRY.....	19
Introduction .....	19
Polarization.....	23
Interference.....	28
Heterodyne Interferometry .....	37
Fiber Optics in Interferometry .....	49
4 STLBB DESIGN .....	59
Tool Socket Joint .....	61
Tool Point Bracket .....	77
Optics Package.....	78
Error Budget.....	84
5 DYNAMIC MEASUREMENT RESULTS .....	106
Initialization Repeatability .....	106
2-D Measurements .....	108
Dynamic/Static Repeatability.....	117
2-D Contouring Accuracy .....	122

3-D Measurements .....	130
<b>6 MACHINING VERIFICATION .....</b>	<b>140</b>
Introduction .....	140
STLBB Results .....	141
Experimental Method .....	146
<b>7 CONCLUSIONS .....</b>	<b>152</b>
Completed Work .....	152
Future Work .....	155
APPENDICES	
A PROCESS CAPABILITY .....	158
B TRANSFORMATION OF BALL BAR COORDINATES INTO MACHINE COORDINATES .....	160
C SURFACE LOCATION ERROR IN MACHINING .....	162
LIST OF REFERENCES .....	193
BIOGRAPHICAL SKETCH.....	197

## LIST OF FIGURES

<u>Figure</u>	<u>page</u>
1-1. Laser Ball Bar .....	4
1-2. Trilateration Tetrahedron.....	4
1-3. Sequential Trilateration.....	6
1-4. Simultaneous Trilateration.....	6
2-1. Heidenhain Grid Plate.....	13
2-2. Magnetic Ball Bar.....	13
2-3. Ball Bar Contouring Error .....	15
2-4. Circular Path Section.....	15
2-5. Circular Test Setup.....	16
3-1. Plane Mirror Reflection .....	21
3-2. Polarizing Filter .....	24
3-3. Linearly Polarized Light.....	26
3-4. Left Circularly Polarized Light.....	26
3-5. Young's Double Slit Experiment .....	29
3-6. Michelson Interferometer.....	31
3-7. Twymann-Green Interferometer.....	33
3-8. Mach-Zehnder Interferometer.....	33
3-9. Alignment Accuracy .....	36

3-10.	Beat Phenomenon.....	39
3-11.	Heterodyne Phase Relationships .....	41
3-12.	Beat Frequency Shift .....	44
3-13.	Acousto-optic Modulator .....	46
3-14.	Zeeman Split .....	46
3-15.	Linear Displacement Interferometer.....	50
3-16.	Angular Measurement Setup.....	50
3-17.	Fiber Delivery/Collection.....	51
3-18.	Total Internal Reflection.....	51
3-19.	Refractive Index Profiles.....	54
3-20.	Single-mode Fibers.....	58
4-1.	Laser Ball Bar .....	60
4-2.	Simultaneous Trilateration .....	60
4-3.	Socket Diameter Constraints .....	63
4-4.	Tool Socket Spring Aid.....	65
4-5.	Castigliano Modeling.....	65
4-6.	Spring Aid Range of Motion.....	67
4-7.	Magnetic Flux Lines .....	67
4-8.	Static Free Body Diagram.....	70
4-9.	Friction Test Stand .....	73
4-10.	Calibration Couple.....	73
4-11.	Contact Area Geometry .....	76
4-12.	Tool Point Bracket .....	79

4-13.	Spring Scale Measurement	79
4-14.	Optics Package	80
4-15.	Optics Package Placement	80
4-16.	4-DOF Positioning Mechanism	83
4-17.	LBB Unsensed Length	85
4-18.	Sphere/Motion Misalignment	88
4-19.	LBB Interferometer Deadpath	88
4-20.	Initialization Fixture Offsets	92
4-21.	Castigliano Model Loading Conditions	95
4-22.	LBB Moment Calculation Sections	95
4-23.	Left Sphere Total Angular Rotation	98
4-24.	Cosine Error Due to Interferometer Rotation	98
4-25.	Moving Retroreflector Rotation	100
5-1.	LBB Initialization Fixture	107
5-2.	LBB Initialization Repeatability	107
5-3.	Heidenhain Grid Plate Setup	110
5-4.	STLBB Setup	110
5-5.	STLBB Verification Contours	112
5-6.	Angle Path Comparison (35 ipm, 0.1g)	114
5-7.	Angle Path Comparison (70 ipm, 0.5g)	114
5-8.	Step Path Comparison (70 ipm, 0.1g)	115
5-9.	Step Path Comparison (70 ipm, 0.5g)	115
5-10.	Sultan Path Comparison (35 ipm, 0.1g)	116

5-11.	Sultan Path Comparison (70 ipm, 0.1g) .....	116
5-12.	Square Path Comparison (70 ipm, 0.5g) .....	118
5-13.	Triangle Path Comparison (35 ipm, 0.1g) .....	118
5-14.	Circular Path Comparison (70 ipm).....	119
5-15.	Heidenhain Dynamic Repeatability Test .....	119
5-16.	STLBB Dynamic Repeatability Test .....	121
5-17.	Capacitance Probe Setup .....	121
5-18.	STLBB Angle Path (70 ipm, 0.1g).....	123
5-19.	STLBB Angle Path (70 ipm, 0.5g).....	123
5-20.	STLBB Square Path (70 ipm, 0.5g) .....	126
5-21.	STLBB Square Path Reversal (70 ipm, 0.5g).....	126
5-22.	STLBB Sultan Path (70 ipm).....	128
5-23.	STLBB Sultan Path Reversal (70 ipm).....	128
5-24.	STLBB Circular Path (35 ipm) .....	129
5-25.	STLBB Counter-Clockwise Circular Path (70 ipm).....	129
5-26.	STLBB Clockwise Circular Path (70 ipm, 0.1g).....	131
5-27.	STLBB Corkscrew 3-D Path and STLBB Measurement .....	131
5-28.	STLBB Hemisphere 3-D Path and STLBB Measurement .....	133
5-29.	STLBB Oblique Rectangle 3-D Path.....	133
5-30.	STLBB Oblique Circle 3-D Path.....	134
5-31.	STLBB Corkscrew 3-D Path Section.....	134
5-32.	STLBB Hemisphere 3-D Path Section .....	135
5-33.	STLBB Oblique Rectangle 3-D Path Section .....	135

5-34. STLBB Oblique Rectangle X-Y Plane .....	137
5-35. STLBB Oblique Rectangle X-Z Plane.....	137
5-36. STLBB Oblique RectangleY-Z Plane.....	139
6-1. Diamond Tool Path .....	142
6-2. X Reversal Error .....	142
6-3. Y Reversal Error .....	143
6-4. X-Y Gain Mismatch Error.....	143
6-5. Diamond Path Gain Mismatch Effect (70 ipm).....	145
6-6. Determination of $\Delta d$ (35 ipm Test) .....	145
6-7. Frequency Response Function (FRF) for 0.5" Diameter Endmill .....	147
C-1. Up/Down Milling .....	163
C-2. Undercut/Overcut in Milling .....	163
C-3. Cutting Forces in Down Milling.....	167
C-4. Y-Force Components ( $r < 1$ ) .....	167
C-5. System Frequency Response .....	169
C-6. Phasor Diagram ( $r < 1$ ).....	169
C-7. Y-Displacement Components ( $r < 1$ ) .....	171
C-8. Y-Force Components ( $r = 1$ ) .....	172
C-9. Phasor Diagram ( $r = 1$ ).....	175
C-10. Phasor Diagram ( $r > 1$ ).....	175
C-11. Undercut/Overcut/Undercut Transition.....	179
C-12. Simulation Flow Diagram .....	179
C-13. Part Geometry .....	182

C-14a. X Direction Direct Transfer Function.....	182
C-14b. Y Direction Direct Transfer Function.....	183
C-15. PTP Force Diagram.....	186
C-16. NC Path .....	186
C-17. Radial Asynchronous Error.....	190
C-18. D1/D2 Surface Location Error .....	190
C-19. Full Range Simulation (0.5" diameter tool, 3.25" overhang) .....	192
C-20. Full Range Simulation (0.75" diameter tool, 1.5" overhang) .....	192

Abstract of Dissertation Presented to the Graduate School  
of the University of Florida in Partial Fulfillment of the  
Requirements for the Degree of Doctor of Philosophy

THE IMPLEMENTATION OF SIMULTANEOUS TRILATERATION TO MEASURE  
DYNAMIC THREE-DIMENSIONAL CONTOURS USING THE LASER BALL BAR

By

TONY L. SCHMITZ

May 1999

Chairman: Dr. John Ziegert

Major Department: Mechanical Engineering

Computer numerically-controlled (CNC) multi-axis machine tools are an integral part of modern manufacturing. These machines operate in an overall open-loop mode (i.e., although the positions of the individual axes are servo-controlled, the actual spatial coordinates of the tool or end-effector are unknown). Since the machining process is open loop, the ability to monitor the cutting tool/workpiece positional relationship and predict the final part dimensions is limited.

At this time there are no pre-process measurements which can be performed to accurately predict the final dimensions of a machined part. This produces a fundamental gap in the ability to model the machining process. Although static measurements may be performed on a given machine tool to characterize its (static positioning) accuracy, the final part dimensions are a function of the machine tool's dynamic spatial positioning accuracy. A tool which could dynamically measure the tool position along three-

dimensional contours to micrometer accuracy would close this gap and permit rapid verification of CNC part programs.

This research describes the design and construction of a sensor, the simultaneous trilateration laser ball bar system (STLBB system), which has the capability of measuring these 3-D contours to micrometer-level accuracy. The data obtained from these 3-D measurements is useful for the evaluation of the controller performance during contouring and the measurement of the relative contributions of both quasi-static (geometric) positioning errors and controller errors to the part dimensional errors. The ability to verify the CNC part program without machining a series of test parts is another benefit of this sensor. This reduces scrap and increases the manufacturing process efficiency, especially in situations where machining time is high and material is expensive (e.g., the aerospace industry).

In order to completely close the open loop machining process, the effects of forced vibrations caused by the steady-state cutting forces on the final workpiece dimensions are also investigated. A simulation is included which computes the surface location errors introduced during the cutting process. These errors may then be applied as a type of post-processing filter to the STLBB dynamic path measurements to accurately predict the final machined part dimensions.

## CHAPTER 1 INTRODUCTION

Computer numerically-controlled (CNC) multiple-axis machine tools are an integral part of modern manufacturing. These machines operate in an overall open-loop mode (i.e., although the positions of the individual axes are servo-controlled, the actual spatial coordinates of the tool or end-effector are unknown). In continuous-path NC systems, there is contact between the cutting tool and workpiece while up to five axes are in motion. Therefore, the final workpiece dimensions are directly related to the positional relationship between the tool and workpiece. Since the machining process is essentially open loop (the tool/workpiece contact may loosely close the positional loop and affect the overall machine tool stiffness), the ability to monitor this relationship and predict the final part dimensions is limited.

At this time there are no pre-process measurements which can be performed to accurately predict the final dimensions of a machined part. This produces a fundamental gap in the ability to model the machining process. Although static measurements may be performed on a given machine tool to characterize its (static positioning) accuracy, the final part dimensions are a function of the machine tool's dynamic spatial positioning accuracy. A tool which could dynamically measure the tool position along three-dimensional contours to micrometer accuracy would close this gap and permit rapid verification of CNC part programs. This research describes the design and construction of a sensor, the simultaneous trilateration laser ball bar system (STLBB system), which

has the capability of measuring these 3-D contours. The data obtained from the 3-D measurements is useful for the evaluation of the controller performance during contouring and the measurement of the relative contributions of both quasi-static positioning errors and controller errors to the part dimensional errors. The ability to verify the CNC part program without machining a series of test parts is another benefit of this sensor. This reduces scrap and increases the manufacturing process efficiency, especially in situations where machining time is high and material is expensive (e.g., the aerospace industry).

The ability to characterize the accuracy of 3-D contours prior to machining could also have far-reaching effects in the field of process capability. In modern industry, there is a "growing interest in quantifying the ability of a process to satisfy customer requirements" [1]. A process capability study provides information on the existing process performance (e.g., producing dimensionally correct parts by machining) with respect to the pre-defined requirements (e.g., the engineering drawings). It can also suggest possible process improvements and allow design engineers to select an appropriate process to meet the accuracy requirements. A brief overview of the statistically-based process capability theory is given in Appendix A.

A process capability study of a given machine tool, for example, may be completed to isolate the amount of process variation contributed solely by the machine. Such a study would attempt to remove other known variation sources (i.e., setup, operator influence, workpiece material, maintenance, pallet errors) and therefore, concentrate on the variations inherent to the machining process (i.e., thermal fluctuations, geometric errors, spindle errors, cutting force errors). In a typical study, a given number of parts (at least 50 recommended) are machined over some thermal duty cycle under normal machining

conditions [1]. These parts are then measured, a process stability analysis performed, and one or more process capability indices (PCIs) utilized to predict future performance [2].

The necessity of machining and measuring such a large number of parts makes this process costly and time consuming. The STLBB system could be used to dynamically measure the corresponding contours in real time over the same thermal duty cycle. This would eliminate the cost of material and tooling and halve the total process time. With the inclusion of possible spindle and cutting force errors in the STLBB analysis, the process capability of a machine tool could be evaluated without cutting a single test part.

The STLBB system is based on the laser ball bar (LBB), a precision linear displacement measuring device developed at the University of Florida by Ziegert and Mize [3]. It consists of a two-stage telescoping tube with a precision sphere mounted at each end. A heterodyne displacement measuring interferometer is aligned inside the tube and measures the relative displacement between the two sphere centers (see Figure 1-1). The LBB has been shown to be accurate to sub-micrometer levels during static measurements [4].

Once initialized, the LBB uses trilateration to measure the spatial coordinates of points along a CNC part path. The six edges of a tetrahedron formed by three base sockets (attached to the machine table) and a tool socket (mounted in the spindle) are measured and, by geometry, the spatial coordinates of the tool position in the LBB coordinate system are calculated. The three lengths between the three base sockets ( $L_{B1}$ ,  $L_{B2}$ ,  $L_{B3}$ ) shown in Figure 1-2 are measured once and remain fixed during the motion of the tool socket. The three base-to-tool socket lengths (denoted  $L_1$ ,  $L_2$ ,  $L_3$  in Figure 1-2) are measured during execution of the applicable CNC part program. Once the coordinates

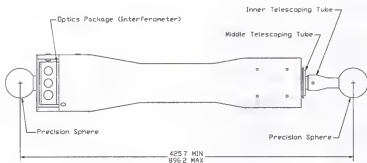


Figure 1-1: Laser Ball Bar

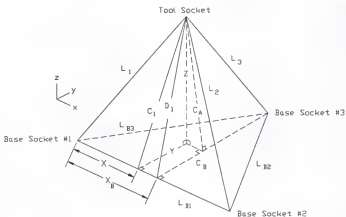


Figure 1-2: Trilateration Tetrahedron

in the LBB frame have been determined, they may be transformed into machine coordinates using the homogeneous transformation matrix (HTM) between the LBB and machine coordinate systems. A brief outline of HTMs and the method used for the determination of the transformation between the LBB and machine coordinates are given in Appendix B.

Previous research using the LBB has focused on sequential trilateration and quasi-static measurements (i.e., motion is stopped to take the measurements). In sequential trilateration, the same part path is traversed three times, measuring the lengths of one base-to-tool socket leg at a number of static points during each repetition. The setup for sequential trilateration is shown in Figure 1-3. This method requires a spatially repeatable measurement trigger since the tool socket must be in exactly the same position (for a given point) for each of the three measurements. When quasi-static measurements are performed, the machine repeatability governs the accuracy of the measurement trigger and, therefore, the measured coordinates. For most machine tools, the short term static repeatability is substantially better than the absolute positioning accuracy, and this process yields satisfactory results. However, for dynamic path measurements, the spatially repeatable measurement trigger is difficult to implement.

The parametric error map for a 3-axis milling machine was constructed by Kulkarni using both the quasi-static sequential trilateration LBB technique and the methods described in the ASME B5.54 Standard, "Methods for Performance Evaluation of Computer Numerically Controlled Machining Centers" [5]. The agreement between the two results verified the LBB technique [6]. A second sequential trilateration study was completed by Srinivasa which measured the positioning errors on a 2-axis turning

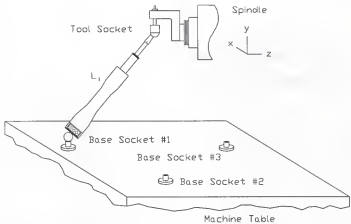


Figure 1-3: Sequential Trilateration

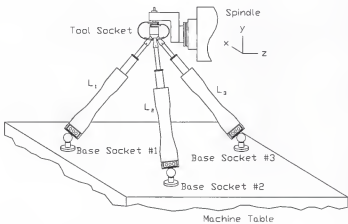


Figure 1-4: Simultaneous Trilateration

center over a thermal duty cycle and correlated these errors with the temperature gradients within the machine tool using a neural network. A PC-based error compensation system was then used to compensate for the errors predicted by the neural network [7].

The above methods give a rapid, efficient way to measure the quasi-static errors of a machine tool and thus evaluate its static positioning accuracy. However, these methods do not characterize the dynamic positioning accuracy of the machine tool.

This research focuses on simultaneous trilateration, where three LBBs ride on a single sphere at the tool point to completely define all three base-to-tool socket lengths with one execution of the CNC program. Since all three leg lengths are captured at once, the measurement trigger need not be spatially repeatable, and this method is better suited to dynamic measurements (see Figure 1-4). In previous work, the feasibility of using the LBB as a dynamic measuring device was demonstrated [8]. Sequential trilateration was implemented to measure the coordinates of a 2-D circular contour using one LBB and the encoder feedback signal as a measurement trigger. Measurements obtained using an independent device verified the LBB results.

The work completed in this research includes the implementation of simultaneous trilateration to measure 3-D dynamic part paths to micrometer level accuracies. Other sub-tasks which were completed are the novel design of a tool socket/joint to support the 3 LBBs, the optics/fiber-optics design and component selection for the linear displacement interferometers inside each LBB, a redesign of the individual LBBs with respect to previous models (e.g., extended and retracted size, optics configuration, optics positioning system), 2-D verification of the STLBB results, 3-D contour measurements using the STLBB, cutting force experiments to quantify the surface location error which results

from forced vibrations of the cutting tool, machining verification tests and software development including NC programming.

## CHAPTER 2 LITERATURE REVIEW

Although there are no other systems currently available to measure three-dimensional dynamic contours to micrometer-level accuracy, the usefulness of dynamic measurements and tools which permit the accurate, dynamic measurement of two-dimensional paths have been widely discussed in literature. Methods of dynamic data capture, data evaluation, and the currently available tools which provide 2-D measurements will be outlined in the following paragraphs. Additionally, recent releases of computer software which focus on pre-machining CNC contour evaluation will be discussed briefly.

### Dynamic Measurements

Geometric calibration of machine tools using the procedures outlined in national and international standards can be costly and time consuming, especially for large machines requiring the measurement of all possible geometric errors (21 for a 3-axis machine). However, the importance of calibration to machine tool builders and users cannot be overlooked. For builders and users alike, calibration procedures attempt to provide a means of comparing the actual machine tool performance with the product specifications. Users can also use calibration to check and maintain the required performance of the machine tool during daily production.

Typical calibration standards call for static measurements (commonly using a laser interferometer) along a single axis with a position-based measurement trigger (i.e., the machine axis is stopped at regular or random intervals during measurements). The time required to stop, settle, make several measurements (to average out vibrations), and start again is considerable when several static measurements are to be made. In order to minimize this time, the number of measurement points taken is limited. For such coarse measurement intervals, cyclic errors with a high spatial frequency (such as errors associated with leadscrew pitch) may be overlooked. If the data is to be used for compensation, this can be a major issue.

In research described in [9] and [10], a time-based measurement trigger was imposed on a linear displacement interferometer system to collect calibration data dynamically along a single axis. The dynamic data capture reduced the overall measurement time and the ability to measure at high temporal frequencies yielded high spatial resolution.

In this work, a Renishaw™ laser interferometer system was used to measure axis position, straightness, or angular (pitch and yaw) errors at sampling rates up to 5 kHz. Unlike static measurements, however, the raw dynamic data required extensive processing to obtain useful information. For position errors, a line was fit to the dynamic data which represented the nominal axis positions for a constant velocity axis motion. The error was the difference between the measured positions and constant velocity positions at appropriate time steps. To calculate the straightness errors, a line was again fit to the data to remove any misalignment between the laser and optics. This line was then subtracted from the original data to give the straightness errors.

Using the dynamic procedure, the measurements were found to be more "noisy" than the results from static tests. This is a direct consequence of the absence of averaging in the dynamic tests (i.e., in static tests, several measurements are taken at each position and the results averaged). The papers suggest that the dynamic data should be processed to remove the "random" high frequency components (although it may be argued that there are no random components, only unexplained ones). Two post-process software methods were used to massage the data: averaging and lowpass filtering. The filter implemented was a digital representation of a 3<sup>rd</sup> order Butterworth lowpass filter. The cutoff frequency was user-selected in the software. The averaging was implemented using the "boxcar" method. In this technique, the data was split into a series of blocks and the mean of each block computed. The user was prompted for the time interval of the individual data blocks for this method.

Dynamic positioning tests at various sampling frequencies and axis velocities were compared to static measurements. Close agreement between the two suggested that dynamic measurements are a valid way to complete machine tool calibration.

#### Two-Dimensional Dynamic Measurement Tools

A product capable of 2-D dynamic measurements has been commercialized by the Heidenhain Corporation. The Heidenhain grid plate system is composed of an optical grid plate with a waffle-type grating of closely spaced lines (4  $\mu\text{m}$  signal period) and a non-contact scanning head which can measure translations in two directions. The grid plate is attached to a mounting base. This base is mounted in the plane to be measured (on an X-Y table, for instance) and the scanning head is fixed perpendicular to the plate

(on the Z axis attached to the spindle, for example). This system measures the relative planar motion of the two bodies for any type of curvilinear path in the plane of the mounting base and within the area of the optical grid plate (see Figure 2-1). The recorded motions allow the user to observe the dynamic effects of the machine tool's performance on the CNC tool path.

Common single-axis measurements (e.g., positioning, straightness, reversal), as well as the circular test, were performed in [11] using the Heidenhain grid plate. The straightness of a short path (100 mm) was measured by moving in a single direction (at 4 m/min) and observing the lateral deviations of the scanning head. For the machine tool used in this research, a total straightness error of 0.6  $\mu\text{m}$  was found. The reversal error of a single axis was also measured for a single traverse and over a three hour duty cycle to test thermal effects. The circular test (circle commanded in NC controller and actual path measured) was performed to see the deviation of the recorded path from a true circle (10 mm diameter circle with a feed rate of 6 m/min). An average error in the path diameter as well as high frequency radial oscillations were detected. The cornering test was also completed to check possible overshoot or undershoot. An overshoot of 0.02 mm was seen at 6 m/min for the machine tool in question. The results of all these tests showed that the grid plate encoder is a valuable tool for examining the dynamic performance of a machine tool.

In a related paper [12], the Heidenhain grid plate encoder was used, along with appropriate models, to optimize the dynamic performance of fast feed drives on high-speed machine tools. A model was developed to represent a particular three-axis machine tool. The machine tool was modeled as serial connections of the motor, ballscrew, table

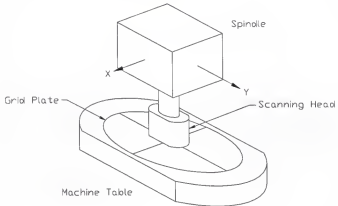


Figure 2-1: Heidenhain Grid Plate

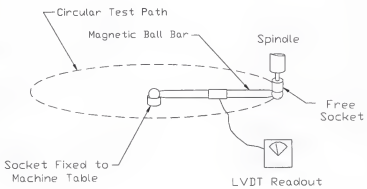


Figure 2-2: Magnetic Ball Bar

and structure in two axes (X, Y), while the Z axis dynamics were neglected. Cornering motions in the X-Y plane were then simulated in software and measured (10 m/min, 1 m/s<sup>2</sup>) using the grid plate system. The axis gains were then adjusted according to the simulation and measurement results. The conclusion was that the limiting factor was the flexibility of the machine tool structure, rather than motor tuning issues.

Another tool commonly used to perform the circular test is the magnetic ball bar. The ball bar is a device which measures small changes in its lengths using a precision transducer (such as an LVDT) (see Figure 2-2). As part of a complete calibration of a three-axis vertical spindle machine tool, the 2-D contouring errors were measured by the circular test using a magnetic ball bar in [13]. A 150 mm radius circular path (4 m/min tangential velocity) was programmed into the controller and the deviations from this path recorded. The two most common forms of contouring error were recognized: path radius error and reversal spikes at a change in quadrant (see Figure 2-3). Typical motion for a section of this circular path is shown in Figure 2-4. The causes of the errors shown in Figure 2-3 were attributed to the servo lag in the controller and the time delay of the acceleration/deceleration control.

By reducing the controller time constant from 50 to 8 ms and adding feed forward velocity control and nonlinear friction compensation, the path errors were minimized. This off-line servo tuning improved the 2-D contouring performance at this local area in the work volume significantly (approximately 20 times improvement at 2 m/min).

Another body of work [14] also included attempts to identify the major motion error sources on CNC machines using the 2-D circular test. The test setup is shown in Figure 2-5. In this research, the motion error signal (proportional to the change in path

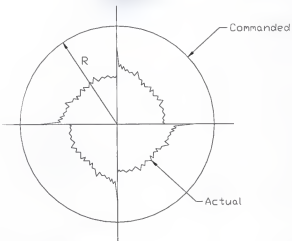


Figure 2-3: Ball Bar Contouring Error

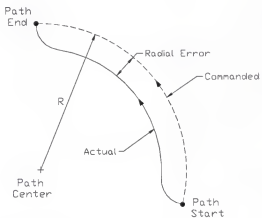


Figure 2-4: Circular Path Section

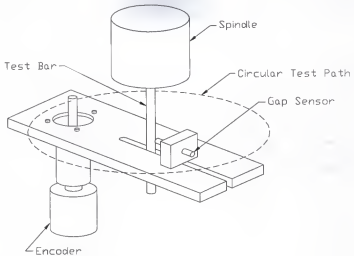


Figure 2-5: 2-D Circular Test Setup

radius from ideal) were taken to be linearly related to the motion error sources. These motion error signals were divided into those which are directional dependent and those which are nondirectional dependent. Directional error patterns are said to be a result of such errors as backlash and loop gain discrepancy. Nondirectional errors result from such sources as squareness, straightness, and uniform positioning errors.

By performing two circular tests in opposite directions, nondirectional dependency was ascertained by averaging the two signals. The directional errors were found by subtracting the averaged record from the original signals. A frequency analysis was then used to find the individual nondirectional errors such as uniform positioning, straightness and squareness errors. A weighted residual method was implemented to identify the directional errors such as backlash and loop gain mismatch.

Aside from machine tool calibration, there are other applications which require dynamic measurements. The laser interferometer provides an attractive method of completing vibration measurements because the measurements are non-contact and have a high resolution. If these measurements are to be performed on large bandwidth systems, high-frequency dynamic data capture is necessary.

An example of this high-frequency, dynamic measurement requirement is the calibration of piezoelectric transducers (PZT). PZTs are typically used in the control systems of lithography and diamond turning to correct rapidly changing errors or provide fine position resolution. In these cases, the frequency response and bandwidth of the transducer must be well defined. Dynamic measurements can provide this information.

Software for Pre-Machining Contour Evaluation

The attractiveness of verifying CNC code prior to machining a test part has not gone unnoticed in the manufacturing community. Several computer-aided manufacturing (CAM) software programs which boast of this capability have been released. Although such programs add collision protection and other NC error checks, as well as tool path optimization, to the manufacturing process, they cannot predict part dimensional errors due to such sources as thermal gradients, geometric positioning errors, machine tool dynamics, and/or cutting force effects. A sensor such as the STLBB system is required to account for these error sources.

## CHAPTER 3

### DISPLACEMENT MEASURING INTERFEROMETRY

#### Introduction

A logical starting point in a discussion of displacement measuring interferometry is a brief review of the fundamentals of light theory, polarization, and interference. Light is a transverse electromagnetic wave with well-established relationships among the velocity, wavelength, and frequency. The velocity of light in a given medium,  $v$ , is related to the speed of light in vacuum,  $c$ , by the index of refraction,  $n$ . This relationship is given in Equation 3-1. A similar relationship can be seen between the wavelength of light in a given medium,  $\lambda$ , and the wavelength in vacuum,  $\lambda_0$ . See Equation 3-2. At standard temperature and pressure (temperature = 20°C, pressure = 760 mm Hg, relative humidity = 50%), the index of refraction of air is 1.000271296 [15]. The velocity of light in air is, therefore, slightly less than the velocity of light in vacuum.

$$v = c / n, \quad \text{where } c = 2.99792458e8 \text{ m/s} \quad (3-1)$$

$$\lambda = \lambda_0 / n \quad (3-2)$$

Additionally, the velocity is related to the wavelength and frequency,  $f$ , of light as shown in Equation 3-3 [16]. An examination of the electromagnetic spectrum reveals a range of frequencies from 3 Hz (AC power radio waves) to 3e24 Hz (gamma rays) with

corresponding wavelengths of  $1e8$  m to  $1e-16$  m. The visible spectrum is generally characterized by wavelengths between 380 nm (violet) and 770 nm (red) [17].

$$\nu = \lambda f \quad (3-3)$$

The relationships given in Equations 3-2 and 3-3 allude to the wave nature of light (i.e., when speaking of the wavelength of light). However, the wave model cannot always predict the behavior of light. Light behavior is better described by a theory which incorporates both wave and particle models, generally referred to as the wave-particle duality. In some situations, the wave theory is useful to describe the behavior of light (e.g., interference) and in others the particle nature is more applicable (e.g., photoelectric effect) [17]. The theory of quantum electrodynamics (QED) incorporates the dual nature of light and successfully predicts all types of light behavior (e.g. diffraction, reflection, refraction, partial reflection, etc.) using probability theory.

As an example, consider the simple case of reflection off a plane mirror. Let there be a very low intensity, single frequency (monochromatic) source that emits only one particle of light, or photon, at a time. This light is incident on a plane mirror with a photomultiplier positioned as shown in Figure 3-1 to detect any reflected photons. Only photons which actually reflect off the mirror surface will be considered (i.e., any photons which travel directly from the source to the detector will be neglected).

The photons are free to travel in any path from the source to the detector, and they actually do. A separate 'probability arrow' can be drawn to represent each possible path that a photon may take from the detector to the source. The length of the 'arrow' for

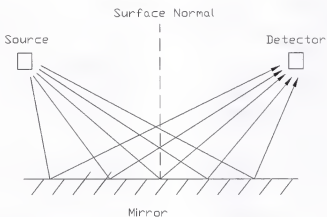


Figure 3-1: Plane Mirror Reflection

each path represents the probability that a photon would take this particular path. The angular orientation of the 'arrow' symbolizes the time it takes for the photon to reach the detector. For example, a longer path will be represented by an 'arrow' which is rotated clockwise by several degrees (i.e., the second hand on a stopwatch after several seconds from vertical), while the 'arrow' for a very short path would be nearly vertical (i.e., the second hand is near vertical when the count in seconds is near zero).

Since the photons have an equal probability of following any path, all arrows have equal lengths. The orientations of the individual arrows will vary, however, since the path lengths are not equal. A photon which travels straight down to the mirror and then to the detector has a longer path length than one which reflects off the mirror center. If the arrow orientations represent the time of flight, the path taken will determine the arrow direction. The implementation of vector addition to sum the individual arrows from all possible paths gives a large resultant arrow. The length of the arrow is the probability amplitude and a long arrow implies an event is likely to occur. Therefore, QED predicts light will indeed reflect off the mirror. Furthermore, the magnitude of the resultant arrow is most strongly influenced by the arrows which represent paths near the middle of the mirror. Since paths near the center of the mirror take approximately the same time and, therefore, have basically the same orientation, it is these paths of least distance (and time) that most affect the final arrow length and high probability of reflection. Therefore, the assumption that light travels in paths of least time (i.e., the law of reflection which states that the incident angle equals reflected angle) is an acceptable approximation, although not an exact picture of light behavior [18].

Polarization

Light can be described as a transverse electromagnetic wave with fluctuating electric (E) and magnetic (B) fields which are mutually perpendicular to one another, as well as the direction of propagation of the wave. The polarization of the wave is defined, by convention, as the direction of the electric field vector (since this is the more easily measurable quantity). If this vector lies in a plane for all temporal and spatial positions, the light is said to be linearly polarized.

Randomly polarized (or unpolarized) light, on the other hand, has an E vector which does not lie in a single plane and does not vary spatially in a repeatable manner. This unpolarized light, such as sunlight or the light emitted by a hot filament, may be linearly polarized by passing the light through a Polaroid<sup>TM</sup>, or polarizing filter. This dichroic material, originally developed by E. H. Land, allows one polarization component (e.g., the vertical) to pass through and absorbs all others. The transmission axis (the vertical axis in this example) is defined as the direction in the material which suppresses vibrations and, therefore, absorbs little of the light energy. The direction orthogonal to the transmission axis blocks the light polarized in this direction by allowing the material electrons to vibrate when excited by the light, thereby absorbing the light energy. Figure 3-2 represents the case of absorbing horizontal polarizations and transmitting the vertical. Other methods of producing polarized light include reflection, scattering and birefringence [17].

The reader may be aware that quality sunglasses have lenses made of dichroic polarizing material. Light reflected from a horizontal surface, such as the highway, has a

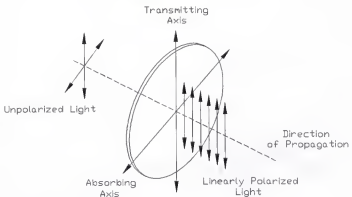


Figure 3-2: Polarizing Filter

polarization state which is mostly linearly polarized in the horizontal plane. The lenses, with a vertical polarization axis, almost completely absorb the horizontal orientation and substantially reduce glare.

Next, consider two, equal-magnitude waves with perpendicular polarizations (electric field vectors  $E_1$  and  $E_2$  perpendicular) and identical directions of propagation. If these two waves are in phase, the resultant polarization, found by the vector addition of  $E_1$  and  $E_2$ , will lie in a plane oriented at  $45^\circ$  with respect to each of the original  $E$  fields. This is also termed linearly polarized light and is shown in Figure 3-3.

If these two, equal-magnitude waves are now shifted in phase by  $90^\circ$  relative to one another, the resultant vector no longer lies in a single plane. Instead, it traces out a helical path along the direction of propagation. This situation is defined as circular polarization. The electromagnetic wave is termed right circularly polarized if the helical path is clockwise as one looks *back* along the direction of propagation and left circularly polarized if the direction is counter-clockwise. Figure 3-4 shows an example of left circular polarization. Viewed head-on, the polarization vector traces out the Lissajous figure of resultant electromagnetic field vibration [17]. In this case, the figure is a circle. In the more general case, when the phase shift is neither  $0^\circ$  or  $90^\circ$  (or an integer multiple) or the magnitudes of the two electric field magnitudes are not equal, the polarization is defined as elliptical. In this instance, the polarization vector traces an elliptical path along the direction of propagation (i.e., the Lissajous figure is an ellipse). Depending on the phase difference, the tip of the resultant electric field vector may trace clockwise or counter-clockwise paths.

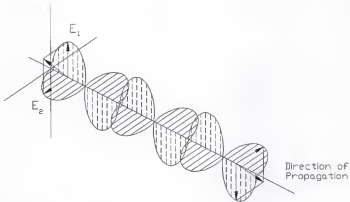


Figure 3-3: Linearly Polarized Light

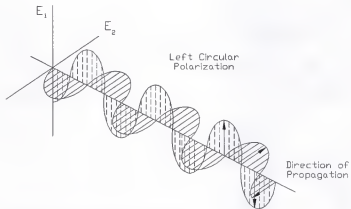


Figure 3-4: Left Circularly Polarized Light

In many situations, it is desired to change the polarization of light by shifting one of the two waves with orthogonal electric field vectors relative to the other, as described previously. A birefringent material is particularly useful in this instance. Birefringent materials exhibit a dependence of the index of refraction on the direction of polarization of the incident electromagnetic wave. Notice from Equation 3-1 that a higher refractive index yields a slower velocity of propagation in the given material. Therefore, when the two waves with perpendicular polarization enter the material (with the optical axis parallel to one polarization), one wave will travel slower than the other (due to a higher  $n$ ) and introduce some phase shift between the two on exit from the material.

In order to convert linearly polarized light to circular polarized (or vice versa), a  $90^\circ$  phase shift must be introduced in one axis relative to the other. The name for the birefringent optic which completes this conversion, a quarter-wave plate (or quarter-wave phase retarder), is derived from the  $\frac{1}{4}$  cycle delay which results from this  $90^\circ$  phase shift. The quarter-wave plate has defined two optical axes, which are mutually orthogonal. The slow axis introduces a  $90^\circ$  phase shift (due to a higher index of refraction) in the light (of appropriate wavelength) which travels along this polarization relative to light which propagates along the fast axis polarization.

As a final word in this brief outline of polarization, it should be noted that an elegant representation of the polarization of electromagnetic waves is given by the Jones vector notation. The Jones vector is a  $2 \times 1$  column vector which denotes the polarization state of a wave using real and imaginary values. Also, the polarizing elements described previously may be modeled by  $2 \times 2$  matrices. The matrix pre-multiplication of the Jones vector by the matrices of the polarizing elements which act on the wave gives the final

polarization state of the original wave. The reader is referred to [17] for more information on this topic.

### Interference

The basis for interferometry is the interference of two or more electromagnetic waves in space. The magnitude of the resultant electric field is defined by the principle of linear superposition [16]. When two coherent (constant initial phase), non-orthogonal waves (for simplicity, assume identical polarizations) arrive at the same point, their phase relationship determines the final magnitude. Constructive interference occurs when the waves are in phase and gives a total magnitude equal to the sum of the individual magnitudes. Destructive interference takes place when the waves are  $180^\circ$  out of phase. The resultant amplitude is the difference between the two individual amplitudes. For equal initial amplitudes, total cancellation occurs.

A popular example of this two-source interference is shown in Figure 3-5. In this experiment, first performed by Thomas Young in 1802, a coherent monochromatic source is incident on two narrow slits in a screen. This source is typically taken to be a point source which has wavefronts, or loci of points with the same phase, which are ideally spherical in shape. The two light paths which show through the two narrow (ideally point source) slits also exhibit coherent spherical wave fronts. A screen placed in the path of these two waves shows alternating bright and dark bands. This is an interference pattern which demonstrates both constructive (bright bands) and destructive (dark bands) interference between the light waves emitted from the two slits.

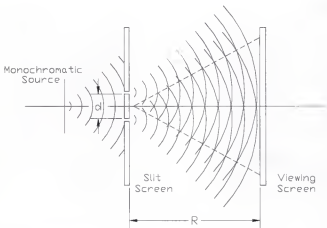


Figure 3-5: Young's Double Slit Experiment

The monochromatic wavelength of the source may then be calculated, according to Equation 3-4, by measuring the distance between the slits ( $d$ ), the distance between the viewing screen and the slits ( $R$ ), and the distance between adjacent bright band centers ( $\delta$ ). For completeness, it should be noted that the effects of diffraction (also an interference phenomenon), or bending of the light waves around the slit of finite width in the screen, have been neglected in this simple analysis.

$$\lambda = d \delta / R \quad (3-4)$$

The first displacement measuring interferometer was developed by Albert Michelson in 1881 [17]. In this experiment, light was incident on a partially silvered mirror or beam splitter (glass with a thin silver coating). This beam splitter allowed some of the light to pass through and reflected the rest. The reflected portion of the light traveled to a moveable mirror mounted on a fine pitch micrometer. The transmitted light passed through a second glass plate with the same thickness as the beam splitter to a fixed, reference mirror. The second plate, or compensator plate, was necessary to ensure that both the reflected and transmitted light traveled through an equal distance in glass, referred to as the optical path length (OPL). When the mirror mounted on the micrometer was translated relative to the fixed mirror (without changing its angular orientation), light to dark (uniform intensity) transitions due to constructive and destructive interference were seen once the beams had recombined at the beam splitter, as shown in Figure 3-6. A relative displacement of one-half the wavelength of the source light ( $\lambda/2$ ) produced a light-dark-light transition, or fringe, at the viewing position. A light-dark-light transition

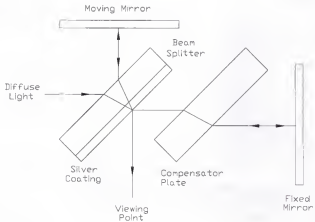


Figure 3-6: Michelson Interferometer

occurred for a  $360^\circ$  (one wavelength) phase shift between the electric fields of the two waves [15]. This corresponded to the half-wave displacement of the mirror since the reflected wave must travel both to and from the mirror and therefore has an overall motion of one wavelength.

Two common variations of the Michelson interferometer are the Twymann-Green and Mach-Zehnder interferometers. The Twymann-Green, shown in Figure 3-7, uses a coherent point source rather than the extended source of the Michelson. The coherent source allows for unequal path lengths in the two legs of the interferometer. For this reason, the Twymann-Green interferometer is also called a Laser Unequal Path Interferometer (LUPI) [19]. Collimating lenses are used to convert the diverging rays of the point source to (essentially) parallel rays within the interferometer. The rest of the interferometer operation is analogous. The Twymann-Green interferometer is typically used to measure imperfections within other optics, provided the optics within the interferometer are high quality, by placing the optic to be measured within one of the measurement paths. The optic distorts the normally planar wavefronts by slowing the light which passes through. Interference fringes can be seen at the interferometer output due to variations in the index of refraction across the optic face. The shape of these fringes indicates where the index of refraction is constant. Therefore, the fringe shapes can be thought of as a contour map which shows the variation of the light path length through the optic and may be used to polish the glass to a particular shape [20].

The Mach-Zehnder, shown in Figure 3-8, has two beam splitters and two mirrors arranged in a rectangular pattern. Typically, one path is disturbed while the other remains fixed to measure the relative change in path length.

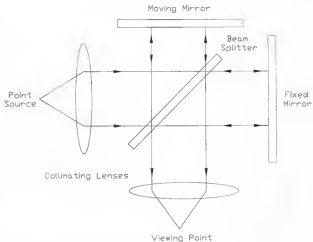


Figure 3-7: Twyman-Green Interferometer

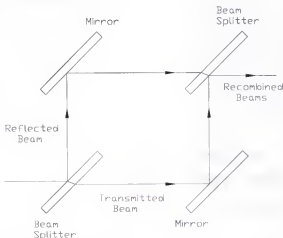


Figure 3-8: Mach-Zehnder Interferometer

The light-dark transitions in the Michelson interferometer discussed previously form the foundation for homodyne (DC), or single frequency, interferometry. After the two beams travel the measurement and reference paths, respectively, they must interfere. As noted, interference only occurs for beams with the same polarization state. If initially the two beams each have planar polarization perpendicular to one another, a polarizing filter may be placed in the path, oriented at  $45^\circ$  to each. A portion of each wave is absorbed by the polarizing filter and a portion passes through, each with the same polarization and now interfere. To find the total relative displacement of the moving mirror, the recombined beams are first incident on a photodetector. The photodetector then produces a signal proportional to the light intensity. For a  $\lambda/4$  motion of the moving mirror, the signal will vary from the maximum value to ideally zero (one-half fringe), assuming the fixed and moving mirrors initially had an equal path length. (The resolution may be increased by adding electronic circuitry to interpolate between the light and dark conditions.) The displacement is calculated by multiplying the number of fringes by  $1/2$  (the scale factor for a single-pass Michelson interferometer).

The measurement signal in a DC interferometer is therefore a function of the photodetector output amplitude. Several problems may arise from this reality. First, the system is susceptible to variations in the source intensity and ambient light since the measurement amplitude will vary for no motion. Second, a loss of the beam from either leg (or both) cannot be distinguished from total destructive interference. Finally, if motion is stopped at a maximum, there is no directional knowledge when motion starts again since either direction will give the same reduction in photodetector output. To obtain directional knowledge, part of the interfered signal can be split off, directed through a

quarter wave plate to shift the signal by 90° and compared to the original signal. This is analogous to the quadrature detection used in rotary encoders.

To this point, the interference of the two waves (recombined at the beam splitter) which provides uniform illumination at the photodetector has been taken for granted. If the two beams are not precisely parallel (mirrors are not perfectly orthogonal), fringes of equal spacing will be seen at the photodetector rather than the desired uniform intensity [17]. These fringes appear as dark bands across the otherwise bright output. As one mirror moves relative to the other, the fringes translate, but do not change the total intensity incident on the photodetector. Therefore, no motion is observed. A simple proof of this concept is to superimpose two transparent plastic sheets, each with finely spaced lines printed on one side. If the lines are not perfectly parallel when the sheets are placed over one another, fringes will be seen which move across the sheets during relative motion. If the lines on the two sheets are perfectly parallel, however, uniform intensity (bright and dark) will be seen for relative motion (i.e., for vertical translation with essentially horizontal lines).

In reality, the alignment of the mirrors in the Michelson interferometer is challenging and time-consuming. It requires precise, high-resolution angular adjustments of the mirrors and a stable optical bench to maintain the alignment. The minimum required alignment accuracy can be quantified according to Figure 3-9. As an example, consider two 3 mm diameter beams of green (coherent) laser light with perfectly planar wavefronts and equal wavelengths of 510 nm. As shown in Figure 3-9, the maximum allowable misalignment occurs when the edge of wavefront #2a overlaps with wavefront

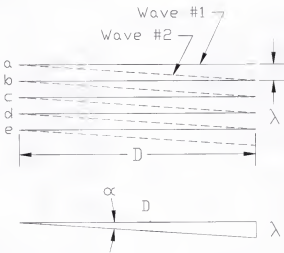


Figure 3-9: Alignment Accuracy

1b. For the typical values given, this predicts a maximum misalignment,  $\alpha$ , of 35.07 arc-sec (see Equation 3-5).

$$\alpha = \tan^{-1} (\lambda / D) * 3600 \text{ arc-sec}, \quad \text{where } \lambda = 510\text{e-9 m} \quad (3-5)$$

$$D = 3\text{e-3 m}$$

#### Heterodyne Interferometry

Modern users of linear displacement measuring interferometers rely mainly on heterodyne (AC), or two-frequency, interferometry. The light source is, in most instances, a frequency-stabilized Helium-Neon (He-Ne) laser tube with some method of generating a second frequency (within the bandwidth of modern electronics) from the natural He-Ne center frequency (roughly 474e3 GHz) within the laser head.

Several longitudinal modes may actually be available within the single  $\text{TEM}_{00}$  transverse mode of light emitted from the laser head, depending on the length of the lasing cavity. However, the frequency split between modes is normally hundreds of megahertz and beyond the bandwidth of most modern electronics. These adjacent longitudinal modes each satisfy the resonant condition for lasing, which is dependent on both the laser cavity length and the wavelength of light, at different frequencies under the He-Ne gain curve (see Equation 3-6). Furthermore, the physics of the process requires that adjacent modes be orthogonally polarized. The frequency difference between two longitudinal modes may be calculated according to Equation 3-7 [26]. The  $\text{TEM}_{00}$  transverse mode has a Gaussian cross-sectional intensity profile. The variation in irradiance across the beam is given in Equation 3-8 [17].

$$2L = m\lambda, \quad \text{where } L = \text{laser cavity length} \quad (3-6)$$

m = integer longitudinal mode number  
 $\lambda$  = light wavelength

$$f_{n+1} - f_n = \frac{c}{2Ln}, \quad \text{where } f_i = \text{light frequency} \quad (3-7)$$

c = speed of light  
n = refractive index of medium

$$I = e^{\frac{-8y^2}{D^2}}, \quad \text{where } I = \text{beam intensity} \quad (3-8)$$

y = transverse beam direction  
D = beam width at given position

In heterodyne systems, by definition, the frequencies of the measurement and reference beams differ slightly. When these two beams of different frequency are recombined at the beam splitter (after traveling different paths) and passed through a polarizing filter, rather than pure constructive or destructive interference, linear superposition yields a wave with a periodically varying amplitude and some phase as shown in Figure 3-10.

If the two beam frequencies are considered as phasors (or vectors) rotating with unequal angular velocities, the phasor with the higher frequency will periodically overtake the slower phasor and the two will have a relative angular velocity of  $2\pi(f_1 - f_2)$  radians/second. The time (in seconds) it takes for one phasor to overtake the other is  $(f_1 - f_2)^{-1}$ . If the two phasors are equal in amplitude (A) and have a small difference in frequency, the interference resultant, y, is described by Equation 3-9. This is essentially a sine wave with a slowly varying, or modulated, amplitude (given by the cosine term). The frequency of the varying amplitude envelope, or beat frequency, is equal to the difference between the two individual frequencies of the measurement and reference beams ( $f_1 - f_2$ )

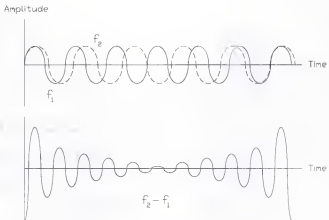


Figure 3-10: Beat Phenomenon

in Hz. The frequency of the actual waveform is the average of the two original signal frequencies,  $0.5(f_1 + f_2)$  [21][22].

$$\begin{aligned}y &= A \sin \omega_1 t + A \sin \omega_2 t \\&= 2A \cos((\omega_1 - \omega_2)/2)t \cdot \sin((\omega_1 + \omega_2)/2)t\end{aligned}\quad (3-9)$$

This heterodyne technique carries the displacement information in the phase of the interfered measurement and reference signals rather than the amplitude. In the frequency domain, a motion of the moving retroreflector causes a change in frequency of the beat signal due to the Doppler shift. For a perfectly sinusoidal beat signal, the single Fourier transform spike at the beat frequency can be viewed sliding left or right (depending on the displacement direction) using a spectrum analyzer. In this way, the frequency/phase relationship can be considered analogous to the velocity/position relationship, where the frequency is simply the circular velocity.

As noted, the measurement and reference beams can be represented by phasors which are rotating with angular velocities equal to the respective optical frequencies of the two beams. For no retroreflector motion (and no subsequent Doppler shift), one phasor periodically overtakes the other (as described previously). The combination of these two vectors, therefore, provides a resting beat frequency equal to the difference between the two optical frequencies. During motion, the phase of the measurement vector with respect to the reference vector either grows larger or smaller (i.e. the beat frequency is either up or down-shifted) depending on the direction of the moving mirror. Unlike homodyne systems, which have a zero Hertz beat frequency at rest and can therefore only exhibit an up-shift in frequency regardless of the motion direction, heterodyne systems

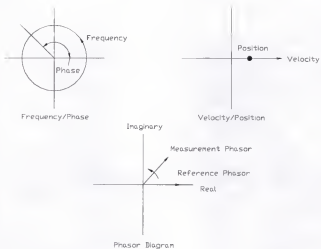


Figure 3-11: Heterodyne Phase Relationships

provide directional sensitivity by the increase or decrease in relative phase. Using phase measuring electronics, the instantaneous phase between the two phasors is recorded and converted to displacement (see Figure 3-11). In the time domain, the beat frequency sinusoid can be seen translating in either direction on an oscilloscope. The amount of shift is the phase change, which carries the displacement information.

The Doppler shift, which is responsible for the phase change in the interfered signals, can be explained in several ways. One can characterize the shift by the time of flight, such as the change in pitch observed when a car with the horn blowing passes by or Doppler radar. It is also possible to think of the light as being *stretched* by the velocity of the moving reflector [21].

An intuitive explanation, provided by John Beckwith of Lawrence Livermore National Laboratory in Livermore, CA, is to consider the light path as a pipeline [23]. The wavelengths,  $\lambda$ , can then be thought of as filling up the pipeline. For a wavelength of 632.8 nm (He-Ne light), this gives a wavenumber or V-number,  $\lambda^{-1}$ , of  $1580278.1 \text{ m}^{-1}$ . The wavenumber represents the number of  $\lambda$ s in one meter of this imaginary pipeline. If the pipeline now begins lengthening at 1 m/s, there will be 1580278.1 more  $\lambda$ s entering the pipeline than exiting. This is analogous to moving the mirror away from the beam splitter in the Michelson interferometer, except that this number is doubled because the light must travel both to and from the mirror (this represents a fold factor of 2 or scale factor of 1/2). Therefore, a negative frequency shift in the beat frequency of  $2 * 1580278.1 \text{ Hz/m/s}$  will be seen for this motion direction because there is a deficit of  $\lambda$ s.

To further clarify the Doppler shift concept, the author would also like to add the notion of a 'bag of light,' or  $\lambda$ s, attached to the end of the pipeline. As the pipeline is

lengthening, the 'bag of  $\lambda$ s' is emptying and the deficit describes the negative frequency shift previously noted.

Now consider the mirror moving toward the beam splitter. In this case, the pipeline will be shrinking at 1 m/s and there will be 1580278.1 more  $\lambda$ s exiting the pipeline than entering (i.e., the 'bag of  $\lambda$ s' is filling). Now the frequency shift will be positive  $2 * 1580278.1 \text{ Hz/m/s}$  for the interferometer. This number gives a general rule of thumb for the frequency shift of red He-Ne laser light in a single-pass Michelson interferometer. The shift for a velocity of 1 ft/s is roughly 1 MHz (or 1 MHz/ft/s); the actual value is 0.9633375 MHz/ft/s.

In modern heterodyne interferometry, however, the situation is a little more complex. The Doppler shifted frequency is the difference between the optical frequency ( $474e12 \text{ Hz}$  for He-Ne), designated  $f_o$ , and the second frequency,  $f_s \pm f_d$ , normally generated within the laser head by either acousto-optic modulation or Zeeman split. This second frequency can be upshifted or downshifted by the amount  $f_d$ . In this case, consider an upshifted second frequency of  $f_s + f_d$ .

For no retroreflector motion, the two optical frequencies remain fixed in the frequency spectrum. The beat frequency is, therefore, the difference between the two,  $f_b$ . Either the optical or shifted frequency signal could function as the reference beam, so either may be Doppler shifted (by retroreflector motion). For instance, if the  $f_o$  mirror was moving away from the beam splitter, this signal would be Doppler shifted down by an amount  $f_d$ . According to Figure 3-12, this would produce an increase in the beat frequency and a positive phase (and therefore displacement) since the total difference

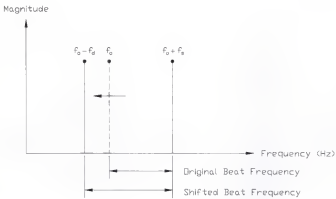


Figure 3-12: Beat Frequency Shift

between the two signals is increasing. Moving the  $f_o + f_s$  mirror in the same direction will have the opposite effect.

A brief description of two common methods to generate the second, shifted frequency for use in heterodyne systems will now be provided (recall that the naturally available adjacent longitudinal modes are separated by hundreds of megahertz and the frequency split is generally outside the electronics' bandwidth). In the acousto-optic technique, a single longitudinal mode (of the  $\text{TEM}_{00}$  transverse wave) is passed through an acousto-optic modulator. This device is, in its simplest form, a piece of glass with a PZT attached to one edge. This transducer is driven at the shifting frequency by a stable quartz oscillator and produces a traveling acoustic (sound) wave in the glass. This traveling sound wave produces successive compressions and rarefractions in the medium which changes the index of refraction periodically along its length. The periodically varying refractive index produces a moving diffraction grating. When linearly polarized, monochromatic light is incident on this phase diffraction grating at the Bragg angle,  $\theta_B$ , a large portion of the beam is diffracted and frequency shifted (for certain crystals the polarization vector is also rotated by  $90^\circ$ ), while the rest is transmitted (with no frequency shift) (see Figure 3-13). The diffracted and transmitted waves are diverging at twice the Bragg angle and are, therefore, spatially separated. The Bragg angle, which is proportional to the driving frequency,  $f_{\text{acoustic}}$ , is given in Equation 3-10. The two frequencies may then be recombined into a single heterodyne beam.

$$2 \theta_B = \lambda / \lambda_{\text{acoustic}}, \quad \text{where } \lambda_{\text{acoustic}} = V_{\text{acoustic}} / f_{\text{acoustic}} \quad (3-10)$$

$V_{\text{acoustic}} = \text{acoustic velocity}$

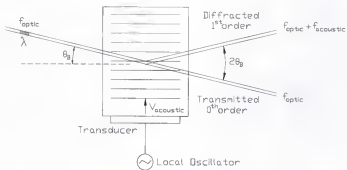


Figure 3-13: Acousto-optic Modulator

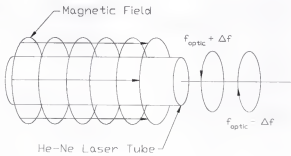


Figure 3-14: Zeeman Split

The Zeeman frequency split is accomplished by placing a magnetic field around the He-Ne laser tube. At low magnetic power, there exists one (preferential) linearly polarized, longitudinal mode in the laser tube (provided the laser cavity is "short"). At some higher power level, this single mode snaps into two circularly polarized modes (one left, one right) of different frequencies. The actual frequency difference between the two modes is dependent on the magnetic field strength. The He-Ne medium is able to support the two modes of different wavelengths (which are not harmonics of one another) in one tube due to the presence of a circular birefringence [23] (see Figure 3-14 [15]). In other words, the two modes see effectively different laser cavity lengths, due to the different indices of refraction, and satisfy the condition for lasing (Equation 3-6) at two different wavelengths (frequencies).

The mathematics behind the heterodyne interference will now be discussed. The math is not complex and relies simply on the trigonometric relationship  $2 \cos(A) \cos(B) = \cos(A+B) + \cos(A-B)$ . The electric field ( $E$ ) of the resultant beam after interference of the measurement (moving mirror) and reference beams (fixed mirror) is expressed in Equation 3-11. Again, the interference of the two beams with initially perpendicular planar polarizations is accomplished using a 45° polarizing filter. The subscript  $m$  refers to the measurement beam and the subscript  $r$  to the reference beam.

$$E = E_m \cos((\omega_0 + \omega_s)t + \phi_0 + \phi_d) + E_r \cos(\omega_0 t + \phi_0), \quad (3-11)$$

where  $E_m, E_r$  = magnitude (V/m)  
 $\omega_0$  = optical frequency (rad/s)  
 $\omega_s$  = shift frequency (rad/s)  
 $\phi_0$  = initial phase (rad)  
 $\phi_d$  = Doppler phase shift (rad)

When the interfered beam is incident on a photodetector, the output is proportional to the field strength squared ( $i \sim E^2$ ). The quantity  $E^2$  and resultant simplifications are shown in Equation 3-12. The final simplification step is the detector output because all frequencies except  $\omega_0$  are outside the detector's bandwidth (i.e. the detector acts like a low pass filter) and the DC component is not used in the dynamic, heterodyne measurement.

$$\begin{aligned} E^2 &= E_m^2 \cos^2((\omega_0 + \omega_b)t + \phi_0 + \phi_d) + E_r^2 \cos^2(\omega_b t + \phi_0) \\ &\quad + 2 E_m E_r \cos((\omega_0 + \omega_b)t + \phi_0 + \phi_d) \cos(\omega_b t + \phi_0) \end{aligned} \quad (3-12)$$

Expand to obtain:

$$\begin{aligned} &= 0.5 E_m^2 (\cos(2(\omega_0 + \omega_b)t + 2\phi_0 + 2\phi_d) + \cos(0)) + 0.5 E_r^2 (\cos(2\omega_b t + 2\phi_0) + \\ &\quad \cos(0)) + 2 E_m E_r (0.5 (\cos(2\omega_b t + \omega_b t + 2\phi_0 + \phi_d) + \cos(\omega_b t + \phi_d))) \end{aligned}$$

Ignore all terms which contain the optical frequency (outside detector bandwidth):

$$= 0.5 E_m^2 + 0.5 E_r^2 + E_m E_r \cos(\omega_b t + \phi_d)$$

Neglect the DC components of the signal:

$$= E_m E_r \cos(\omega_b t + \phi_d)$$

A typical linear interferometer consists minimally of a two-frequency He-Ne laser head with the two frequencies occupying perpendicular polarizations (polarization coded), a polarization beam splitter, two retroreflectors, and a heterodyne receiver with the necessary phase measuring electronics. Variations in the optical setup allow measurement of linear and angular displacement, straightness of travel, flatness, squareness, and parallelism, as well as changes in the refractive index of air (although all are derived from a change in displacement) [15].

Simple linear displacement is measured as shown in Figure 3-15. At the polarization beam splitter it can be seen that the polarization parallel to the plane of

incidence is transmitted, while the vertical polarization is reflected. The polarization parallel to the plane of incidence (the plane of the page) is normally referred to as the transverse magnetic (TM) mode, or 'p' mode. The polarization perpendicular to the plane of incidence is called the transverse electric (TE) mode, or 's' mode [17]. Either path can act as the reference or measurement leg of the Michelson interferometer. The beams are recombined (for interference) when they return from their respective retroreflectors. The retroreflectors, glass optics with three silvered faces containing a solid right angle, simplify the alignment procedure greatly by returning a beam parallel to the incident beam (after three reflections) regardless of the incident angle [20]. This nearly guarantees interference provided there are no significant changes in the wavefront shape of the transmitted and reflected beams. Figure 3-16 shows a method of measuring angular deviations using only a polarization beam splitter (PBS), a 90° prism, and two retroreflectors.

#### Fiber Optics in Interferometry

A discussion of modern heterodyne interferometry would be remiss if a brief description of fiber optics and their application to heterodyne interferometry were not included. Although the main use of fiber optic technology is in the field of communications, metrology applications, such as fiber optic sensors and fiber delivery/collection of heterodyne measurement signals, are becoming quite common. Heterodyne fiber delivery/collection will be discussed here.

An example heterodyne fiber delivery/collection system is shown in Figure 3-17. The different fiber types shown in the figure, single-mode polarization maintaining (SMPM) and multimode (MM), will be discussed after a brief review of total internal

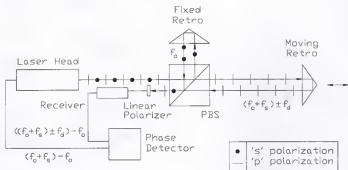


Figure 3-15: Linear Displacement Interferometer

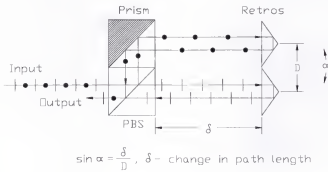


Figure 3-16: Angular Measurement Setup

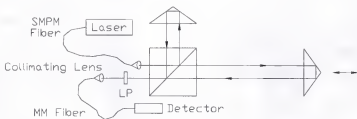


Figure 3-17: Fiber Delivery/Collection

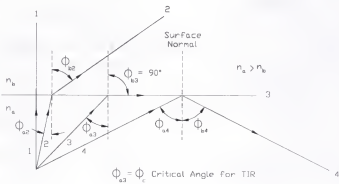


Figure 3-18: Total Internal Reflection

reflection, launching conditions, fiber numerical aperture (NA), and mode distribution in fibers.

When light travels from one medium to a medium with a different refractive index, it obeys Snell's law of refraction. See Equation 3-13. In the case of light entering a medium with a lower index of refraction,  $n_b$ , the refracted angle,  $\phi_b$ , is greater than the incident angle,  $\phi_a$  (i.e., the light bends away from the surface normal) (see Figure 3-18). As the incident angle is increased, the refracted angle in the second medium increases until it reaches  $90^\circ$ . At this point, the interface between the two media begins to act as a perfect mirror and the light is reflected back into the first medium according to Snell's law (incident angle equals reflected angle). This situation is called total internal reflection (TIR). The critical angle of incidence for TIR may be derived from Snell's law by substituting  $90^\circ$  for the refracted angle. The critical angle,  $\phi_{\text{critical}}$ , is given in Equation 3-14. If the first medium is a transparent rod, or fiber optic, and the surrounding medium is air (or any medium with a lower refractive index), light input at the critical angle will be trapped within the rod by TIR [16].

$$n_a \sin \phi_a = n_b \sin \phi_b \quad (3-13)$$

$$\sin \phi_{\text{critical}} = n_b / n_a, \text{ where } n_b < n_a \quad (3-14)$$

The light trapped by TIR in the fiber will only remain in the fiber provided it does not come into contact with another surface. If the fiber touches a surface with a higher index of refraction, TIR will no longer occur. To circumvent this problem, optical fibers

consist of a core, cladding and protective jacket. The core carries the light and has a higher index of refraction ( $n_{core}$ ) than the cladding ( $n_{cladding}$ ) which surrounds the core.

Two typical cross-sectional profiles for the core index of refraction are shown in Figure 3-19. The step index profile has an abrupt discontinuity at the cladding interface, while the graded-index profile has a smoothly changing index of refraction, typically parabolic in shape. The advantage of graded-index fiber is seen in communications. For a step index, the path length for a ray entering at the maximum angle for TIR (cone angle) is longer than the path length for one which enters along the fiber axis. This different path time (due to a constant refractive index) will smear, or broaden, a pulse (bit) of information by modal distortion and limit the data transfer rate (bandwidth). A graded-index fiber with a parabolic profile significantly reduces this problem [24]. Additionally, a reduction in the number of modes propagating in the fiber lessens the effect of modal distortion.

Material dispersion, inherent to all fiber optics, also limits the system bandwidth by pulse broadening. In any given material there is a dependence of the refractive index on the wavelength of light traveling in the medium. Since there are no completely monochromatic sources, the input light encompasses a range of wavelengths, referred to as the free spectral range (at full width half maximum). As this range of wavelengths propagates through the fiber, the information carried in the longer wavelengths travels faster than the information in the shorter wavelengths (i.e., the refractive index decreases with wavelength for normal dispersion). Therefore, the input pulse spreads in time and, in the extreme case, overlaps with the next pulse. Adjacent pulses can then no longer be distinguished and the data transfer rate is limited [17].

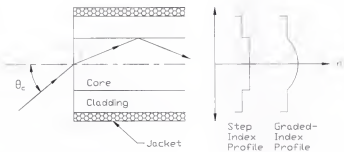


Figure 3-19: Refractive Index Profiles

The cone of light which may be accepted by a fiber is a function of the core and cladding indices of refraction. The half-angle ( $\theta_c$ ) of the acceptance cone may be calculated according to Equation 3-15 for a step index fiber.

$$n_i \sin \theta_c = (n_{\text{core}}^2 - n_{\text{cladding}}^2)^{0.5}, \text{ where } n_i = 1 \text{ for light from air} \quad (3-15)$$

A fiber's numerical aperture (NA), a measure of the light-gathering capability of the fiber, is also a function of the core and cladding refractive indices. The NA for a step index fiber with light incident on the fiber from air is given in Equation 3-16. It should be noted that this particular figure of merit is independent of the fiber geometry.

$$\text{NA} = (n_{\text{core}}^2 - n_{\text{cladding}}^2)^{0.5} \quad (3-16)$$

A fiber's NA is an important consideration in the launch conditions of light into a fiber. For example, if light is introduced into the fiber with a cone of diverging rays greater than the maximum cone angle of the fiber, some of the source light cannot be propagated by the fiber. This situation is referred to as "overfilling" the fiber and causes transmission losses. If the source cone of light is less than the maximum cone angle the fiber can accept, the fiber is "underfilled," but results in less attenuation than in the overfilled case.

If light is being coupled into the fiber from a collimated source (i.e., the source emits light in only one direction), a converging (double convex) lens may be used to focus the light on the fiber core (a challenging task which is mainly a function of the angle at

which the light strikes the fiber from the lens). The NA of the beam may now be found according to Equation 3-17. This NA must then be compared to the fiber NA to avoid overfilling.

$$\text{NA}_{\text{beam}} = n \sin (\tau_o / f), \quad \begin{aligned} &\text{where } \tau_o = \text{initial beam waist radius} \\ &f = \text{lens focal length} \\ &n = \text{air refractive index} (= 1) \end{aligned} \quad (3-17)$$

Once light is coupled into the fiber, it is next important to understand how it propagates in the fiber. By combining Maxwell's equations, a wave equation may be obtained which can be solved for the distribution of the electromagnetic field across the fiber face, or the guided modes. A solution of the wave equation for these modes depends on the fiber geometry and index profile of the core and cladding. To determine the number of modes which will be supported by a given fiber, the normalized wavenumber, or V-number, may be calculated (see Equation 3-18 [24]). An alternate analysis, developed in [17], suggests that the maximum number of supported modes ( $m_{\max}$ ) may be calculated according to Equation 3-19.

$$V = k_o (a) \text{NA}, \quad \begin{aligned} &\text{where } k_o = \text{free space wavenumber} = 2\pi / \lambda_o \\ &a = \text{fiber core radius} \end{aligned} \quad (3-18)$$

$$m_{\max} = \frac{1}{2} \left( \frac{\pi d}{\lambda_o} \text{NA} \right)^2, \quad \begin{aligned} &\text{where } d = \text{fiber core diameter} \end{aligned} \quad (3-19)$$

It can be seen that a small core diameter, small NA, or a large free space wavelength,  $\lambda_0$ , will decrease the V-number and reduce the number of modes supported by the fiber. For  $V < 2.405$ , only a single mode (HE<sub>11</sub>) will be supported. Fibers which support just this single mode are known as single mode fibers. As the V-number is increased, more modes may be carried by the fiber. These fibers are referred to as multimode fibers. Typical multimode communications fibers may have V-numbers from 50 to 150.

In many cases, it is desirable to maintain the polarization state of the input light through the length of a single mode fiber. This is the case for the fiber feed from the laser head to the interferometer (e.g., the single mode-polarization maintaining or SMPM fiber shown in Figure 3-17). For the fiber to maintain the input polarization state, it is stressed along a single axis to produce a birefringence in the fiber (see Figure 3-20 [25]). Light linearly polarized along the stressed axis travels at a slower rate than light orthogonally polarized to this axis. If the two orthogonal frequency components from the laser head are aligned with these birefringent (fast and slow) axes when launching into the fiber, sensitivity to environmental effects is reduced and the input polarizations are maintained. For an ideal fiber and perfect launch conditions, the fiber input and output light could be described by the same wave equation. In reality, there is a small amount of polarization "leakage" between the fast and slow axes and small relative phase shifts introduced due to mechanical and environmental cable perturbations.

Again referring to the heterodyne system shown in Figure 3-17, once the two orthogonal polarizations have traversed the Michelson interferometer (to introduce a relative phase shift between reference and measurement signals) and interfered at the

polarizing filter, there is no longer any need to maintain the polarization state because the displacement information is now carried in the phase of the optical signal. Therefore, the light may now be carried on a high NA multimode (MM) fiber to the phase measuring electronics. Multimode fibers generally have a much larger core diameter and are easier to couple into than single-mode fibers.

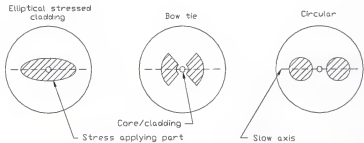


Figure 3-20: Single-mode Fibers

## CHAPTER 4 STLBB DESIGN

As noted in Chapter 1, the Laser Ball Bar (LBB) is a precision linear displacement measuring device. It consists of a two-stage telescoping tube with a precision sphere mounted at each end. A heterodyne displacement measuring interferometer is aligned inside the telescoping tube and measures the relative displacement between the two spheres (see Figure 4-1).

Once initialized, the LBB uses trilateration to measure the spatial coordinates of points along a CNC part path. The six sides of the tetrahedron formed by three base sockets (attached to the machine table) and a tool socket (mounted in the spindle) are measured, and, by geometry, the coordinates of the tool position (end effector) can be calculated.

In simultaneous trilateration, three LBBs ride on a single sphere at the tool point to completely define the tetrahedron with one execution of the CNC program (the three lengths between the base sockets are measured prior to executing the part program and remain fixed throughout the measurement). Figure 4-2 illustrates this method. The physical implementation of simultaneous trilateration required the design of a joint at the tool socket to support all three LBBs and a bracket to mount the joint at the tool point on the spindle. A redesign of the past generation LBB was also completed. The tool socket joint, tool point bracket, and new LBB mechanical and optical design will now be outlined.

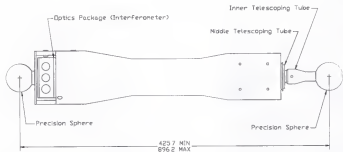


Figure 4-1: Laser Ball Bar

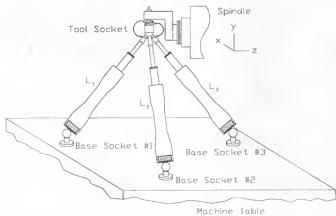


Figure 4-2: Simultaneous Trilateration

Tool Socket Joint

Simultaneous trilateration requires that the axes of the three LBBs meet at a single point which coincides with the tool point (to minimize Abbe offset errors). During the execution of a CNC part program, the coordinates of the tool point are measured at finite intervals along the path to define the contouring accuracy. As the spatial coordinates of the tool point vary, the lengths of the individual LBBs change as well as the angles between the LBBs. This calls for a joint which provides three independent angular degrees of freedom while prohibiting relative translations between the endpoints of each of the three LBB axes (e.g., a spherical joint). This joint provided a challenging design problem when combined with the minimum space, low friction, and ease of assembly/disassembly requirements of the STLBB system.

For the first generation STLBB system, the initial concept was the use of a single precision sphere at the tool socket with three magnetic sockets utilized to attach the LBBs to the sphere. In a first analysis, the main concern with this design appeared to be the coefficient of friction between the sphere and sockets. However, one design change in the LBBs used in this research was a 50% increase in length. This length increase expanded the work volume for the LBB, but also added weight. Therefore, adequate magnetic attractive force to secure the LBBs to the sphere was also an important consideration. Additionally, it was required to minimize the cross-sectional area of the sockets to reduce interference between the three sockets riding on the single sphere.

### Socket Interference

A minimum angle between adjacent LBB sockets of  $45^{\circ}$  was selected to maximize the measurement volume, while still allowing adequate space for the magnets (a larger magnet cross-sectional area provides more attractive force). This angle, combined with the sphere diameter ( $D$ ) constrains the allowable LBB socket diameter (see Figure 4-3).

$$d_{socket} = D \sin\left(\frac{45^{\circ}}{2}\right) \quad (4-1)$$

From Equation 4-1, the maximum LBB socket diameter can be calculated. For a sphere diameter of 38.1 mm (1.5"), the maximum allowable LBB socket diameter is 14.58 mm (0.574"). A 12.7 mm (0.5") diameter by 12.7 mm long cylindrical neodymium magnet was then chosen to fit inside the LBB socket and attach the socket to the tool sphere.

Initial tests using the LBBs and these magnets provided less than desirable results. Although near vertical static positions could be held, horizontal positions or motions with high accelerations caused the sockets to tip off the tool sphere. To remedy these problems, a spring aid was designed to provide additional support for the LBBs at the tool sphere.

### Magnetic/Spring Force

The requirement for this spring aid was to provide a mechanical force along a line approximately parallel to the magnetic force (or the LBB axis), while minimizing the motion limitations placed on the measurement volume. From experimental

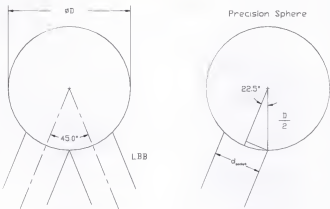


Figure 4-3: Socket Diameter Constraints

measurements, it was determined that an additional 8.9 N (2 lb<sub>f</sub>) would provide adequate holding power, but not introduce an excessive normal force which would increase the friction force between the sphere and LBB socket.

The spring aid is shown in Figure 4-4. It is composed of a tool socket and sphere, upper bearing with pin connection, spring assembly, and lower collar with pin connection (attached to the LBB socket). The pin connections allow the spring assembly to move as the LBB socket rotates about the sphere center and the upper sintered brass bearing allows rotation about the vertical axis. Two LBBs require this spring aid. The other is rigidly fixed to the tool sphere using a threaded connection.

The radius and cross-sectional dimensions of the spring steel assembly which provides the holding force were calculated using Castigliano's Theorem on Deflections [33]. The spring was modeled as a curved beam with the required force applied at the free end (see Figure 4-5). By selecting representative values for the force (F), radius (R), Young's modulus (E), deflection ( $q_F$ ), and width (w), the required thickness (t) could be calculated.

$$q_F = \int_0^{\pi} \frac{M}{EI} \frac{\partial M}{\partial F} R d\theta \quad (4-2)$$

In Equation 4-2, the formula for the deflection of the spring end in the direction of the force is given (deflections due to axial and shear loads have been neglected). The solution of this definite integral and substitution of  $wt^3/12$  for the 2<sup>nd</sup> area moment of inertia (I) provides an equation for the necessary thickness. Using the dimensions shown

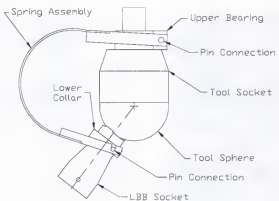


Figure 4-4: Tool Socket Spring Aid

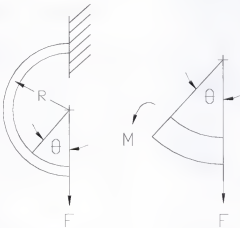


Figure 4-5: Castigiano Modeling

in Equation 4-3, the spring aid was found to provide a range of motion of 22.5° to 38° from the vertical axis (see Figure 4-6). The minimum angle of 22.5° results from interference between adjacent LBBs on the tool sphere. The maximum angle, 76° between adjacent LBBs, was imposed by the spring aid design. Because the two spring assembly upper bearings were stacked upon one another, there was a constraint placed on the maximum angular deviation of each spring assembly. In the final spring aid design, the maximum range of motion was chosen to satisfy this constraint.

$$t = \left[ \frac{6\pi F R^3}{E w q_p} \right]^{\frac{1}{3}} = 0.8 \text{ mm} \quad (4-3)$$

where $F = 8.9 \text{ N}$	$q_p = 3.15 \text{ mm}$
$R = 0.03 \text{ m}$	$w = 12.7 \text{ mm}$
$E = 200e9 \text{ N/m}^2$	

The tool socket holds the tool sphere using a magnetic connection. In this case, the size requirements were relaxed so a magnet of adequate flux could be selected. In fact, it was necessary to limit the magnetic force so that unnecessary friction forces would not be developed between the sphere and the tool socket during rotations of the LBB which is rigidly connected to the sphere.

The magnetic flux lines for the tool socket geometry are shown in Figure 4-7a. The 440 stainless steel (SST) socket completes the magnetic circuit through the sphere. The neodymium magnetic is encased in a brass (non-magnetic) sleeve to force the flux lines out the plane of the magnet. It was found that the magnetic attractive force could be reduced by decreasing the height of the socket. The new predicted flux lines for a short

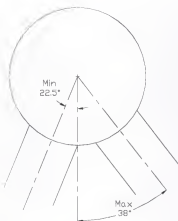


Figure 4-6: Spring Aid Range of Motion

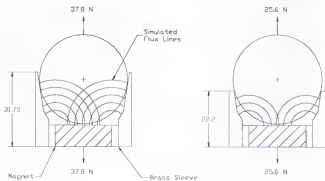


Figure 4-7: Magnetic Flux Lines

socket are shown in Figure 4-7b. For a 31.75 mm (1.25") tool socket, the magnetic force was found to be 37.8 N (8.5 lb<sub>f</sub>), which is adequate to support the three LBBs.

#### Maximum Allowable Coefficient of Friction

Another important consideration for the tool socket joint is the coefficient of friction at the sphere/LBB socket interface. If the coefficient of friction between the LBB socket and the tool sphere is large, the socket will not slide around the sphere surface. Instead, the socket would tend to tip off the sphere and cause measurement errors [35]. A static analysis of the LBB socket/sphere interface was therefore performed to find the maximum allowable coefficient of friction to prevent tipping.

The planar free body diagram for the static case is shown in Figure 4-8. This figure shows the normal and friction forces at the socket/sphere interface ( $N_i$  and  $\mu N_i$ , ( $i = 1$  to  $2$ )), the spring aid force ( $S$ ), the magnetic force ( $M$ ), the LBB weight ( $W$ ), and a force applied to the LBB end ( $P$ ). The static equations of equilibrium are shown in Equation 4-4. The simultaneous solution of these equations was found using the symbolic mathematics software Maple V Release 4.0™. This solution yields an expression for the sliding force ( $P_{slide}$ ) in terms of the unknown ( $\mu$ ) and the knowns ( $\theta$ ,  $r$ ,  $S$ ,  $\phi$ ,  $W$ ,  $d$ ,  $L_1$ ,  $L_2$ ,  $M$  and  $\beta$ ) (see Equation 4-5).

$$\sum F_z = 0$$

$$0 = P \cos \theta + S \sin \phi + M \sin \theta - N_1 \sin(\theta - \beta) - \mu N_1 \cos(\theta - \beta) - \\ N_2 \sin(\theta + \beta) - \mu N_2 \cos(\theta + \beta)$$

$$\sum F_y = 0$$

$$0 = -P \sin \theta + S \cos \phi + M \cos \theta - N_1 \cos(\theta - \beta) + \mu N_1 \sin(\theta - \beta) - \\ N_2 \cos(\theta + \beta) + \mu N_2 \sin(\theta + \beta) - W \quad (4-4)$$

$$\sum M_0 = 0$$

$$0 = -\mu N_1 r - \mu N_2 r + PL_1 - Sd + WL_2 \sin \theta$$

$$P_{\text{slide}} = (-\sin(\theta)^2 \mu^2 r^2 S \sin(\phi) + \sin(\theta) \mu^2 r^2 \cos(\theta) W - S d \mu^2 L_1 \cos(\theta)) \quad (4-5) \\ - \sin(\theta) \mu^2 r^2 M + \sin(\theta) L_1 S d \mu u - \sin(\theta)^2 L_1 W L_2 \mu - W L_2 \sin(\theta)^2 \mu^3 L_1 \\ - \cos(\theta) L_1 S d + S d \mu^3 L_1 \sin(\theta) - \mu^3 r^2 \sin(\theta)^2 W + W L_2 \sin(\theta) \mu^2 L_1 \\ \cos(\theta) + \cos(\theta) L_1 W L_2 \sin(\theta) - \mu^3 r \sin(\theta) S d \cos(\beta) + \mu^3 r^2 \sin(\theta)^2 S \\ \cos(\phi) - 2 \sin(\theta) \mu^2 r \cos(\theta) \cos(\beta) L_1 W + \cos(\beta) L_1 \mu r W - \sin(\theta) \mu r S d \\ \cos(\beta) - \cos(\theta) \cos(\beta) L_1 \mu r M - \sin(\theta)^2 \mu r \cos(\beta) L_1 W + \mu r \sin(\theta) \\ \sin(\beta) L_1 \cos(\theta) W - \mu^3 r \cos(\theta) \sin(\beta) L_1 \sin(\theta) W + \sin(\beta) L_1 W \mu^2 r + W \\ L_2 \sin(\theta) \sin(\beta) L_1 \cos(\beta) \mu \cos(\theta) + W L_2 \sin(\theta) \sin(\beta) \mu^3 \cos(\beta) L_1 \\ \cos(\theta) - S d \sin(\beta) L_1 \cos(\beta) \mu \cos(\theta) - S d \sin(\beta) \mu^3 \cos(\beta) L_1 \cos(\theta) + W \\ L_2 \sin(\theta)^2 \sin(\beta) L_1 \cos(\beta) - \sin(\theta) S d \sin(\beta) L_1 \cos(\beta) - \sin(\theta) S d \sin(\beta) \\ \mu^2 \cos(\beta) L_1 + W L_2 \sin(\theta)^2 \sin(\beta) \mu^2 \cos(\beta) L_1 + \mu^3 r W L_2 \sin(\theta)^2 \cos(\beta) \\ + \mu^3 r \sin(\theta)^2 \cos(\beta) L_1 W + \sin(\theta) \mu^2 r \cos(\beta) L_1 M + \sin(\theta)^2 \mu r W L_2 \\ \cos(\beta) - \cos(\theta) L_1 W L_2 \sin(\theta) \sin(\beta)^2 - 2 \sin(\theta)^2 \mu^2 r \sin(\beta) L_1 W + W L_2 \\ \sin(\theta)^2 \sin(\beta)^2 \mu^3 L_1 - S d \sin(\beta)^2 L_1 \mu \sin(\theta) - S d \sin(\beta)^2 \mu^3 L_1 \sin(\theta) + \mu^2 \\ \cos(\theta) \sin(\beta)^2 L_1 S d - M \cos(\theta) L_1 \sin(\beta) \mu^2 r + \cos(\theta) L_1 S d \sin(\beta)^2 - \mu^2 \\ \cos(\theta) \sin(\beta)^2 L_1 W L_2 \sin(\theta) + W L_2 \sin(\theta)^2 \sin(\beta)^2 L_1 \mu - \mu r \sin(\theta) \sin(\beta) \\ L_1 M - \sin(\theta) \mu^2 r^2 \cos(\theta) S \cos(\phi) + 2 \sin(\theta) \mu^2 r \cos(\theta) \cos(\beta) L_1 S \\ \cos(\phi) - \cos(\beta) L_1 \mu r S \cos(\phi) + \mu^3 r \cos(\theta) \sin(\beta) L_1 \sin(\theta) S \cos(\phi) - \mu r \\ \sin(\theta) \sin(\beta) L_1 \cos(\theta) S \cos(\phi) - \sin(\beta) L_1 S \cos(\phi) \mu^2 r - \mu^3 r \sin(\theta)^2 \\ \cos(\beta) L_1 S \cos(\phi) + \sin(\theta)^2 \mu r \cos(\beta) L_1 S \cos(\phi) + 2 \mu^2 r \sin(\theta)^2 \sin(\beta) \\ L_1 S \cos(\phi) - \mu^2 r \cos(\beta) L_1 S \sin(\phi) - \mu^3 r \sin(\theta) S \sin(\phi) \cos(\theta) + \mu^3 r \\ \sin(\theta) \cos(\beta) L_1 S \sin(\phi) \cos(\theta) - \sin(\theta) \mu r S \sin(\phi) L_1 \cos(\theta) \cos(\beta) + \mu^3 r \\ \sin(\beta) L_1 S \sin(\phi) \sin(\theta)^2 - 2 \mu^2 r \sin(\theta) \sin(\beta) L_1 S \sin(\phi) \cos(\theta) - \mu^3 r \\ \sin(\beta) L_1 S \sin(\phi) + 2 \sin(\theta)^2 \mu^2 r \sin(\phi) L_1 \cos(\beta) - \mu r \sin(\theta)^2 \sin(\beta) L_1 \\ S \sin(\phi)) / ((-L_1 \cos(\beta) - \mu^2 \cos(\beta) L_1 + \mu^2 r) (\sin(\theta) \mu r + \cos(\theta) \cos(\beta) \\ L_1 + \sin(\theta) \sin(\beta) L_1 - \mu \sin(\theta) \cos(\beta) L_1 + \mu \cos(\theta) \sin(\beta) L_1))$$

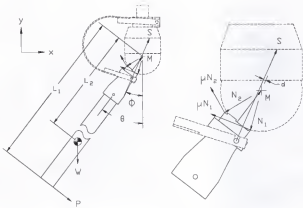


Figure 4-8: Static Free Body Diagram

At the limit between sliding of the socket over the sphere and tipping of the socket off the sphere, the normal force ( $N_2$ ) becomes zero [35]. An expression for the tipping force is then obtained by setting  $N_2$  equal to zero in Equation 4-4. The tipping force ( $P_{tip}$ ) is given in Equation 4-6.

$$P_{tip} = -(-S \sin(\phi) \mu r - M \sin(\theta) \mu r - \sin(\theta - \beta) S d + \sin(\theta - \beta) W L_2 \sin(\theta) - \mu \cos(\theta - \beta) S d + \mu \cos(\theta - \beta) W L_2 \sin(\theta)) / (-\cos(\theta) \mu r + \sin(\theta - \beta) L_1 + \mu \cos(\theta - \beta) L_1) \quad (4-6)$$

The maximum allowable static coefficient of friction may then be obtained by equating the expressions for  $P_{slide}$  and  $P_{tip}$  and solving for the unknown,  $\mu$ . In order to simplify this calculation, the values for the known variables were substituted into this equality. The known values for the limiting case (maximum tendency towards tipping) used in this calculation are given in Table 4-1.

Table 4-1: Maximum Coefficient of Friction Calculation Constants

Variable	Value
$\theta$	38°
$\phi$	23°
$d$	1.62 mm
$S$	8.9 N
$M$	11.1 N
$L_2$	304.8 mm
$L_1$	609.6 mm
$r$	19.05 mm
$\beta$	22.75°
$W$	8.9 N

The value for  $\mu$  is then obtained by solving the fourth order polynomial for the four roots and selecting the appropriate value. The equality ( $P_{slide} = P_{tip}$ ) with the variables

replaced by the values in Table 4-1 is shown in Equation 4-7. From the solution set, it was determined that the maximum allowable static coefficient of friction is 0.479. At higher values, the LBB socket will tend to tip off rather than slide around the tool sphere [35]. The next step, therefore, was to measure the coefficient of friction between commercially available coatings and the 440 SST tool sphere and select a coating which met the friction requirement at the lowest cost.

$$P_{slide} = P_{ap}$$

$$\frac{-75.91\mu^3 + 312.94\mu^2 - 128.64\mu + 312.80}{(-21.38\mu^2 - 22.13)(-5.85\mu + 23.15)} = \frac{-12.39\mu - 385}{22.56\mu + 6.31} \quad (4-7)$$

$$\mu = \begin{Bmatrix} 3.958 \\ 1.280 \\ 0.479 \\ 0 \end{Bmatrix}$$

#### Coefficient of Friction Measurements

Two commercially available coatings (S334B Teflon and amorphous diamond) were applied to several LBB sockets and the resulting static coefficient of friction measured using a strain-gage-based friction test stand [36].

The strain-gage-based friction test stand is shown in Figure 4-9. The main components are the base, support arms, strain-gage bridge mounted on a torsion member, the precision sphere and the socket. The first step in the measurement procedure was to calibrate the test stand. This was accomplished by measuring the strain induced in the torsion member by a known applied couple. The couple was placed on the torsion member by loading a shaft through the tube center by two equal and opposite forces

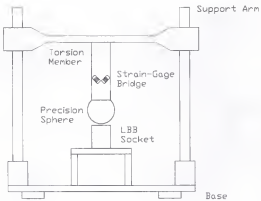


Figure 4-9: Friction Test Stand

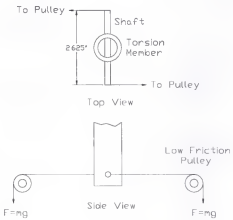


Figure 4-10: Calibration Couple

perpendicular to the shaft (see Figure 4-10). The moment ( $M$ ) produced by this couple is equal to the magnitude of the force multiplied by the distance ( $d$ ) between the two forces.

$$M = F * d \quad (4-8)$$

The strain in the full-bridge wheatstone circuit was measured for a range of applied torques using a Vishay V/E-20A Strain Gage Indicator. This unit contains a DC power supply and fixed gain differential amplifier which converts the change in resistance across the wheatstone bridge into microstrain and displays it on a digital readout.

A linear relationship between the applied torque and resulting strain was determined and the slope of a least squares best-fit line through the data points recorded. Once this relationship was obtained, the next step was to begin the actual friction measurements. The test procedure follows:

- 1) The shaft through the torsion member was removed and the 38.1 mm (1.5") diameter tooling ball attached with structural adhesive to the lower end.
- 2) A coated socket was placed on the socket support below the ball.
- 3) A known mass was placed directly above the ball to produce a normal force.
- 4) A torque was placed on the socket and the maximum strain just before movement was recorded.
- 5) Next, the value of the moment ( $M$ ) corresponding to the measured strain was calculated using the graph of the calibration data.
- 6) The externally applied friction force was then calculated assuming that a couple

was again applied. The friction force was then equal to the moment ( $M$ ), divided by the diameter of the socket ( $d_{socket}$ ).

- 7) Finally, the static coefficient of friction (SCOF) was found from the ratio of the friction force to the normal force.

$$SCOF = F_{friction} / N_{contact} \quad (4-9)$$

It is important to note that the normal force produced by putting a known weight above the ball is not the true normal used in the friction calculations since the ball is resting on a three-point contact socket. See Figure 4-11 for the actual geometry of the contact area. The equation for the normal used in the friction equation is given in Equation 4-10. The results of the friction measurements for S334B Teflon and amorphous diamond coated sockets on the 440 stainless steel tooling ball are shown in Table 4-2.

$$N_{contact} \cos(\theta) = N_{applied} \quad (4-10)$$

Table 4-2: SCOF Experimental Results

<u>S334B Teflon</u>			<u>Amorphous Diamond</u>		
$N_{applied}$ (g)	Strain (x1e6)	SCOF	$N_{applied}$ (g)	Strain (x1e6)	SCOF
500	4	.077	500	3	.114
700	5	.069	700	3	.082
900	6	.064	900	4	.084
1295	7	.052	1295	5	.073
1453.5	8	.053	1453.5	6	.078
1748.5	9.5	.053	1748.5	7	.076
2202	10.5	.046	2202	8	.069

$N_{applied}$ (g)	Strain (x1e6)	SCOF	$N_{applied}$ (g)	Strain (x1e6)	SCOF
500	4	.077	500	3	.114
700	5	.069	700	3	.082
900	6	.064	900	4	.084
1295	7	.052	1295	5	.073
1453.5	8	.053	1453.5	6	.078
1748.5	9.5	.053	1748.5	7	.076
2202	10.5	.046	2202	8	.069

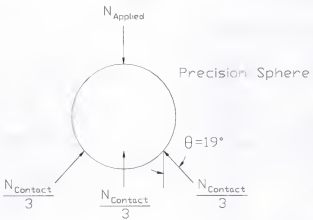


Figure 4-11: Contact Area Geometry

A statistical analysis of the SCOF data yielded a mean of 0.059 with a standard deviation (95% confidence level) of 0.011 for the Teflon data and a mean of 0.082 with a standard deviation of 0.015 for the amorphous diamond data. Both tested coatings showed SCOFs well below the calculated maximum value of 0.479. Further considerations included the wear characteristics or durability of each coating, the cost per part, and the coating thickness uniformity. Because the Teflon coating was nearly an order of magnitude less expensive than the amorphous diamond, the determining factor was cost and the LBB sockets were coated with S334B Teflon.

#### Tool Point Bracket

The bracket which supports the tool socket joint is shown in Figure 4-12. The sphere center of the joint is located on the spindle centerline with an offset (in the Z-direction) of 104.8 mm (4.125") from the face of a standard 50 taper tool holder.

The design constraint imposed on this item was a maximum deflection of  $1.5 \mu\text{m}$  at the cantilevered bracket end for a  $35.6 \text{ N}$  ( $8 \text{ lb}_f$ ) load,  $P$ . The experimental determination of this load is shown in Figure 4-13. The spring scale reading was recorded under static conditions ( $4 \text{ lb}_f$ ) and under a  $0.5 \text{ g}$  vertical acceleration ( $6 \text{ lb}_f$ ). The  $8 \text{ lb}_f$  value for the load was chosen as a worst case scenario.

The bracket cross-sectional dimensions were then calculated according to Equation 4-11. The material selected for the bracket was 301 SST due to its high elastic modulus and good corrosion resistance. For a square cross-sectional dimension ( $b$ ) of  $34.16 \text{ mm}$  ( $1.345"$ ), the cantilever deflection at the angled bracket end ( $q_p$ ) was calculated to be  $1.51 \mu\text{m}$ , which was at the limit of the design constraint.

$$\begin{aligned}
 q_r = & \frac{k}{GA} \int_0^{d_1} wx_1 dx_1 + \frac{1}{EI} \int_0^{d_1} \frac{wx_1^3}{2} dx_1 + \frac{k}{GA} \int_0^{(L_1-d_1)} (F + wx_2 + wd_1) dx_2 \\
 & + \frac{1}{EI} \int_0^{(L_1-d_1)} \left( Fx_2 + wd_1 x_2 + \frac{wd_1^2}{2} + \frac{wx_2^2}{2} \right) (d_1 + x_2) dx_2 \\
 & + \frac{1}{EI} \int_0^{L_1} \left( FL_1 - Fd_1 + \frac{wL_1^2}{2} \right) L_1 dy + \frac{1}{EA} \int_0^{L_1} (wd_2 + wL_1 + F) dy
 \end{aligned} \tag{4-11}$$

where  $F = 35.6 \text{ N}$

$$L_1 = 0.0928 \text{ m}$$

$$L_2 = 0.0921 \text{ m}$$

$$d_1 = 0.0222 \text{ m}$$

$$d_2 = 0.0342 \text{ m}$$

$$I = b^4/12 = 1.135e-7 \text{ m}^4$$

$$G = \text{Shear Modulus} = 75.98e9 \text{ N/m}^2$$

$$A = b^2 = 1.167e-3 \text{ m}^2$$

$$E = \text{Young's Modulus} = 193e9 \text{ N/m}^2$$

$$w = \text{Distributed Weight} = pgA = pgb^2 = 90.68 \text{ N/m}$$

$$k = \text{Correction Coefficient for Shear Strain} = 1.2 [33]$$

$x_1, x_2$ , and  $y$  = integration variables along length of bracket

Experimental verification of this bracket deflection analysis was also performed. A known force (37.8 N) was applied to the end of the bracket and the resulting deflection measured with a capacitance probe fixed to ground. The deflection predicted by the analysis for this force was 1.59  $\mu\text{m}$ , while the measured deflection was 1.4  $\mu\text{m}$ . The measured deflection was less than the prescribed design constraint and the design was, therefore, acceptable.

#### Optics Package

The optical configuration of the Michelson interferometer (aligned between the spheres at the ends of the LBB) for the first generation STLBB system will now be described. There were three main design considerations which defined the final optical layout. First, because the heterodyne laser signal is introduced into the interferometer through a single-mode, polarization maintaining fiber optic, it is necessary to generate a

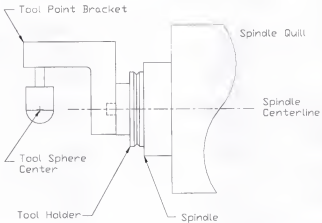


Figure 4-12: Tool Point Bracket

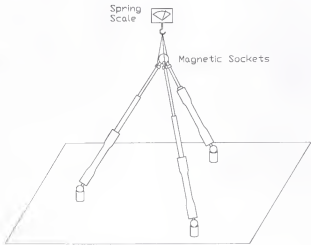


Figure 4-13: Spring Scale Measurement

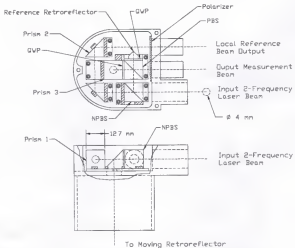


Figure 4-14: Optics Package

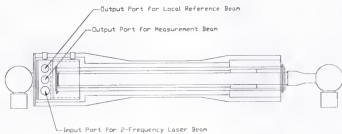


Figure 4-15: Optics Package Placement

local reference signal. This signal accounts for the unavoidable relative phase shifts between the two frequencies introduced by cable deformations. Second, aesthetically it was desired to place both the input and output fiber optic cables on the same side of the optics package. Third, as an overall design concern, the size of each component in the LBB must be minimized. The required optics and their configuration are shown in Figure 4-14. The position of the optics package within the LBB is shown in Figure 4-15.

Figure 4-14 shows the four millimeter diameter input laser beam at the lower right hand side of the top view. This beam is split into two components by the non-polarization beam splitter (NPBS). The transmitted portion (approximately 15%) is routed around the setup (via prisms 1 and 2) through a linear polarizer oriented at 45° to the two orthogonal polarizations in the heterodyne signal. The two frequency components then interfere at the polarizing filter. The interference signal is carried to a photodetector by a multimode (MM) fiber optic where the electronic local reference signal is generated.

The reflected portion from the NPBS travels to the Michelson interferometer. At the polarization beam splitter (PBS), the vertical (*s*) polarization is reflected and the horizontal (*p*) is transmitted. The linearly polarized *p* light then passes through a quarter wave plate (QWP), orientated at 45° to the light linear polarization, which converts the polarization state to circular. After three internal reflections within the retroreflector, the light returns parallel to itself and passes once again through the QWP. The circular polarization state is now transformed into linear, but now the polarization vector is rotated 90° with respect to the original orientation (a 180° relative phase shift between the electric and magnetic fields has occurred). The light returning from the reference retroreflector is therefore functionally *s* light and is reflected at the PBS.

The *s* light originally reflected by the PBS follows an analogous path, except for the 90° turn imposed by total internal reflection in prism 3 (attached to the corresponding QWP). When the two light beams (with some relative Doppler phase shift) recombine at the PBS and pass through the polarizing filter (oriented at 45° to either linear polarization), they also interfere and are carried to the measurement photodetector (again on a MM fiber). Any phase change in the local reference signal is then subtracted from the measurement signal by the system electronics to obtain the final measurement signal which represents the actual retroreflector motion.

In order to secure an interference signal (in the Michelson interferometer portion of the optical layout), the return beam from the moving retroreflector must overlap the beam from the reference retroreflector. This requires a positioning system which provides both translational and angular adjustments of the optics package relative to the moving retroreflector.

The four degree-of-freedom device which provides these adjustments is shown in Figure 4-16. The top two adjustment screws provide pitch and vertical translations, while the two side screws allow yaw and horizontal motions. The fifth screw oriented at 135° to the other screws serves as a locking mechanism. Three important design considerations to note are: 1) the dimple under the screw marked 'A' prevents axial motions of the optics package within the LBB, 2) the fine pitch of all screws (80 threads per inch) allows the necessary precise adjustments, and 3) the locking screw is spring-loaded so constant adjustment of this screw while aligning the interferometer is unnecessary.

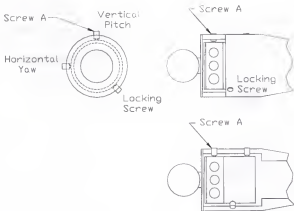


Figure 4-16: 4-DOF Positioning Mechanism

Error Budget

In order to predict the final accuracy of the STLBB system, it was necessary to identify each error source and tabulate these errors in an error budget. Error budgets are typically used in the design process to select components or processes which will meet the required system accuracy. In this case, Mize had previously outlined an error budget for the first generation laser ball bar, so the primary error sources had already been characterized [27]. Mize's work has been modified for the STLBB error budget. Twelve key error sources are described and quantified in the following paragraphs. In the error calculations, the error has been calculated as the difference between the measured and actual values and individual errors have been assumed to be independent of the others.

### 1) Thermal Error Due to Unsensed Length

An interferometer measures the relative path difference between the reference and measurement paths. In the LBB, the reference path is fixed inside the optics package, while the measurement path changes with the motion of the moving retroreflector mounted at the end of the telescoping tubes. Ideally, the measurement path would include the entire LBB length (sphere center to sphere center). In reality, there are portions of the LBB total length outside the measurement path. The portion of the LBB outside this path represents the unsensed length (see Figure 4-17). Changes in this length due to thermal variations over the course of a measurement introduces an error. For example, if the spheres at the end of the LBB were fixed in two, thermally stable magnetic sockets and the unsensed length expanded due to a temperature increase, the interferometer would

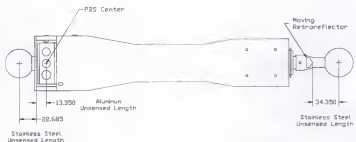


Figure 4-17: LBB Unsensed Length

show a decrease in displacement although the overall length had not changed.

Alternately, if the LBB was unconstrained and the unsensed length increased, the interferometer would not show a change in displacement even though the overall length was now greater. This error can be calculated according Equation 4-12. Figure 4-17 shows an unsensed length of 57.035 mm in 304 stainless steel and 13.350 in 6061-T6 aluminum. The coefficients of thermal expansion,  $\alpha$ , are 17.8 ppm/ $^{\circ}$ C for 304 stainless steel and 24.3 ppm/ $^{\circ}$ C for the 6061-T6 aluminum [32]. For a temperature change of 0.25 $^{\circ}$ C, these values give a total error of  $\pm 0.335 \mu\text{m}$ .

$$\text{error}_{\text{unsensed}} = [(\alpha L)_{\text{ss}} + (\alpha L)_{\text{al}}] \Delta T, \quad \begin{aligned} &\text{where } L = \text{unsensed length} \\ &\Delta T = \text{temperature change} \end{aligned} \quad (4-12)$$

## 2) Cosine Error

This error is inherent to linear displacement interferometers. If the laser beam is not exactly parallel with the direction of motion, a proportional error (i.e., one which increases with the measurement distance) will be established which is a function of the angle of misalignment [28]. The cosine error may be calculated according to Equation 4-13. The angle of misalignment ( $\theta$ ) is found by measuring the lateral offset of the return beam from the moving retroreflector. The angle is related to the return offset according to Equation 4-14. Because He-Ne laser beams have a Gaussian cross-sectional intensity profile, it is difficult to visually resolve the edge of the beam to find the exact return offset. The best case resolution of this lateral displacement was assumed to be 0.5 mm. This gives a cosine error of 0 to -0.066  $\mu\text{m}$  for an angular misalignment of 0.03 $^{\circ}$ .

$$\text{error}_{\text{cone}} = L (\cos \theta - 1), \quad \text{where } L = \text{range of motion} = 470.5 \text{ mm} \quad (4-13)$$

$$\theta = \tan^{-1} (\text{offset} / 2L) \quad (4-14)$$

### 3) Sphere/Motion Misalignment

This error is present when the center of one of the spheres at the end of the LBB does not lie on the line defining the direction of tube extension. This situation is shown in Figure 4-18. For no offset, the change in displacement of the LBB ( $\Delta L$ ) is equal to the difference between final and initial lengths ( $L'$  and  $L$ , respectively). However, a lateral offset of one sphere from the line of displacement due to incorrect assembly will result in a difference between the sphere center displacement and the recorded displacement. This error is equal to the difference between the change in displacement recorded by the interferometer and the actual change in displacement between sphere centers (see Equation 4-15). For a measured sphere center offset of 0.25 mm, a maximum change in displacement of 470.5 mm and an initialization length ( $L$ ) of 425.7 mm, the total error is 0 to 0.039  $\mu\text{m}$ .

$$\begin{aligned}\text{error}_{\text{misalign}} &= \Delta L - (L' - L) \\ &= \Delta L - [L^2 + 2\Delta L (L^2 - \text{offset}^2)^{0.5} + \Delta L^2]^{0.5} + L\end{aligned} \quad (4-15)$$

### 4) Deadpath Error

When the measurement and reference path lengths are not equal at initialization (the zero displacement point), deadpath error, or DPE, is introduced for any

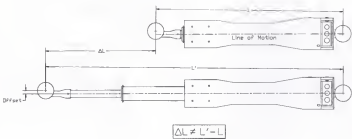


Figure 4-18: Sphere/Motion Misalignment

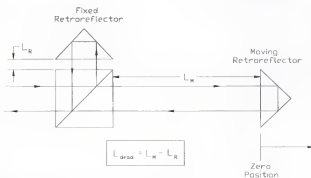


Figure 4-19: LBB Interferometer Deadpath

uncompensated change in environmental conditions during the measurement. Since it is impossible to know the exact temperature, pressure, humidity, and air composition at all times, deadpath error is present in all linear displacement interferometers with unequal reference and measurement optical path lengths. The deadpath distance ( $L_{\text{dead}}$ ) is equal to the difference between the reference ( $L_R$ ) and measurement ( $L_M$ ) optical path lengths at the zero position (see Figure 4-19). The DPE, which is proportional to this distance, is given in Equation 4-16.

$$\text{DPE} = \Delta n L_{\text{dead}} / n, \quad \text{where } \Delta n = \text{change in refractive index} \quad (4-16)$$

$n = \text{nominal value of index of refraction}$

The change in the refractive index of air ( $\Delta n$ ) due to environmental fluctuations may be calculated using Edlen's equation [29] (see Equation 4-17). The nominal index of refraction can be calculated as 1.000271295 under the conditions of standard temperature and pressure. The conditions for standard temperature and pressure (STP) are: pressure = 760 mm Hg (101323.2 Pa), temperature = 20 °C (68 °F), and relative humidity = 50%. The atmospheric content of carbon dioxide, CO<sub>2</sub>, may be taken to be 355 parts per million (ppm). For a change in any one of these values, however, the refractive index will change. From Equation 4-17, it can be seen that there is a larger dependence of the refractive index on temperature and pressure than humidity and CO<sub>2</sub>.

$$n = 1 + 271.8e-6 (P / 101325) (293.15 / T)^* \quad (4-17)$$

$$(1 + 0.54(CO_2 - 300)/1e6) - 1e-8 H,$$

where: P = Pressure (Pa)  
T = Absolute temperature ( $^{\circ}$ K)  
 $\text{CO}_2$  = Carbon dioxide content (ppm)  
H = Relative humidity (%)

In order to compensate for the atmospheric changes during a measurement, transducers are used to measure the temperature, pressure, and humidity in real time. A barometer with an accuracy of  $\pm 0.3$  hPa ( $\pm 0.225$  mm Hg) was selected to measure the pressure [30]. Thermistors ( $\pm 0.1$   $^{\circ}$ C) were chosen to measure the ambient temperature. The relative humidity is measured with an accuracy of  $\pm 5\%$  using a commercially available digital hygrometer. For these accuracies, the uncertainty ( $\Delta n$ ) in the compensated value of the index of refraction was found to be  $1.232\text{e-}7$ . For this value of  $\Delta n$  and a dead path length ( $L_{\text{dead}}$ ) of 338.97 mm, the dead path error is found to be  $\pm 0.042$   $\mu\text{m}$ .

### 5) Environmental Error

A change in the index of refraction of air due to environmental fluctuations during a measurement effectively changes the length of the "yardstick" used to find displacement. As the refractive index increases (e.g., due to an increase in temperature), the wavelength in air decreases and the measured displacement is greater than actual (positive error). In this case, the imaginary pipeline of Chapter 3 is being filled with smaller  $\lambda$ s, so more will fit in the pipe. Therefore, a count of the number of  $\lambda$ s in the pipe increases and it appears that the moving retroreflector has been displaced away from the PBS.

The environmental error magnitude is given in Equation 4-18, where D is the LBB range of motion. Uncertainties in the value of the temperature, pressure, and humidity

again cause an uncertainty in the compensated value of the refractive index. For the same values of these uncertainties as in the previous section, this gives a value of 1.232e-7 for  $\Delta n$  and an error of  $\pm 0.058 \mu\text{m}$ .

$$\text{error}_{\text{environment}} = \Delta n D / n, \quad \text{where } D = 470.5 \text{ mm} \quad (4-18)$$

#### 6) Sphericity of Ball/Socket

The form (sphericity) of the spheres mounted at each end of the LBB determines the motion of the sphere center as the LBB is rotated in the three-point contact magnetic sockets. For an imperfect form, the sphere center will trace some path in space rather than remaining at a single point. The 1.5" diameter spheres used in this research were reported to have a sphericity of  $\pm 5 \mu\text{in}$  (grade 5). This total form tolerance provides a maximum radial deviation of the sphere surface from the theoretical center of  $\pm 2.5 \mu\text{in}$  ( $\pm 0.06 \mu\text{m}$ ). Assuming a worst case scenario, the individual errors of the two spheres could combine to give a total error of  $\pm 0.13 \mu\text{m}$ .

#### 7) Initialization Fixture

The three socket initialization fixture described in Chapter 1 is again shown in Figure 4-20. In this figure, it can be seen that the socket centers do not lie on a single line. The offset may have components in both the X and Y coordinate directions. The general case of offset components in both coordinates is shown in Figure 4-20. The possibility of these offsets is inherent to the three socket fixture because there is a finite tolerance associated with the manufacturing process and socket location. The error can be

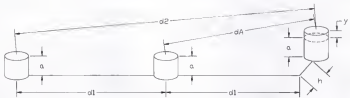


Figure 4-20: Initialization Fixture Offsets

calculated according the Equation 4-19. For an error in each offset of 0.025 mm and an initialization length ( $d_1$ ) of 425.7 mm, the error is 0 to -7.34e-3  $\mu\text{m}$ .

$$\text{error}_{\text{minsize}} = (4d_1^2 + h^2 + y^2)^{0.5} - (d_1^2 + h^2 + y^2)^{0.5} - d_1 \quad (4-19)$$

where  $d_1$  = distance from socket 1 to socket 2

$d_2$  = extended length

$h$  = lateral offset distance

$y$  = vertical offset distance

## 8) Laser System Errors

The components of the heterodyne laser system which affect the measurement accuracy and repeatability are: the laser wavelength stability, the polarization characteristics of the laser beam, interferometer errors, and electronics linearity. These error sources are intrinsic to all heterodyne linear displacement interferometers. The values associated with the commercial system used in this research (Zygo ZMI 2001) will be given in the following paragraphs.

The metric used for linear displacement measurements is the wavelength of the He-Ne laser light. The fractional stability and accuracy of the measured displacement is equal to the fractional wavelength stability of the laser source (provided all other errors are fixed). For the laser head used in this research, the stability is specified as  $\pm 0.01$  ppm ( $\mu\text{m}/\text{m}$ ) over a 24 hour period [31]. For a fully extended LBB length of 896.225 mm, this gives an error of  $\pm 8.96\text{e-}3 \mu\text{m}$ .

The laser beam carries the two heterodyne frequencies in orthogonal polarizations. Ideally, these two polarizations are perfectly orthogonal. In reality, they are not normal

and each contains residuals of the other frequency component. This is termed polarization mixing and introduces a cyclic displacement error. The magnitude of this error is given as  $\pm 0.8$  nm in [31].

In the interferometer, errors arise from two sources: polarization mixing and thermal effects. The polarization mixing due to imperfect optical coatings is estimated to be  $\pm 0.8$  nm (for initially perfectly orthogonal frequencies in the incident beam). A uniform change in the ambient temperature can introduce a relative change in the glass path distance between the measurement and reference legs of the interferometer. For a linear displacement interferometer, this error is given as  $0.01 \mu\text{m}/^\circ\text{C}$  [31]. If the ambient temperature change is taken to be  $\pm 0.25$   $^\circ\text{C}$ , the error value is  $\pm 2.5 \times 10^{-3} \mu\text{m}$ .

The electronics error is introduced by the extension of the system resolution. The single pass (Michelson) interferometer resolution of  $\lambda/2$  is divided by 127 electronically to produce a resolution of  $\lambda/254$ . The error is equal to the quantization error of the system electronic counter and is given as  $\pm 10$  nm [28][31].

For a nominal change in the ambient temperature of  $\pm 0.25$   $^\circ\text{C}$  and a maximum LBB length of 896.225 mm, the sum of these errors is  $\pm 0.022 \mu\text{m}$ .

#### 9) Beam Misalignment from Optic Rotation

Due to structural deflections and angular compliance in the telescoping tube's bearings, the interferometer and moving retroreflector rotate about their respective sphere centers. These angular rotations cause the laser beam to become misaligned with the direction of motion and shorten the measured displacement relative to the actual displacement between the sphere centers.

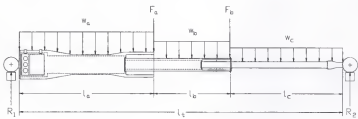


Figure 4-21: Castigliano Model Loading Conditions

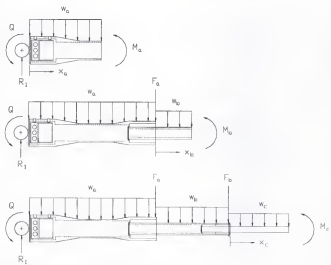


Figure 4-22: LBB Moment Calculation Sections

The rotations of the interferometer and moving retroreflector were calculated using Castigliano's Theorem on Deflections [33]. The loading conditions for these calculations are shown in Figure 4-21. In this figure, the distributed forces due to component weights are denoted with a subscripted  $w$ , the forces marked  $F$  are the bearing weights and the reaction forces are labeled with an  $R$ . In order to simplify the calculations, the  $F$  forces also include the weight of the tubes inside the bearings and are assumed to be concentrated at a single point. The total LBB length ( $l$ ) was divided into sections at obvious discontinuities. Each of these section lengths are denoted by a subscripted  $l$ .

The first step in this solution was to calculate the reaction forces ( $R_1$  and  $R_2$ ) as a function of the external loads and an imaginary moment ( $Q$ ). The imaginary moment was placed at the point where the rotation was to be determined (i.e., the left or right sphere centers). The resulting moment equations along the length of the structure from the imaginary moment, external loads, and reaction forces were then calculated. There were discontinuities of force and cross-section along the LBB, so several moment equations were written along the beam length. Next, the partial differentials of these moment equations with respect to the imaginary moment  $Q$  were calculated. The final rotation (in the direction of  $Q$ ) was calculated according to Equation 4-20, where all terms which contain  $Q$  are now set equal to zero. The values for Young's modulus ( $E$ ) and the cross-sectional moment of inertia ( $I$ ) are also included in this integration.

$$\theta_Q = \sum_{i=1}^N \frac{1}{E_i I_i} \int_0^{l_i} M_i \frac{\partial M_i}{\partial Q} dx_i, \quad \text{where } N = \# \text{ of beam sections} \quad (4-20)$$

As an example, consider the calculation of the rotations about the left sphere, which corresponds to a rotation of the interferometer (see Figure 4-1). The LBB length was divided into three sections due to cross-sectional area discontinuities. These sections are shown in Figure 4-22. The resulting moment equations for these sections are listed in Equation 4-21.

$$M_a = -Q + R_1 x_a - 0.5 w_a x_a^2 \quad (4-21)$$

$$M_b = -Q + R_1 (l_a + x_a) - F_b x_b - w_a l_a (l_a/2 + x_b) - w_b x_b^2/2$$

$$M_c = -Q + R_1 (l_a + l_b + x_c) - F_a (l_b + x_c) - F_a x_c - w_a l_a (l_a/2 + l_b + x_c) - w_b l_b (l_a/2 + x_c) - w_c x_c^2/2$$

$$\text{where } R_1 = Q/l_a - F_a l_a/l_a - F_b l_b (l_a + l_b) - w_a l_a^2/(2l_a) - w_b l_b/l_b (l_a + l_b/2) - w_c l_c/l_a (l_a + l_b + l_c/2) + w_a l_a + w_b l_b + w_c l_c + F_a + F_b$$

Using Maple V Release 4.0™, the partial differentials ( $\delta M / \delta Q$ ) and the total integral were calculated. The resulting angular rotation about the left sphere center ( $\theta_L$ ) in Figure 4-21 was  $-1.9199e-4$  radians ( $-0.011^\circ$ ) in the direction of  $Q$ . Similarly, the rotation about the right end ( $\theta_R$ ) was calculated to be  $6.5990e-4$  radians ( $0.038^\circ$ ) in the same direction.

The other source of rotations and resulting angular misalignment is the angular compliance ( $\theta_{BC}$ ) in the linear ball bearings used to support the middle and inner telescoping tubes. A value of  $3.5e-4$  radians ( $0.02^\circ$ ) was chosen for this compliance. This conservative value was based, in each case, on the amount of play in the bearing over its full length. The rotations at the left and right sphere centers ( $\theta_{BL}$  and  $\theta_{BR}$ ) due to this angular compliance may be calculated according to Equation 4-22. Substituting the

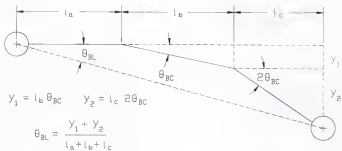


Figure 4-23: Left Sphere Total Angular Rotation

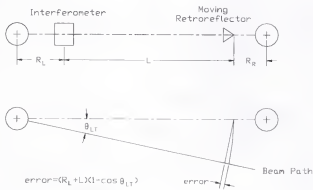


Figure 4-24: Cosine Error Due to Interferometer Rotation

appropriate values into this equation, rotational values of 3.1422e-4 radians (0.018°) and 3.8578e-4 radians (0.022°) were found for the left and right sphere centers, respectively.

The formulation of the left sphere equation, which accounts for the bearing compliance, is shown in Figure 4-23. This figure shows the compliance at each of the two extending tubes and the resulting total angular rotation at the left sphere center as a function of the bearing rotations.

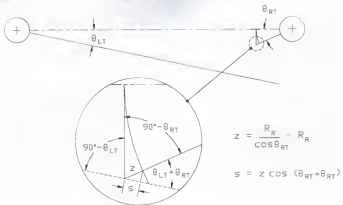
$$\theta_{BL} = (l_b \theta_{BC} + l_c 2\theta_{BC}) / (l_a + l_b + l_c) \quad (4-22)$$

$$\theta_{BR} = (l_b \theta_{BC} + l_c 2\theta_{BC}) / (l_a + l_b + l_c)$$

The total angular rotations ( $\theta_{LT}$  and  $\theta_{RT}$ ) at each end of the LBB were then taken as the sum of the structural and bearing compliance rotations. For the left sphere center, the total rotation ( $\theta_{LT}$ ) was 5.0621e-4 rad (0.029°). The right sphere center rotation ( $\theta_{RT}$ ) was found to be 1.0457e-3 rad (0.0599°). Once these values for the optic's rotations were known, an examination of the geometry of the optical path difference caused by the angular misalignment was used to derive the linear measurement error.

Rotation of the interferometer about its sphere center caused a familiar cosine error. The measured path is shorter than the actual path by an amount proportional to the angular misalignment  $\theta_{LT}$ . This error is shown in Figure 4-24.

As the moving retroreflector rotates about its sphere center (the right sphere in Figure 4-1), an error, which is a function of both the angles  $\theta_{LT}$  and  $\theta_{RT}$ , is introduced. The error geometry is shown in Figure 4-25. The total error introduced by these rotations is given in Equation 4-23. Substitution of the full length dimensions of the LBB into this



$$z = \frac{R_R}{\cos \theta_{RT}} - R_R$$

$$s = z \cos (\theta_{RT} + \theta_{LT})$$

Figure 4-25: Moving Retroreflector Rotation

equation gives a final error of 0 to -0.084  $\mu\text{m}$ . This error is zero for a vertical LBB orientation and maximally negative when the LBB is horizontal.

$$\text{error}_{\text{rotation}} = (R_L + L)(\cos\theta_{LT} - 1) + R_R \left( \frac{1}{\cos\theta_{RT}} - 1 \right) \cos(\theta_{LT} + \theta_{RT}) \quad (4-23)$$

where  $R_L$  = distance from left sphere center to interferometer

$R_R$  = distance from right sphere center to retroreflector

#### 10) Incident Polarization Alignment

This error is a result of imperfect alignment between the optical axes of the incident two-frequency light and the polarization beam splitter. If the laser polarization axes are rotated with respect to the PBS axes, polarization mixing results. This results in a periodic or cyclic error in the measurement signal (i.e the error does not grow infinitely with distance, but oscillates sinusoidally during retroreflector motion). For a worst case optical axis alignment error of  $\pm 1^\circ$  and a maximum misalignment of the incident beam with the PBS face of  $1^\circ$ , a total measurement error of  $\pm 8.2\text{e-}4 \mu\text{m}$  is assumed [27].

#### 11) Fiber Optic Phase Shifting

In situations where the laser light is fed to the heterodyne interferometer through a single mode, polarization maintaining fiber, any change in the optical path in the fiber between the orthogonal axes of the two frequencies results in a relative phase shift between the two waves. Since the displacement information is carried in the phase in AC systems, this is seen as motion of the moving retroreflector when none has occurred. Changes in the optical path length between the two linearly polarized waves may be

caused by both mechanical and thermal deformations of the fiber. For radical, temporally varying deformations, the phase shift between the two beams may appear random. In this case, the constant initial phase condition of the source will not be met, coherence will be reduced and poor interference patterns will result. However, the cable-induced phase changes tend to be slowly varying and may be compensated.

In the LBB design, the local reference removes any quasi-static phase changes due to the fiber optic cable. Any mechanically-induced phase shift will be common to both the reference and measurement signals. Therefore, taking the difference of the local reference and measurement signals attenuates this error.

## 12) Elastic Elongation

When the components of the LBB outside the interferometer path (unsensed length) are subjected to an axial loads, they deform. An elongation at the upper sphere can be expected due to the weight of the corresponding tube and a contraction is seen at the lower sphere due to the remaining weight of the LBB. The elastic deformation may be calculated according to the simple formula shown in Equation 4-24 for simple tension or compression [34]. The worse case condition of a vertical LBB orientation will be assumed for calculations. An LBB normal orientation with the interferometer at the bottom sphere and the moving retroreflector at the top is assumed.

$$\delta = F l / (A E), \quad \text{where } F = \text{applied axial load} \quad (4-24)$$

l = length of support member  
A = cross-sectional area  
E = Young's modulus

At the top sphere, the unsensed length between the retroreflector apex and the sphere elongates under the combined weights of the inner telescoping tube (3.15 N), the middle telescoping tube (8.41 N) and the pair of linear bearings inside the middle tube (2.22 N) in a worst case scenario. For this tensile force of 13.79 N, a cross-sectional area of  $3.593e-5 \text{ m}^2$  of the stainless steel socket and a length of  $15.1e-3 \text{ m}$ , an elongation of  $0.0304 \mu\text{m}$  is experienced.

At the lower sphere, the remaining weights of the main tube (8.53 N) and the linear bearing which supports the middle tube (6.45 N) tend to compress the unsensed length. If this compression is assumed to be localized at the small diameter between the outer tube and sphere, a deflection of  $1.129e-3 \mu\text{m}$  is predicted. The total error is the difference between these two and varies from  $0 \mu\text{m}$  in a horizontal position to  $-0.029 \mu\text{m}$  in the vertical orientation.

These 12 errors will now be collected in an error budget and the final system accuracy estimated. The individual errors may be accumulated in various manners to give the final accuracy. The arithmetic sum and root sum squared (RSS) methods have been chosen here [27].

Two error calculations have been completed. First, the LBB initialization accuracy was established because the LBB length is determined by a measurement of its own displacement. The applicable errors are: the Cosine Error (2), Sphere/Motion Misalignment (3), Deadpath Error (4), Environmental Error (5), Initialization Fixture (7), Laser System Errors (8), Beam Misalignment from Optic Rotation (9) and Incident Polarization Alignment (10). The remaining errors were neglected for the following reasons. The Thermal Error Due to Unsensed Length (1) was assumed to have no effect

because the thermal time constant of the material is much larger than the time for initialization and a large temperature fluctuation isn't expected over the short measurement time. Fiber Optic Phase Shifting (11) is attenuated by the local reference at each LBB. The Sphericity of Ball/Socket Error (6) was ignored because the spheres are not required to rotate in the three-point contact sockets during initialization. Finally, there is no contribution from Error 12 (Elastic Elongation) because the LBB is initialized in a horizontal orientation.

Second, the overall system accuracy was determined. This number includes the expected initialization accuracy as well as all 12 individual errors. The error budget is summarized in Table 4-3 shown on the following page. The arithmetic sum and RSS values for the initialization and final accuracy are also given. The final system accuracy predicted by the arithmetic sum is +0.786, -1.051  $\mu\text{m}$  and 0.402, -0.474  $\mu\text{m}$  using the RSS method.

Table 4-3: Error Budget

	Error Source	+ Error	- Error ( $\mu\text{m}$ )
1	Thermal Error Due to Unsensed Length	0.335	-0.335
2	Cosine Error	0.0	-0.066
3	Sphere/Motion Misalignment	0.039	0.0
4	Deadpath Error	0.042	-0.042
5	Environmental Error	0.058	-0.058
6	Sphericity of Ball/Socket	0.127	-0.127
7	Initialization Fixture	0.0	-0.007
8	Laser System Errors	0.022	-0.022
9	Beam Misalignment from Optic Rotation	0.0	-0.084
10	Incident Polarization Alignment	0.0008	-0.0008
11	Fiber Optic Phase Shifting	0.0	0.0
12	Elastic Elongation	0.0	-0.029
<b>Initialization Accuracy</b>		Sum	0.162
		RSS	0.084
<b>System Accuracy</b>		Sum	0.786
		RSS	0.402
			-1.051
			-0.474

## CHAPTER 5 DYNAMIC MEASUREMENT RESULTS

### Initialization Repeatability

Before the three LBBs of the STLBB system can be used to measure spatial coordinates through simultaneous trilateration, each must be initialized to determine the sphere center to sphere center length. The initialization procedure (for each LBB) is composed of three steps. First, the LBB is placed between sockets 1 and 2, and the displacement counter zeroed. Next, the LBB is extended from socket 2 to 3, and the displacement recorded. This displacement is the distance between sockets 2 and 3. Finally, the LBB is placed between sockets 2 and 3, and the length of the LBB initialized to the previously recorded displacement (see Figure 5-1). Since three LBBs are used simultaneously in this research, an important consideration is the repeatability of this procedure.

Aside from the individual initialization of each LBB, the full initialization algorithm contained another important consideration. Since all three LBBs were attached to a single sphere at the tool point during measurements (two by magnetic socket and one by threaded connection), this single sphere had to be used to initialize the three individual LBBs. To accomplish this task, the two LBBs with magnetic connections were initialized first. The sphere was then rigidly attached to the final LBB and its length initialized. The entire procedure is easily performed in approximately two minutes.

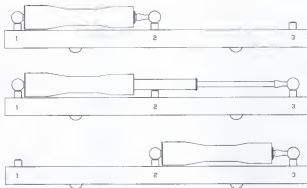


Figure 5-1: LBB Initialization Procedure

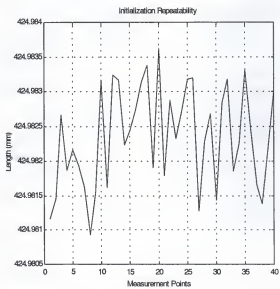


Figure 5-2: LBB Initialization Repeatability

To test the individual initialization repeatability, several consecutive measurements were completed and the results recorded. Although this test was performed in a temperature-controlled environment, heat from the operator's hands was introduced into both the LBB and initialization fixture. Therefore, the experimental results include thermally-induced length changes. Figure 5-2 shows the initialization repeatability over 40 consecutive tests for a single LBB. The results show a standard deviation of 0.72  $\mu\text{m}$  about an average initialization length of 424.982 mm.

### 2-D Measurements

In previous research, it was shown that the LBB is capable of dynamic measurements by comparing dynamic sequential trilateration measurements of a 2-D circular path to the radial error motions of the spindle used to generate the circular path [8][39]. The measurement trigger for the three consecutive runs (required for sequential trilateration) was the spindle encoder position. This measurement trigger required a complicated interface with the machine tool. To make the measurement system portable, it becomes necessary to eliminate the complicated interface.

The purpose of this work, therefore, was to verify simultaneous trilateration LBB measurements (as an alternative to the sequential trilateration method previously explored). In this case, a time-based sampling trigger could be utilized since all three leg measurements are obtained simultaneously. Therefore, no complicated interface with the CNC machine tool is required (i.e., no spindle encoder monitoring). Ideally, a verification device would be selected which could measure the same 3-D dynamic contours as the STLBB system. However, the closest match to this 3-D dynamic requirement was

provided by an optical grid encoder, which is capable of 2-D dynamic measurements. The grid encoder used in this research was provided by the Heidenhain Corporation.

The Heidenhain KGM 101 Grid Encoder is composed of a 140 mm diameter grid plate with a waffle-type grating of closely spaced lines (4  $\mu\text{m}$  signal period) and a non-contact scanning head which is able to measure translations in two directions. The optical grid plate is attached to an aluminum mounting base. This base is mounted in the plane to be measured (on an X-Y table for instance) and the scanning head is fixed perpendicular to the plate (e.g., on the Z axis attached to the spindle). This system measures the relative planar motion of the two bodies for any curvilinear path in the plane of the mounting base with a resolution of 4 nm and accuracy of  $\pm 2 \mu\text{m}$ . The recorded motions allow the user to observe the dynamic effects of the machine tool's performance on 2-D CNC tool paths. Figures 5-3 and 5-4 show the Heidenhain and STLBB setups used for the 2-D measurements. Note that the measurement point is on the spindle centerline with the same Z direction offset for both experimental setups. Therefore, geometric error variations within the work volume will not introduce a relative difference between the measurements (due to an Abbe' offset). Additionally, the CNC programs for both the STLBB and Heidenhain tests were executed from the same starting coordinates so, again, any geometric variations within the machine tool's work volume would be minimized. Finally, the part programs were run in the same order from a cold machine state to minimize thermal deviations between the two sets of tests.

Several planar contours were selected to be measured with both the Heidenhain grid encoder and STLBB system. These contours and the pertinent dimensions are summarized in Figure 5-5. The data gathered from the Heidenhain measurements was

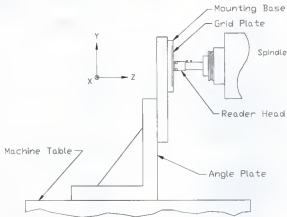


Figure 5-3: Heidenhain Grid Plate Setup

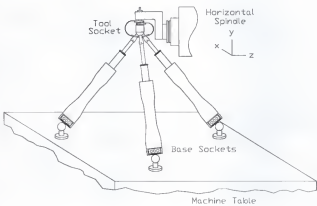


Figure 5-4: STLBB Setup

adequate to fully verify the STLBB measurements based on the following three-point argument. First, the STLBB system requires no special alignment of its axes with the machine tool's coordinate system and, in general, they are not aligned. Second, although the commanded path is in two dimensions with respect to the machine tool, the spatial coordinates of this path lie in three dimensions in the STLBB system. (The positions are then transformed in the machine's coordinate system using a rotation matrix obtained by an independent LBB measurement to give the final 2-D results in machine coordinates.) Third, a typical contour will require extension or contraction of all three individual LBBs, a rotation of the LBBs within their respective sockets (change in angular orientation), or both. Therefore, even though the commanded path lies in two dimensions in a coordinate frame external to the STLBB system, the path seen by the STLBB system and the required motions of the individual LBBs are three-dimensional in nature.

Comparisons between the Heidenhain and STLBB measurements will now be presented. Each of the six verification contours (angle, step, sultan, square, triangle, and circle) will be visited separately in the following paragraphs. All paths were executed at constant accelerations (i.e., trapezoidal velocity profiles) of 0.1 to 0.5g with feed rates ranging from 35 to 70 inches per minute (ipm). Additionally, the machine axes were preloaded in the positive X and Y directions prior to execution of each CNC contour and a nominal sampling frequency of 1 kHz was employed.

#### Angle

The angle path includes motions in the X-Y plane which require linear interpolation in the two axes simultaneously. Figure 5-6 shows a comparison between the

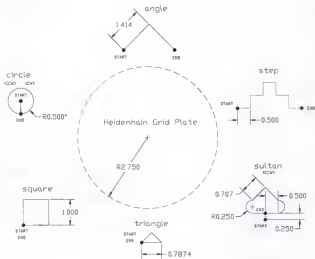


Figure 5-5: STLBB Verification Contours

Heidenhain grid plate and STLBB measurements for a feed of 35 ipm and an acceleration of 0.1g (0.98 m/s<sup>2</sup>). Only the cornering portion of the path is shown to enhance the viewing resolution. Figure 5-7 exhibits the two measurements for a feed of 70 ipm and an acceleration of 0.5g (4.9 m/s<sup>2</sup>).

#### Step

The step path includes linear interpolation in the X and Y axes individually and sharp corners with both positive and negative Y-direction motions. Figure 5-8 shows a comparison between the Heidenhain and STLBB measurements for the first cornering motion (+X to +Y) in the path at a feed rate of 70 ipm and an acceleration of 0.1g's. Figure 5-9 displays the same contour section at a feed of 70 ipm and 0.5g acceleration.

#### Sultan

The sultan path combines simultaneous X-Y linear interpolation with circular interpolation and single axis linear interpolation. A small section of the measured path has been highlighted in Figures 5-10 and 5-11. This section corresponds to the first transition from circular to linear interpolation in the contour (i.e., the right hand side of the path directly above the counter-clockwise circular section). Figure 5-10 displays the measurement comparison at 35 ipm feed and 0.1g acceleration. Figure 5-11 shows the contour section at 70 ipm feed and 0.1g acceleration.

#### Square

The square path provides linear interpolation in the X and Y coordinate directions as well as motions in both positive and negative directions. The results for a 70 ipm, 0.5g

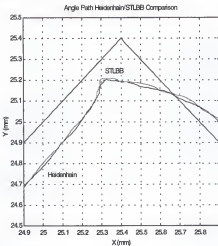


Figure 5-6: Angle Path Comparison (35 ipm, 0.1g)

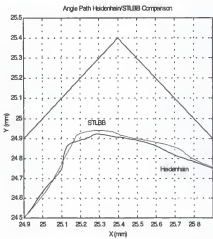


Figure 5-7: Angle Path Comparison (70 ipm, 0.5g)

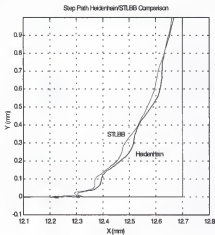


Figure 5-8: Step Path Comparison (70 ipm, 0.1g)

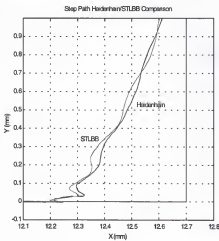


Figure 5-9: Step Path Comparison (70 ipm, 0.5g)

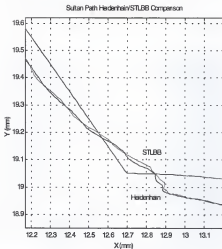


Figure 5-10: Sultan Path Comparison (35 ipm, 0.1g)

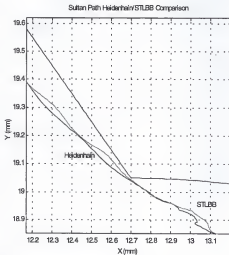


Figure 5-11: Sultan Path Comparison (70 ipm, 0.1g)

contour are shown in Figure 5-12. The displayed section is the upper right corner of the counter-clockwise square (i.e., the transition from +Y to -X motion).

#### Triangle

The triangle path is similar to the angle contour, but also provides a closed-loop path and negative X-direction motion. Figure 5-13 shows a comparison between the Heidenhain and STLBB results for the lower right hand portion of a path executed at 70 ipm and 0.2g. This contour section represents the X-motion reversal of the counter-clockwise triangle.

#### Circle

A counter-clockwise circular path was also measured using the two measurement systems. Figure 5-14 displays the measurement results for a commanded velocity of 70 ipm, where the deviations of the measured path from the commanded have been amplified by a factor of five. The figure shows an elliptical distortion of the path with the major axis of the ellipse rotated 45° counter-clockwise from the positive Y-axis. The explanation for this common path distortion will be given in the "2-D Contouring Accuracy" section to follow.

#### Dynamic/Static Repeatability

In all cases outlined in the previous paragraphs, good agreement is found between the Heidenhain and STLBB measurements. Changes in the contour velocity and acceleration can be seen to affect the dynamic contouring accuracy (e.g., off-path velocity lag and undershoot), but do not seem to disturb the agreement between the Heidenhain and STLBB results.

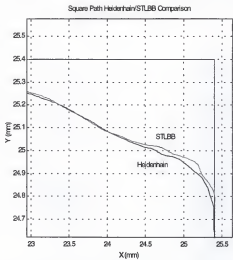


Figure 5-12: Square Path Comparison (70 ipm, 0.5g)

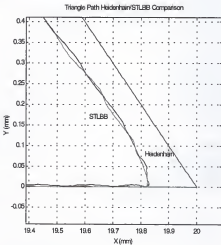


Figure 5-13: Triangle Path Comparison (35 ipm, 0.1g)

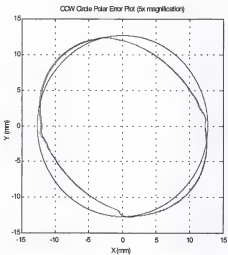


Figure 5-14: Circular Path Comparison (70 ipm)

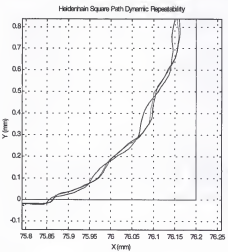


Figure 5-15: Heidenhain Dynamic Repeatability Test

Although these measurement results verify the overall dynamic performance of the STLBB system, they do not provide the micrometer-level reproduction between the two measurement sets that was expected. To investigate these small differences during motion, several consecutive tests were completed and the dynamic repeatability evaluated for the machine tool used in this study. Figure 5-15 shows three back-to-back dynamic path measurements using the Heidenhain grid plate. It can be seen that there is approximately a 20  $\mu\text{m}$  error band which contains the separate measurements. Similarly, three consecutive contours measured with the STLBB are shown in Figure 5-16. In this case, a roughly 15  $\mu\text{m}$  error band is recognized. Therefore, the dynamic contouring non-repeatability (during motion) of the machine tool motions explains the small differences between the Heidenhain and STLBB tests, rather than errors in the STLBB measurement process.

To fully explore the measurement repeatability of the STLBB, a capacitance probe was employed to compare to the STLBB static positioning repeatability. The capacitance probe setup is shown in Figure 5-17. For this set of tests, the machine tool controller was programmed to move 0.25" in the +Y direction, pause and then return to the initial position. Twenty-five repetitions were completed using both the capacitance probe and STLBB setups and the starting and ending positions compared. At a feed of 35 ipm, a maximum difference between return positions of 0.9  $\mu\text{m}$  was found for the capacitance probe and a maximum difference of 1.3  $\mu\text{m}$  for the STLBB. At 70 ipm, the maximum difference was 1.1  $\mu\text{m}$  for the capacitance probe, while the STLBB maximum difference was 0.8  $\mu\text{m}$ . These similar results suggest good measurement repeatability for the STLBB measurement system.

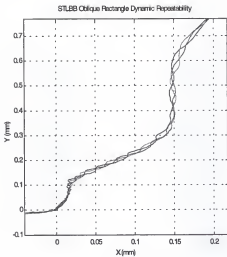


Figure 5-16: STLBB Dynamic Repeatability Test

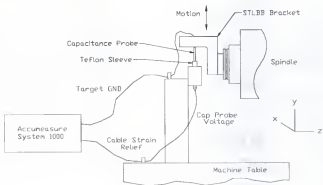


Figure 5-17: Capacitance Probe Setup

## 2-D Contouring Accuracy

An additional benefit of the Heidenhain/STLBB 2-D verification data was the information it contained regarding the contouring accuracy of the machine tool. By appropriate contour selections, the same information used for the STLBB verification was able to be utilized to evaluate the dynamic performance of the 3-axis, horizontal spindle White-Sundstrand Series 20 Omnimill used in these tests. Additionally, the effect of both feed rate and acceleration were explored to evaluate the corresponding effects. The results from the STLBB tests will now be given and the individual error sources identified for deviations of the measured from the commanded paths. It should be noted that: 1) the controller function which blends the commands of consecutive moves to smooth the path was disabled for these tests, 2) the axes were preloaded in the +X, +Y direction prior to execution of the CNC program for all tests except the clockwise circular paths (-X, +Y preload), 3) all software compensation was turned off for these tests, and 4) a nominal sampling frequency of 1kHz was selected (this provided a spatial frequency of roughly 30  $\mu\text{m}$  of translation/sample at a maximum feed of 70 ipm).

### Angle Path

An important consideration in the tuning of the servomotors on a multi-axis machine tool is the response in cornering motions (i.e., undershoot or overshoot). A simple 90° angle provides an efficient means of evaluating this response. An angle path with a commanded feed of 70 ipm and 0.1g acceleration was executed. The commanded and measured contours for the cornering section of the path are shown in Figure 5-18.

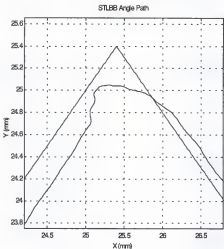


Figure 5-18: STLBB Angle Path (70 ipm, 0.1g)

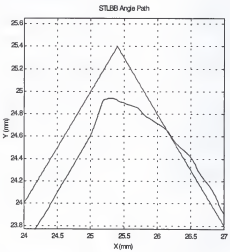


Figure 5-19: STLBB Angle Path (70 ipm, 0.5g)

In Figure 5-18 there is a differential velocity lag between the X and Y axes, which causes the actual contour to lag behind the commanded positions with some overall path error. The velocity lag ( $e_{ss}$ ) in each axis is a steady state positional error which is proportional to the feed rate and inversely proportional to the single axis gain (see Equation 5-1 [37]). As the axes are moving simultaneously in +X and +Y (at an angle of 45° to each), the Y axis lags more than the X in the measured contour. Therefore, the effective axis gains are unequal and the X gain is larger than the Y [37]. It can also be seen that there is no appreciable overshoot in the corner, although it is masked by the velocity lag. In Figure 5-19, the acceleration has been increased to 0.5g. The amount of undershoot is now slightly increased due to the more rapid deceleration into the corner and acceleration out of the corner.

$$e_{ss} = \frac{F(2\xi)}{\omega_n} = \frac{F}{K} \text{ (mm)}, \quad (5-1)$$

where  $F$  = feed rate (mm/s)

$\xi$  = 2<sup>nd</sup> order system damping ratio

$\omega_n$  = 2<sup>nd</sup> order system natural frequency (rad/s)

$K$  = feed forward positional loop gain (s<sup>-1</sup>)

Using Figure 5-18 and Equation 5-1, the difference in gain between the X and Y axes ( $\Delta K_{XY}$ ) can be calculated. The expression for  $\Delta K_{XY}$  is formulated in Equation 5-2. In order to solve this equation, a value for either the X or Y axis velocity lag must be known because the measurement data only provides a difference between the X and Y positional lags ( $\Delta_{XY}$ ). The X axis velocity lag ( $e_{ss,X}$ ) was found by measuring the following error during a constant velocity move in the X direction. This data was

obtained by recording the commanded and actual encoder counts using the PMAC controller software, then determining the difference between the commanded and actual position at constant velocity. At a feed rate of 20 ipm, this steady-state positional error was found to be 520  $\mu\text{m}$ . The X axis gain was then calculated according to Equation 5-3.

$$\Delta K_{XY} = K_X - K_Y = K_X - \frac{F_Y}{e_{m,Y}} = K_X - \frac{\frac{F_{com}}{\sqrt{2}}}{\frac{1}{K_X} + \Delta_{XY}} \quad (5-2)$$

$$K_X = \frac{F_X}{e_{m,X}} = \frac{20}{\frac{60}{0.520}} = 16.28 \frac{1}{\text{sec}} \quad (5-3)$$

Referring again to Figure 5-18, it is seen that the Y axis lags 410  $\mu\text{m}$  more than the X axis during the constant velocity section of the +X, +Y motion. Substitution of this steady-state error difference, the experimental value for the X axis gain and the commanded path velocity (70 ipm or 29.6333 mm/s) into Equation 5-2 yields a gain difference ( $\Delta K_{XY}$ ) of  $3.93 \text{ s}^{-1}$ . This value is positive because the X gain is greater than the Y gain (i.e., the Y lag is greater than the X lag).

#### Square Path

The undershoot and overshoot in cornering, as well as any reversal error in the X and Y drives, can be seen with this path. Reversal error is caused by friction in the leadscrew and produces a positional error, or dead zone, due to a force discontinuity when the direction of motion is reversed [37][21]. If the reversal error is assumed to be located between the drive and feedback sensor, it is outside the control loop and must be software

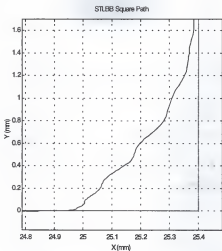


Figure 5-20: STLBB Square Path (70 ipm, 0.5g)

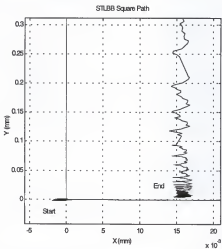


Figure 5-21: STLBB Square Path Reversal (70 ipm, 0.5g)

compensated. In Figure 5-20, the +X to +Y square cornering motion for a feed rate of 70 ipm and an acceleration of 0.5g is shown. The undershoot transient is now more apparent due to the absence of the unequal gain error seen in the two-axis angle path. The corner starts approximately 400  $\mu\text{m}$  early due to the single axis velocity lag. The X-axis reversal error can be seen in Figure 5-21. This figure shows that the end point of the square does not return to the motion start point by an offset of roughly 17  $\mu\text{m}$ . This offset shows that there is 17  $\mu\text{m}$  of lost motion when the X axis motion is reversed (at this particular place in the machine tool's work volume). The small oscillation in the X direction during the final Y motion (straightness error) is caused by the modulation of the commanded signal (linear interpolation in the Y direction) with the machine noise (with frequency components at 60, 120, and 180 Hz) in the X direction. Similarly, an X motion is modulated by the Y machine noise.

#### Sultan's Hat Contour

This path includes both linear and circular interpolation. A measurement of this path, performed at 70 ipm, is shown in Figure 5-22. The first motion is a vertical Y translation and the rest of the path is followed in a counter-clockwise direction. The X-Y gain mismatch is recognized by the contouring error (path lag) in both the circular and linear interpolation sections. At the right hand quadrant of the first circle, the X reversal error is also introduced. This manifests itself as a short vertical motion when the X axis reverses direction. This vertical translation is shown in Figure 5-23. The cornering transient can also be seen at the top of the hat in Figure 5-22.

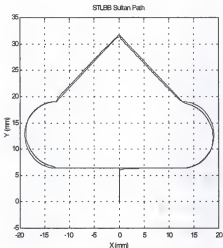


Figure 5-22: STLBB Sultan Path (70 ipm)

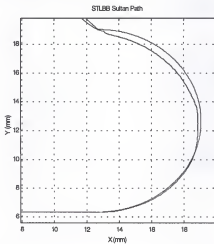


Figure 5-23: STLBB Sultan Path Reversal (70 ipm)

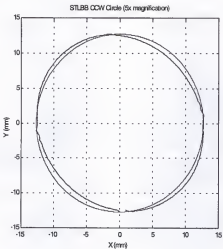


Figure 5-24: STLBB Circular Path (35 ipm)

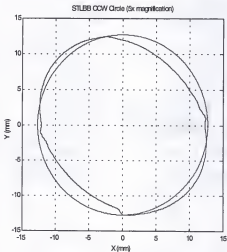


Figure 5-25: STLBB Counter-Clockwise Circular Path (70 ipm)

### Circular Contour

Perhaps the most popular path for evaluating contouring performance is a simple circle. Several circular profiles were measured at various feed rates. The results for a counter-clockwise 25.4 mm diameter circle with a commanded velocity of 35 ipm and is shown in Figure 5-24, where the radial error has been multiplied by a factor of 5. The servo gain mismatch is seen as an elliptical distortion of the measured path with the major axis oriented at an angle of 135° from the +X axis. The X axis reversal error can be seen at the 0° and 180° quadrants. In Figure 5-25, the feed has been increased to 70 ipm. The magnitude of the servo gain mismatch error is now larger and the path distortion increased.

As a final consideration in the circular measurement evaluation, the contour direction was reversed and a path measured to check for a squareness error between the X and Y axes. This error manifests itself as an elliptically-shaped error plot with the ellipse major axis tilted at either 45° or 135° depending on the sign of the squareness error (i.e., whether the angle between the X and Y axes is slightly greater or less than 90°). If the tilt is due to a squareness error, then the angular orientation of the corresponding elliptical error plot will not change when the contouring direction is reversed [38]. In Figure 5-26, the error plot is seen for a clockwise 70 ipm circular contour. This can be compared to the counter-clockwise circle in Figure 5-24 to show that there has been a mirroring of the errors about the Y axis (the major axis angle is now 45°). Therefore, the possibility of a dominant squareness error can be eliminated.

In conclusion, several 2-D paths were measured and the contouring errors evaluated. For the White-Sundstrand Omnimill machine tool used in this research, the

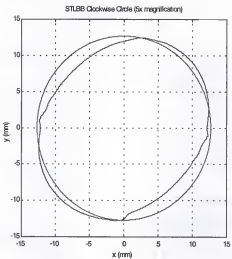


Figure 5-26: STLBB Clockwise Circular Path (70 ipm, 0.1g)

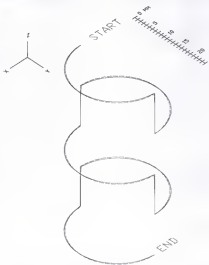


Figure 5-27: STLBB Corkscrew 3-D Path and STLBB Measurement

governing error sources were found to be an X-axis reversal error and a servo gain mismatch between the X and Y axes. This data could next be used to eliminate (by removing the error source) or compensate for (by software correction) these error sources. For example, backlash compensation, where motion pulses are injected or suppressed by the controller at axis reversals, is common to most commercial machine tool controllers.

### 3-D Measurements

Four different paths, which combine both linear and circular interpolation, were chosen to investigate the STLBB 3-D measurement performance. The first path, shown with an STLBB measurement in Figure 5-27, is corkscrew in nature. A counter-clockwise half-circle was commanded in the X-Y plane, then a small step in the -Z direction was executed. Next, the half-circle was completed and followed by another step in the -Z direction, etc. The second CNC program roughly simulated a hemispherical cutting path. First, a small circle was executed in the X-Y plane. Next, a step in both the -Z and -Y directions was commanded. A larger circle with the same center coordinates was next executed from this new starting point. The completion of this circle was followed by another Y-Z linear step, and so on. This path and a corresponding STLBB measurement is shown in Figure 5-28. The final two paths were executed in a plane oblique to each of the machine tool's coordinate axes. Both a rectangular and circular path were commanded to investigate the effect of three simultaneous coordinate motions on path errors. These oblique plane contours, along with their respective STLBB measurements, are shown in Figures 5-29 and 30.

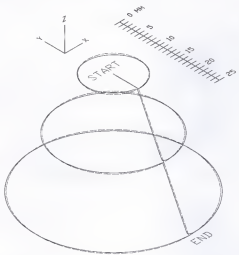


Figure 5-28: STLBB Hemisphere 3-D Path and STLBB Measurement

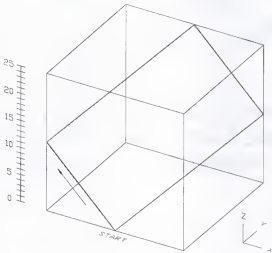


Figure 5-29: STLBB Oblique Rectangle 3-D Path

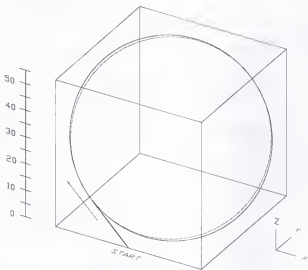


Figure 5-30: STLBB Oblique Circle 3-D Path

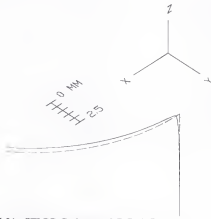


Figure 5-31: STLBB Corkscrew 3-D Path Section

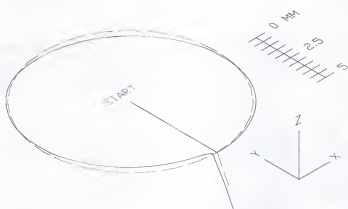


Figure 5-32: STLBB Hemisphere 3-D Path Section

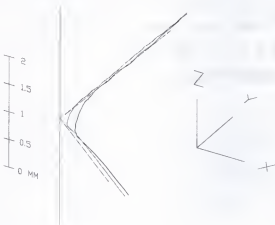


Figure 5-33: STLBB Oblique Rectangle 3-D Path Section

Comparisons between the STLBB measurements and the commanded 3-D paths are best made by viewing small sections of the individual contours. In Figure 5-31, the transition from the first half-circle to the first -Z motion in the corkscrew path is shown. The elliptical distortion of the half-circle in the X-Y plane is evident as well as undershoot in both the X and Y directions for the start of the -Z motion. The integral gain in the controller then begins to correct the steady state error (velocity lag) in the X and Y directions as the Z motion progresses.

Figure 5-32 shows the start and end point for the smallest circle in the hemispherical 3-D path. It is immediately apparent that the circular path does not close and also exhibits the elliptical distortion due to the unequal X-Y controller gains. The X-axis reversal error can also be seen as the short Y-direction straight line motion during the circular interpolation. It can also be seen that the contouring accuracy in the transition from the circular to linear interpolation is quite poor.

Figure 5-33 displays a comparison between two oblique rectangular paths executed at different feed rates (35 and 70 ipm). The section shown is the transition from -X, +Z linear interpolation to +X, +Y, +Z linear interpolation. The figure shows a steady state error in the X-Z plane and undershoot errors at the interpolation direction transition. The individual X-Y, Y-Z and X-Z planes of motion for the 3-D path section shown in Figure 5-33 are given in Figures 5-34 through 36. These plane views emphasize both the existence of errors in each of the coordinate directions for this path as well as the dramatic effect of feed rate on the magnitude of these contouring errors.

In Figure 5-34, the motion direction is first in the -X direction (to the left), then in the +X, +Y directions. The off-path velocity lag indicates that the controller gain for the

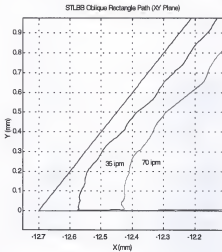


Figure 5-34: STLBB Oblique Rectangle X-Y Plane

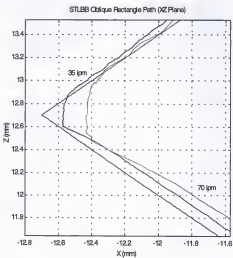


Figure 5-35: STLBB Oblique Rectangle X-Z Plane

X axis is greater than that for the Y axis (i.e., the lag is greater in the Y direction). The difference between the X and Y axis gains, calculated in the preceding section "2-D Contouring Accuracy", is  $3.93 \text{ s}^{-1}$ .

In Figure 5-35, the X-Z gain relationship is found. As the motion progresses from the lower right hand edge of the figure to the upper right, the X motion lags more than the Z by  $138 \mu\text{m}$  (at a commanded feed rate of 70 ipm), so it is surmised that the Z controller gain is larger than the X. Substitution into Equation 5-4 yields a  $\Delta K_{xz}$  value of  $-5.13 \text{ s}^{-1}$ . Note that in Equation 5-4,  $\beta_{xz}$  is the angle between the X-Z plane and the commanded direction of motion.

$$\Delta K_{xz} = K_x - K_z = K_x - \frac{\frac{F}{\sqrt{2}} \cos \beta_{xz}}{\frac{F}{\sqrt{2}} \frac{\cos \beta_{xz}}{K_x} - \Delta_{xz}} \quad (5-4)$$

Figure 5-36 displays motion in the +Z direction followed by a +Y, +Z linear interpolation. In this case, the Z controller gain is greater than the Y gain because the Y lag is approximately  $700 \mu\text{m}$  larger than the Z lag (at a feed rate of 70 ipm). The difference in gain,  $\Delta K_{yz}$ , may be calculated using Equation 5-5. The calculated gain difference,  $-8.84 \text{ s}^{-1}$ , is negative because the Y gain is smaller than the Z.

$$\Delta K_{yz} = K_y - K_z = (K_y - \Delta K_{xy}) - (K_z - \Delta K_{xz}) = -8.84 \text{ s}^{-1} \quad (5-5)$$

In summary, this single 3-D measurement (with no alignment required between the machine and measurement system axes) combined with knowledge of one of the axis gain values has provided the user with information regarding the controller gain relationships between the three coordinate axes (i.e.,  $Z_{\text{gain}} > X_{\text{gain}} > Y_{\text{gain}}$ ) as well as the gain magnitudes (in this case, the low gain settings give large steady-state errors and large cornering undershoots).

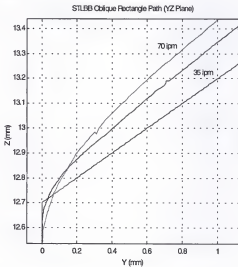


Figure 5-36: STLBB Oblique Rectangle Y-Z Plane

## CHAPTER 6 MACHINING VERIFICATION

### Introduction

As stated in Chapter 1, a sensor which could monitor the positional relationship between the tool and workpiece would serve to close the otherwise open-loop mode in which machine tools operate (i.e., the tool point coordinates are not directly known in the part's local coordinate system). Although the STLBB system can monitor the 3-D dynamic contouring accuracy and therefore close this loop, it cannot perform these measurements during the machining process (i.e., the CNC part path must be verified prior to cutting). Therefore, to fully verify the STLBB system, it was necessary to measure a given CNC contour, machine a part using the same CNC program and then compare the results.

To this end, a diamond path has been measured (on a White-Sundstrand Series 20 Ommimill) using the STLBB system at various feed rates to determine the accuracy of the dynamic contour. Next, this path was machined using the same CNC part program and feed rates on the White-Sundstrand machining center. Finally, the machined part dimensions were recorded using a coordinate measuring machine (CMM) and these dimensions compared to those obtained with the STLBB system. These results, as well as the experimental methodology, will be outlined in the remainder of this chapter. The

discussion will also include the effects of forced vibrations during stable machining on the final workpiece dimensional accuracy.

#### STLBB Results

A diamond-shaped path was measured using the STLBB system (see Figure 6-1). This contour represents the tool path (including tool offsets) for a diamond which is nominally 18.1554 mm across the two faces. The path was executed and measured at two different feed rates (20 and 35 ipm) and a single (constant) acceleration of 0.1g to be compared with machining results. The measured paths exhibit the same contouring errors identified in Chapter 5 (i.e., X-Y gain mismatch and X reversal error). By highlighting small sections of the diamond path, these errors become obvious. In Figure 6-2, the X reversal error is shown. As the path direction switches from +X to -X motion, there exists a dead zone during which no X movement takes place. Because the Y axis is in motion during this time and the two dual-axis linear interpolations lie at  $\pm 45^\circ$  in the X-Y plane, the X reversal presents itself as a short vertical translation of length equal to the magnitude of the X reversal error (17  $\mu\text{m}$ ). A small Y reversal error (approximately 6  $\mu\text{m}$ ) can also be seen in Figure 6-3, which displays the start and end points of the diamond path. Also seen in this figure is the machine noise at the path start/end points (approximately 3.5  $\mu\text{m}$  in Y and 2  $\mu\text{m}$  in X).<sup>1</sup>

---

<sup>1</sup> The usefulness of the STLBB system as a diagnostic device for contouring performance is again emphasized by these measurements. Before cutting a test part, poor dimensional accuracy of the final machined workpiece could be predicted.

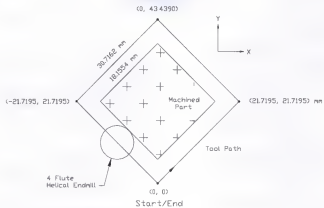


Figure 6-1: Diamond Tool Path

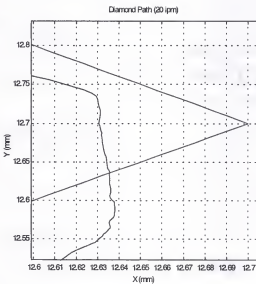


Figure 6-2: X Reversal Error

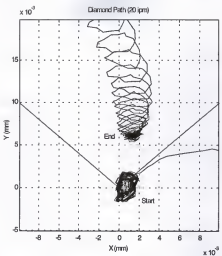


Figure 6-3: Y Reversal Error

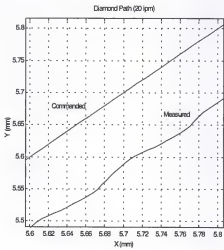


Figure 6-4: X-Y Gain Mismatch Error

The X-Y gain mismatch is seen as the steady-state contouring error shown in Figure 6-4 for a +X, +Y motion at 20 ipm. In the figure, it is seen that the Y motion lags more than the X, so a large contouring error is introduced. The total effect of the gain mismatch on the diamond path is to lengthen the distance across one face ( $d_1$  in Figure 6-5) by twice the servo gain mismatch error and shorten the distance across the other ( $d_2$  in Figure 6-5), again by twice the gain mismatch error. The magnitude of this velocity-dependent error is quite large, even for the relatively slow 20 and 35 ipm feed rates used for the machining verification.

By importing the measurements into AutoCAD® (version 14.0) via a script file, the distances ( $d_1$  and  $d_2$ ) were measured at 9 different locations for each recorded path. Figure 6-6 shows an example of the  $d_1$  and  $d_2$  experimental values for a 35 ipm STLBB test. In Figure 6-6 it can be seen that the previously discussed controller errors exert a sizable influence on the path straightness (i.e., large variation in  $d$  values) as the integral gain attempts to correct the steady-state error. The final values for  $d_1$  and  $d_2$  were obtained by averaging the 9 measurements across each face. The value for  $\Delta d$  was then calculated by subtracting the average  $d_2$  value from the average  $d_1$  value. This method was chosen because it most closely corresponds to the CMM probing method used to measure the machined parts (i.e., 13 points were probed and a line best fit to the data in the CMM software). STLBB results for the two different feed rates are listed in Table 6-1. Also listed is the commanded value and the difference ( $\Delta d$ ) between  $d_1$  and  $d_2$ . It should be noted that these values reflect measurements of the actual tool path followed by the cutter. The final part dimensions, therefore, will be a function of the cutter diameter.

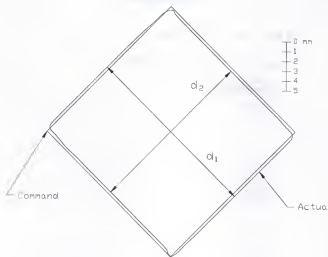


Figure 6-5: Diamond Path Gain Mismatch Effect (70 ipm)

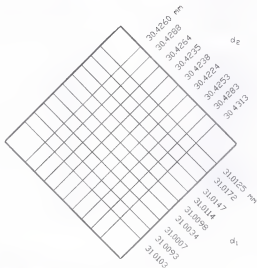


Figure 6-6: Determination of  $\Delta d$  (35 ipm Test)

However, the difference ( $\Delta d$ ) is unaffected by the actual cutter diameter and will be used for the STLBB verification.

Table 6-1: STLBB Diamond Path Results

Feed Rate	Commanded, $d_1$	Measured, $d_1$	Measured, $d_2$	Difference, $\Delta d$
20 ipm	30.7162 mm	30.8891	30.5453	0.3438 mm
35	30.7162	31.0099	30.4262	0.5837

#### Experimental Method

The machining verification was performed at the same two linear feed rates as the STLBB measurements, as well as the same commanded acceleration. The first test was executed under the following up-milling cutting conditions: 20 inches per minute linear feed, 0.0037" feed per tooth, 1337 rpm spindle speed, 1% radial immersion, and an axial depth of cut of 0.010". The low radial immersion was chosen to simulate a finishing operation and the low axial depth of cut avoided chatter while minimizing the (axial) surface location error due to the helical geometry of the cutter (see Appendix C for a description of this error type). The second test was performed at 35 ipm and a spindle speed of 2339 rpm. All other cutting conditions were identical. The machining tests were performed at the same coordinates within the machine tool's work volume as the STLBB tests (to reduce the effect of the inherent positional-dependent geometric inaccuracies) and the same approximate thermal state (the parts were machined from a cold thermal state). The same axis preloads (+X, +Y) were also observed to minimize reversal errors.

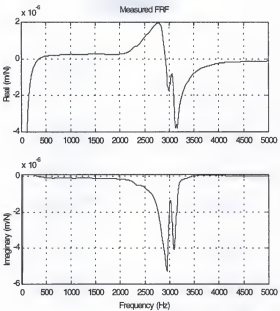


Figure 6-7: Frequency Response Function (FRF) for 0.5" Diameter Endmill

The cutting tool used for both tests was a nominal 0.5" diameter, 4-flute, high speed steel (HSS) helical end mill with a 1.5" overhang. The transfer function for the tool in the Y coordinate direction is shown in Figure 6-7 (the X results are similar). A curve fit to this data yields modal values of: 0.01 kg mass, 3.5e6 N/m stiffness, and a damping ratio of 0.03 for the most flexible mode at a natural frequency of 2950 Hz.

Once the diamond test parts were machined, they were allowed to soak overnight in a temperature-controlled environment ( $68 \pm 0.2^\circ\text{F}$ ) and then measured on a Brown & Sharpe MicroVal PFx coordinate measuring machine. These measurements were completed under "Direct Computer Control" or DCC to improve the measurement accuracy. In this method, the part is first probed manually by the user (13 points were probed on each face of the diamond parts). The computer records the location in the CMM work volume of the measured features (four 2-D lines in this case) and then calculates the surface normal to each probed point. A corresponding part program is automatically written which includes the user-defined measurements and the appropriate approach directions. When this part program is executed and the features are probed under computer control, the measurement accuracy (roughly  $\pm 1 \mu\text{m}$  for the portion of the work volume used in these measurements) is maximized due to the normalized approach directions and constant (computer-controlled) approach speed. The measurement results for two machining verification parts are given in Table 6-2.

Table 6-2: Machining Verification Results

Feed Rate	Commanded, d	Measured, d <sub>1</sub>	Measured, d <sub>2</sub>	Difference, Δd
20 ipm	18.1554 mm	18.3056	17.9712	0.3344 mm
35	18.1554	18.4278	17.8439	0.5839

Comparing these results with the STLBB dynamic contour measurements provides the final verification for the STLBB system. At 35 ipm, the difference between the face dimensions of the diamond path,  $\Delta d$ , was measured as 0.5837 mm using the STLBB. The difference between the face dimensions for a machined part was then measured as 0.5839 mm using the CMM. These measurements agree to within 0.2  $\mu\text{m}$  (0.03% error). The 20 ipm tests provided a larger discrepancy of 9.4  $\mu\text{m}$  (2.7% error). Table 6-3 shows a comparison of the machining and STLBB tests in tabular form.

Table 6-3: STLBB vs. Machining Verification Results

Feed Rate	$\Delta d$ , STLBB	$\Delta d$ , Machining	Error
20 ipm	0.3438 mm	0.3344	9.4 $\mu\text{m}$ (2.7%)
35	0.5837	0.5839	0.2 $\mu\text{m}$ (0.03%)

In an attempt to define the small measurement differences, several consecutive STLBB measurements and machining tests were completed to attempt to determine the repeatability of  $\Delta d$ , the metric used to evaluate the STLBB performance in these tests. At 35 ipm, the maximum difference between calculated  $\Delta d$  values for successive STLBB measurements was 3.5  $\mu\text{m}$ . The maximum difference for  $\Delta d$  between sequential machined part measurements, again at a feed rate of 35 ipm, was 5.2  $\mu\text{m}$ . These repeatability errors are of the same order as the differences seen between the STLBB and machined part measurements. This close agreement between the STLBB and machined part measurements further validates the STLBB system as a pre-process tool for CNC part program validation.

It should be noted that the diamond path used in this research represents a special case. Because the path is symmetric about both the X and Y axes, common path variations (such as surface location errors due to cutter deflections during machining, axis of rotation errors for the cutter and/or spindle or quasi-static spindle thermal growth errors) will not affect the metric ( $\Delta d$ ) used to verify the STLBB system. Axis of rotation errors for the cutter teeth (commonly called run-out), for example, will affect both dimensions ( $d_1$  and  $d_2$ ) by the same amount and, therefore, have no effect on  $\Delta d$ . Additionally, the path was kept small to minimize the introduction of the machine tool's parametric errors into the machined part geometry. In fact, this path was expressly chosen for the combination of the large X-Y gain mismatch errors and the absence of these other error sources.

In general, these special considerations cannot be met and the surface location and axis of rotation errors, as well as the machine tool's inherent parametric and thermal errors, can have a significant effect on the final dimensions of a machined part. For instance, if an improper tool offset (tool diameter) is used in the CAD/CAM generation of complicated CNC part paths, significant part errors can be obtained as the cutter follows both inside and outside contours. Perhaps more insidious is the effect of forced vibrations during stable machining on the final part dimensions. Depending on the selected spindle speed, cutter dynamics and chip load, different part dimensions may be obtained by relatively small variations of these parameters. These differences between the commanded and actual part dimensions due to cutting force effects have been termed surface location errors [37]. To the uninformed observer, these surface location errors could be attributed

to other common error sources (e.g., parametric, thermal, programming) and a large amount of time wasted in attempting to diagnose and fix the problem.

Because surface location errors represent the only (theoretical) difference between the STLBB dynamic 3-D path measurements and machined part dimensions, this phenomenon has been explored experimentally. Additionally, the theory behind surface location errors and their prediction, as well as a computer simulation and machining verification, are presented. The experimental results show that a simple variation in spindle speed can change the surface location error from undercut (less material removed than commanded) to overcut (more material removed), depending on the relationship between the rotational frequency of the spindle (and subsequent harmonics) and the natural frequencies which correspond to the most flexible modes of the tool/machine/workpiece system. However, due to the length of the experimental methodology description and discussion of the results, this material has been included in an appendix. The interested reader is referred to Appendix C for a more complete description of surface location errors and their determination.

## CHAPTER 7 CONCLUSIONS

### Completed Work

In this research the implementation of simultaneous trilateration to measure three-dimensional CNC using the Laser Ball Bar was completed. A prototype Simultaneous Trilateration Laser Ball Bar (STLBB) system was designed, constructed, and tested. The design and construction of the STLBB system included a redesign of the past generation LBB. This redesign was comprised of a dramatic size increase, a change in the optical configuration of the Michelson interferometer used to sense the LBB length and a new four degree-of-freedom positioning system for the interferometer optics within the LBB housing. Also included was the novel design of a tool socket joint (and spring aid) used to support the three LBBs during simultaneous trilateration.

The initial verification testing of the STLBB system was composed of two main parts. In the first set of tests, a group of six two-dimensional contours were measured with both the STLBB system and a Hiedenhain KGM 101 Grid Encoder. Both path velocity and acceleration were varied to study the corresponding effects. Good agreement between the STLBB and Heidenhain results at all velocities and accelerations provided authentication of the STLBB measurement capabilities. Additionally, the STLBB results were utilized to assess the 2-D contouring accuracy of the 3-axis machining center used in this study. These results showed that this particular CNC machine had a sizable X

reversal error (at the particular place in the work volume where the tests were carried out) and a considerable mismatch between the X and Y axis gains.

The second group of initial verification tests included an evaluation of the static and dynamic measurement repeatability of the STLBB system. The static positioning repeatability was tested by comparing the STLBB measurement results for a short single axis translation (i.e., a motion of 0.25" in +Y followed by a return to the start position) to capacitance probe measurements of the same path. Sub-micrometer agreement between the return positioning error recorded by the two methods was found.

The dynamic positioning repeatability was evaluated using the Heidenhain Grid Encoder. In these tests, several back-to-back CNC paths were executed and the results recorded using both the STLBB and Heidenhain measurement systems. For this particular machining center, it was found that the dynamic positioning non-repeatability of the machine tool was much larger than the measurement systems' resolution. Using both systems, approximately a 15  $\mu\text{m}$  error band was needed to enclose successive repetitions of an example NC path during dynamic motions, although the starting and ending points of the path were repeatable to sub-micrometer levels.

Once the validity and repeatability of the STLBB system as a dynamic measurement tool were exhibited, the next step was to perform the inaugural measurement of three-dimensional CNC contours to micrometer-level accuracy. Four contours were selected to highlight the STLBB system's 3-D measurement capabilities: a corkscrew, a hemisphere, an oblique-plane rectangle and an oblique-plane circle. These paths combined linear and circular interpolation in three simultaneous axes of motion. The measurement results showed a large dependence of the path contouring accuracy on the commanded

feed rate, as well as overall poor contouring performance for the 3-axis machine tool used in this study. The oblique rectangular path was used to establish the gain mismatch between all three axes with a single measurement and no alignment of the STLBB system with the machine tool coordinate directions. Also recognized in this path were reversal errors in both the X and Y axes.

The final group of verification tests included machining and measuring aluminum test parts to compare with STLBB contour measurements. A diamond path was chosen for this endeavor. This path provided relatively large errors (due to the large X-Y gain mismatch on the machine used in this study) while minimizing other possible error sources such as axis or rotation errors of the cutter/spindle and surface location errors due to forced vibrations during machining. A comparison between STLBB measurements and machined part dimensions showed differences between 0.2 and 9.4  $\mu\text{m}$  (0.03 and 2.7% error) with path repeatability in both cases of roughly 5  $\mu\text{m}$ . Because the experimental differences are on the order of the path repeatability, these measurements serve to further validate the STLBB system's performance.

An evaluation of the extensive verification procedures performed in this research leads to the following conclusions. First, the STLBB system is fully capable of the dynamic measurement of spatial coordinates along arbitrary 3-D contours. Second, the absolute dynamic accuracy of the system is difficult to quantify because the contours measured in this research did not possess good dynamic repeatability. However, the static positioning measurement accuracy of the system was shown to agree with capacitance probe measurements to  $\pm 0.4 \mu\text{m}$ . Finally, in terms of system bandwidth, the expected limitations would be imposed by the mechanical rather than the optical portion of the

overall design. Conservative values for the maximum allowable feed rate and acceleration for arbitrary contours are 100 ipm and 1.0g, respectively.

Also provided as part of this research was an in-depth analysis of surface location error theory. It was shown that the relationship between the spindle speed (and harmonics) and the cutter/machine/workpiece dynamics is of prime importance. By changing the spindle speed, variations in the surface location error from undercut to overcut was demonstrated. Also included was a simple computer simulation which attempted to predict the surface location error based on the cutter dynamics and machining conditions.

#### Future Work

This work provides a complete verification of simultaneous trilateration (using three Laser Ball Bars) as a method to measure three-dimensional CNC contours. As with most complicated opto-mechanical designs, some design improvements could be suggested after using the system for several batteries of tests. In terms of the optics package, although the implemented design is optically efficient and sufficiently rugged, initial internal alignment and assembly of the optics (within the optics package) is challenging and time-consuming. In this first generation design, the flatness of a machined surface and small adjustment screws were relied upon to align the interferometer optics with the multi-mode fiber optics which carry the local reference and measurement signals from the LBBs to the measurement electronics. A flexure-type alignment mechanism with two independent angular degrees-of-freedom would greatly simplify this initial optical alignment. However, once this alignment was complete, the 4-DOF positioning device

(which aligns the optics package with the moving retroreflector at the end of the LBB) performed admirably. No axial translation during measurement was identified and the interferometer alignment was deemed intuitive and relatively easy to perform.

A final improvement on the optical package would be to replace the SMA-type (multi-mode) fiber optic connectors with ST-type connectors. The SMA connectors have an internally-threaded sleeve and male ferrule which mate with an externally-threaded female housing. Although repeatable and optically efficient when assembled, it was observed that the threaded connector tended to loosen after several cable flexures during a typical set of dynamic measurements. This severely degrades the optical power received by the measurement electronics and can disrupt the measurements. The ST connector has a spring-loaded bayonet mechanism which locks into place and would not suffer from this gradual loosening.

The main suggestion for the overall LBB mechanical design is to dramatically decrease the weight. If the total weight could be approximately halved, the problems encountered with insufficient magnetic attractive force between the LBB sockets and tool sphere could possibly be overcome. If these problems were resolved, the spring-aid device at the tool sphere (which provides the additional attractive force between the individual LBBs and the tool socket) could be eliminated and the work volume of the STLBB greatly increased. In fact, with the current design the increase in work volume obtained by enlarging the LBB lengths (to approximately 1 m fully extended) was essentially canceled by the angular limitations imposed by the spring-aid device.

Aside from these (minor) design changes, future work for the STLBB system should include other applications of its 3-D measurement capabilities. Initial suggestions

include inverting the STLBB assembly in a portable housing to provide 3-D contour measurements of highly accurate optics (e.g., large lenses) during the polishing process. Another possible use is the measurement and evaluation of the velocity and acceleration profiles for arbitrary 3-D motions. This is easily accomplished by adding a time stamp to the position data and then performing numerical differentiation to accurately obtain the velocity and acceleration.

Machine tool applications include the quick and efficient evaluation of a machine tool's contouring accuracy. Geometric and controller effects could be isolated by adopting a measurement algorithm which includes static and dynamic measurement of paths which contain both linear and circular interpolation in three-axes at various feed rates. The incorporation of the surface location errors during (chatter-free) machining with the previous measurement results could serve to close the otherwise open-loop machining process. This would allow the machine tool user to finally bridge the gap between a programmed CNC part path and the final dimensions of the machined workpiece.

## APPENDIX A PROCESS CAPABILITY

Process capability is a controversial new subject within the field of modern manufacturing. Inconsistencies in terminology and the evaluation of the process capability indices (PCIs) has led to much confusion among users. Kotz and Johnson suggest the primary problem is with the application of these indices as deterministic rather than random. In this way, process capability can be differentiated from precision engineering. Process capability seeks to define an operation by describing the (assumed) random variations in terms of statistical theory. Precision engineering, on the whole, attempts to assign deterministic solutions to process variations.

Since process capability is firmly rooted in statistical theory, a primary consideration is the repeatability of a process. For an unstable process, a capability prediction is impossible because the probable future outputs are unknown. Good statistical control is therefore a pre-requisite to estimating the process capability. Stable processes are said to contain only common-cause variations (e.g., machine, operator, material, measurement system). These are components which originate from the main elements of the manufacturing process. The influence of common-cause variations on the final output may be estimated. Unstable processes, on the other hand, contain events which change the output variation by an unknown amount (assignable-source variations). Typical assignable-source variations include a broken tool, fixturing errors or spikes in the supply air pressure [1].

Once a process has been statistically stabilized and the output(s) measured over a reasonably long period, the next step is to attempt to describe the process capability using one or more process capability indices. Process capability indices are a tool for "judging potentials and capabilities of a manufacturing process" already under statistical control [2]. Two commonly used PCIs are  $C_p$  and  $C_{pk}$ , although many others are available.

$C_p$  is used to estimate the amount of expected process variation. For a value of unity ( $C_p = 1$ ) and a normal distribution of the variation, this index indicates that the expected proportion of non-conforming parts is *not less than* 0.27%.  $C_p$  may be calculated according to Equation A-1 [2].

$$C_p = \frac{USL - LSL}{6\sigma} \quad \text{where } USL = \text{upper specification limit} \quad (\text{A-1})$$

LSL = lower specification limit  
 $\sigma$  = standard deviation of measured value

$C_{pk}$  considers both the process variation and the centering of the variation about some nominal value [1]. This index, therefore, is influenced by the process mean,  $\xi$ .  $C_{pk}$ , which does not require knowledge of  $\xi$ , may not provide a direct relation between its value and the probability of producing a non-conforming part [2] (see Equation A-2).

$$C_{pk} = \frac{\min(USL - \xi, \xi - LSL)}{3\sigma} \quad (\text{A-2})$$

APPENDIX B  
TRANSFORMATION OF BALL BAR COORDINATES INTO MACHINE  
COORDINATES [7]

A method to transform coordinates from the LBB frame {B} into a given machine frame {M} is outlined here. The first step is to define a reference axis in the machine frame. In this approach, the reference axis is assumed to be the  $Z_M$  axis. The LBB is used to sequentially sample a set of points  $(x_i, y_i, z_i)$  at regular intervals along the positive  $Z_M$  axis. These coordinates are used to best fit a line along this axis. The direction cosines of the best fit line provide the components of the unit vector  $\underline{n}_z$  in the LBB coordinates along the  $Z_M$  axis. Similarly, a set of points are sampled by moving along the  $X_M$  axis. Since the machine axes could have orthogonality (or squareness) errors between them, the direction cosines of the vector  $V_x$  derived from the  $X_M$  motion need not represent a unit vector orthogonal to the  $Z_M$  axis. However, a unit vector  $\underline{n}_y$  can be defined by Equation A-1 which will lie in the  $Y_M$  direction.

$$\underline{n}_y = \frac{\underline{n}_z \times \underline{V}_x}{|\underline{n}_z \times \underline{V}_x|} \quad (\text{A-1})$$

By evaluating  $\underline{n}_y \times \underline{n}_z$ , the unit vector  $\underline{n}_x$  along the  $X_M$  axis is found. These unit vectors  $\underline{n}_x$ ,  $\underline{n}_y$ , and  $\underline{n}_z$  form a right-handed Cartesian coordinate system and represent the coordinate system of the machine as seen in LBB coordinates. The 3x3 rotation matrix

between the ball bar frame and the machine tool frame can be expressed as shown in Equation A-2.

$$R_B^M = \begin{bmatrix} n_x \\ n_y \\ n_z \end{bmatrix} \quad (A-2)$$

The transformation between the two coordinate frames can then be expressed by the 4x4 matrix shown in Equation A-3. The final column,  $\underline{D}$ , in the transformation matrix defines the translation between the origins of the two coordinate frames. However, the  $\underline{D}$  vector is set to zero in this method since all the machine errors are normalized with respect to the origin of the machine frame {M}.

$$T_B^M = \begin{bmatrix} R_B^M & \underline{D} \\ 0 & 0 & 0 & 1 \end{bmatrix} \quad \text{where } \underline{D} = [D_x \ D_y \ D_z]^T = [0 \ 0 \ 0]^T \quad (A-3)$$

## APPENDIX C SURFACE LOCATION ERROR IN MACHINING

### Forced Vibrations and Surface Location Error

The relationship between the spindle speed, the most flexible natural frequencies of the machine/cutting tool system and the final part dimensions is not a simple one. It has been detailed by Tlusty in [37], Smith [41], and Altintas [49] and will be briefly outlined here. As shown in Figure C-1, cutter deflections during end milling will only affect the final surface when a tooth is in position 1.

In up milling (Figure C-1a), the error of location is defined as the displacement of the cutter relative to the commanded depth of cut when a tooth enters the cut. In down milling, the error is defined as the cutter displacement relative to the desired surface when a tooth disengages from the cut [40]. At other angular orientations of the tool, any imprint of the cutter deflection on the material will be removed by succeeding teeth.

As the cutter impacts the workpiece surface, a situation of forced vibration arises in which the dominant forcing frequency is equal to the tooth passing frequency of the cutter,  $f_{tooth}$  (see Equation C-1). For simple systems under forced vibration, the deflection varies at the same frequency as the force, but lags it in time. The cutting forces are strongly harmonic and cause deflections of the cutter. The amplitude and phase of these deflections depends not only on the system flexibility and cutting conditions, but also on the system natural frequency (i.e., when the forcing frequency is equal to the natural

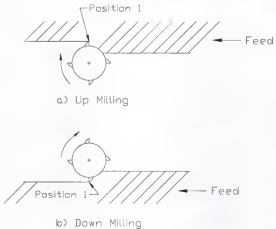


Figure C-1: Up/Down Milling

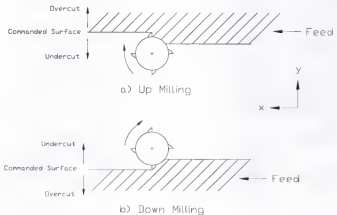


Figure C-2: Undercut/Overshoot in Milling

frequency, resonance is observed and large deflections can occur). The crucial factors, therefore, are the spindle speed (proportional to the tooth passing frequency) and the frequency response of the system. As the tooth passing frequency is varied, the magnitude and phase of the cutter vibration change. This, in turn, varies the final surface location.

$$f_{\text{tooth}} = nm \text{ (Hz)}, \quad \begin{aligned} \text{where } n &= \text{spindle speed in rev/s} \\ m &= \text{number of teeth on cutting tool} \end{aligned} \quad (\text{C-1})$$

It is the occurrence of resonance and the importance of the ratio,  $r$ , of the forcing frequency to the natural frequency ( $r = f_{\text{tooth}}/f_a$ ) that makes this work especially relevant to the field of high-speed machining (HSM). One popular definition of HSM is operation at spindle speeds where the tooth passing frequency is equal to an integer fraction of the system's most flexible natural frequency. Machining at these speeds can dramatically increase the allowable depth of cut for stable machining. By increasing the stable depth of cut, the material removal rate (MRR) can be increased and the machining time substantially reduced [42]. However, operating at these spindle speeds may also adversely affect the workpiece accuracy depending on the tool flexibility.

$$\text{MRR} = b * a * f \text{ (mm}^3/\text{min}), \quad \begin{aligned} \text{where } b &= \text{axial depth of cut (mm)} \\ a &= \text{radial depth of cut (mm)} \\ f &= \text{linear feed rate (mm/min)} \end{aligned} \quad (\text{C-2})$$

Over a range of spindle speeds that span an integer increase in the number of waves of vibration per tooth (e.g.,  $f_{\text{tooth}} = f_a$  to  $2f_{\text{tooth}} = f_a$ ), a periodic change in the surface location will occur. This change in surface location is termed overcut when the part is

smaller than commanded (i.e., more material removed than specified) and undercut when larger than commanded (see Figure C-2). This periodic variation between overcut and undercut will now be described.

Consider the case of down milling with a circular tool path assumed. The normal and tangential cutting force components shown in Figure C-3 may be projected into the x and y coordinate directions using the cutting angle ( $\phi$ ) according to Equation C-3. The tangential cutting force,  $F_T$ , is taken to be proportional to the material specific force ( $K_s$ ), the feed per tooth ( $f_t$ ), the chip width ( $b$ ), and the cutting angle. The normal (or radial) force ( $F_N$ ) is assumed proportional to the tangential force (see Equation C-4).

$$F_x = \sum_{i=1}^m F_{T,i} \cos \phi_i + F_{N,i} \sin \phi_i, \text{ where } m = \# \text{ teeth in cut at cutter angle } \phi \quad (\text{C-3})$$

$$F_y = \sum_{i=1}^m F_{T,i} \sin \phi_i - F_{N,i} \cos \phi_i$$

$$F_T = K_s b f_t \sin \phi \quad (\text{C-4})$$

$$F_N = F_T \cos \beta, \text{ where } \beta = 72^\circ \text{ and } \cos \beta = 0.3$$

Substitution of Equation C-4 into Equation C-3 yields x and y cutting forces, each with three distinct terms: DC, sine, and cosine [37] (see Equation C-5).

$$F_x = K_s b f_t \sum_{i=1}^m \sin \phi_i \cos \phi_i + 0.3 \sin^2 \phi_i = \frac{K_s b f_t}{2} \sum_{i=1}^m \sin 2\phi_i + 0.3 - 0.3 \cos 2\phi_i \quad (\text{C-5})$$

$$F_y = K_s b f_t \sum_{i=1}^m \sin^2 \phi_i - 0.3 \sin \phi_i \cos \phi_i = \frac{K_s b f_t}{2} \sum_{i=1}^m 1 - \cos 2\phi_i - 0.3 \sin 2\phi_i$$

For small radial immersions, only a single tooth is in the cut at any given instant. Therefore, the cutting force is approximately constant during engagement and zero otherwise. This force is similar to an impulse with a short duration and gives strongly harmonic frequency content [40]. The frequency spectrum of the cutting force therefore includes both the fundamental tooth passing frequency, ( $f_{tooth} = f_a$ ), and harmonics which occur at integer multiples of the fundamental frequency.

For now, consider only the fundamental frequency and its effect on the surface location error. The three term, y-force component given in Equation C-5 may be evaluated and used to find the y-deflection of the cutter (which is imprinted on the final surface at cutting angles which are odd multiples of  $180^\circ$  or  $\pi$  rad for each tooth on the cutter). The y-direction cutter displacement is phase shifted behind the y-force by an angle which is dependent on the ratio,  $r$ . Three distinct down milling cases will now be explored to explain the variation of overcut to undercut.

Case 1:  $r < 1$  ( $f_{tooth} < f_a$ )

The three components of the y-force from Equation C-5, as well as the sum of the three components, are plotted in Figure C-4. The y-displacement which results from the two periodic (cosine and sine) force components may be found using the system transfer function ( $y_i = Y/F * F_i$ ,  $i = 1, 2$ ). The DC deflection is equal to the DC force divided by the static system stiffness,  $k$ . The linear magnitude and phase plots for an example single degree of freedom system are shown in Figure C-5. The magnitude and phase for a given ratio  $r$  may be calculated according to Equation C-6.

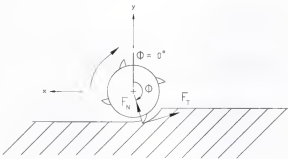


Figure C-3: Cutting Forces in Down Milling

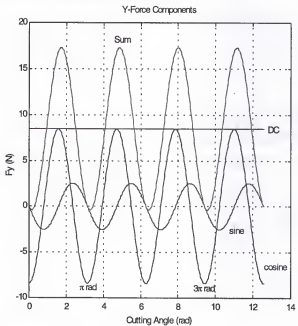


Figure C-4: Y-Force Components ( $r < 1$ )

$$\frac{Y}{F} = \frac{1}{k} \frac{1}{\left( (1 - r^2)^2 + (2\xi r)^2 \right)^{\frac{1}{2}}}, \text{ where } \xi = \text{damping ratio, } k = \text{stiffness} \quad (\text{C-6})$$

$$\gamma = -\tan^{-1}\left(\frac{2\xi r}{1 - r^2}\right)$$

It can be seen for the lightly damped system shown in Figure C-5 that for  $r < 1$ , the phase rapidly approaches  $0^\circ$  and the magnitude approaches the DC value ( $1/k$ ). The two periodic components of the  $y$ -force are shown in rotating vector form in Figure C-6 at some instant when a tooth is in position 1 (from Figure C-1). The respective deflections, which lag the force by the phase angle ( $\gamma$ ) are also shown. The cutter displacement component which results from each force term is found by projecting the phase shifted deflections onto the real axis. For the small phase lag corresponding to  $r < 1$ , the deflection due to the periodic components is dominated by the negative deflection caused by the larger cosine force component,  $y_1$ .

The three components of the  $y$ -displacement due to the three force components of Equation C-5, as well as the sum of the three components, are shown in Figure C-7, now in a time-based format and scaled using Equation C-6. The cutter angles which produce the final surface location (odd multiples of  $\pi$  rad) are marked. As seen in the figure, the sum of the three deflection components is negative at the cutter locations which produce the final surface.

The final deflection may also be found by adding the real projection of the two deflection components shown in Figure C-6 to the DC deflection ( $K_3 b f / 2k$ ). The addition of the small positive DC deflection to the large negative resultant deflection

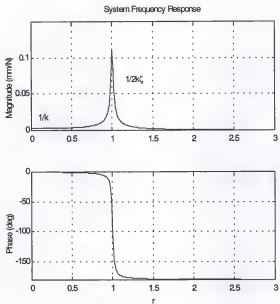
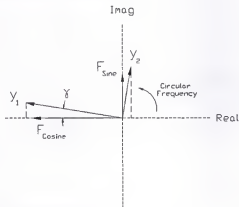


Figure C-5: System Frequency Response

Figure C-6: Phasor Diagram ( $r < 1$ )

from the periodic force components produces an overcut surface since the total cutter deflection is negative (into the cut for a down milling operation).

**Case 2:  $r = 1$  ( $f_{\text{sooth}} = f_s$ )**

As seen in Figure C-5, there is a  $90^\circ$  phase delay between the cutting force and deflection at resonance. Due to this phase shift, the y-force may now be re-written as shown in Equation C-7. The three force components and their sum for a single tooth including this phase shift are shown in Figure C-8.

$$F_y = \frac{K_s b f_s}{2} (1 - \sin 2\phi + 0.3 \cos 2\phi) \quad (\text{C-7})$$

The corresponding deflections may again be shown in rotating vector format. In Figure C-9 it is seen that the sine force term deflection (scaled by the resonant  $1/2k\xi$  factor and shifted  $90^\circ$  behind the force) projects no component on the real axis, while the cosine force term (scaled by the same factor and again lagging by  $90^\circ$ ) adds a positive value to the final deflection. The final down milling surface is now assumed to be undercut since the positive deflection of the cosine force,  $y_2$ , is added to the always positive DC deflection.

**Case 3:  $r > 1$  ( $f_{\text{sooth}} > f_s$ )**

This situation is similar in magnitude to Case 1, but the phase now rapidly approaches  $-180^\circ$ . The phasor diagram, shown in Figure C-10, now gives a positive deflection due to the large phase shift behind the cosine and sine terms of the y-force. When combined with the DC deflection, a final undercut surface is predicted.

The preceding examples have assumed a single fundamental component at the

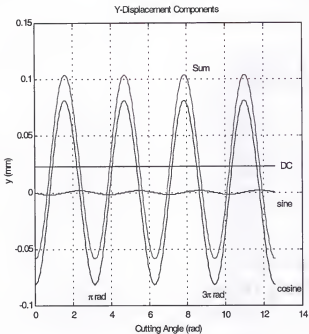


Figure C-7: Y-Displacement Components ( $r < 1$ )

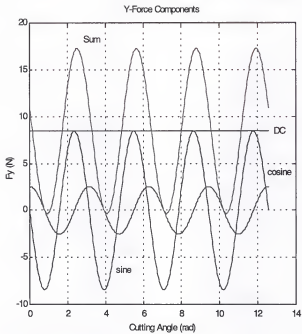


Figure C-8: Y-Force Components ( $r = 1$ )

tooth passing frequency in the force frequency spectrum. In reality, as noted previously, this spectrum contains the fundamental tooth passing frequency as well as several harmonics of significant amplitude. For example, a reduction in spindle speed from resonance ( $f_{tooth} = f_n$ ) to  $2f_{tooth} = f_n$  causes a shift of the fundamental frequency from resonance ( $r = 1$ ) to below the resonant frequency ( $r < 1$ ), so a change from undercut to overcut would be expected for a down milling operation. However, reducing the spindle speed to  $2f_{tooth} = f_n$  also shifts the first harmonic of the fundamental frequency into the resonant position (see Figure C-11). Therefore, the situation of undercut is again seen. This periodic change from undercut to overcut and back to undercut while reducing the spindle speed is repeated until all the significant (tooth passing) harmonics are well below the system natural frequency. The situation becomes even more complex if the system has multiple closely-spaced modes of approximately equal stiffness. In this case, adjacent modes will be undergoing this periodic variation from undercut to overcut simultaneously and the surface location can be predicted only by detailed simulation.

Additionally, in the previous paragraphs, only the y-direction force and deflection (perpendicular to the final surface) were considered. In reality, for small radial immersions (e.g., finishing passes), the x-direction force grows larger than the y-direction force and the x-direction vibrations can influence the location of the final machined surface.

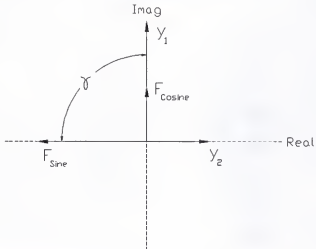
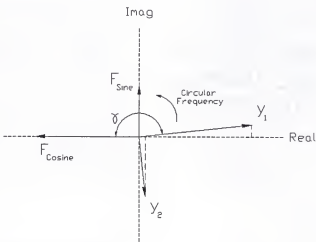
Another phenomenon associated with end milling cutter vibrations, defined as the profile error, is also dependent on the spindle speed, system natural frequency and stiffness, as well as the axial depth of cut [43]. For helical cutters, points on the cutting edge pass through position 1 at different instants in time along the length of the cutter. Therefore, the error of surface location described previously varies along the axial depth

of cut. In this research, the axial depth of cut was kept small to avoid this particular error and isolate the surface location error only.

### Simulation

Although the simple calculations outlined previously can reveal a picture of the cutter deflections, the determination of the final surface location error is best evaluated by time domain simulation. A simulation for end milling operations is described here which calculates the tangential and normal forces on the cutter, the resulting cutter deflections in both the x and y-directions and the final error of surface. The simulation also includes regeneration of surface (although it is a secondary effect in forced vibrations [37]) and the non-linearity which arises when the tool jumps out of the cut due to excessive vibrations. The simulation algorithm is shown in Figure C-12.

Inputs to the simulation include the material specific force ( $K_t$ ), the chip thickness or axial depth of cut, ( $b$ ), the feed per tooth, ( $f_t$ ), the spindle speed, the radial immersion, and the modal stiffness, natural frequency and damping ratio of the most flexible mode in two orthogonal directions. For this elementary simulation, a circular tool path and straight cutter was assumed, which is acceptable for the low axial depths of cut used in this research. Vectors *teeth* and *phi* are used to record the instantaneous teeth positions and the angle of the cutter, respectively. A vector *surf* contains the surface location left by the vibrating cutter at time steps,  $dt$ .

Figure C-9: Phasor Diagram ( $r = 1$ )Figure C-10: Phasor Diagram ( $r > 1$ )

In the main body of the program, the first step is to increment the time step and index the cutter teeth to the current angular positions. The next step is to calculate the tangential force on the cutter if the current tooth is in the cut (bounded by the angles *phistart* and *phiexit*). Otherwise, it is set to zero. The tangential force is assumed proportional to the product of the material specific force and instantaneous chip load. Previous passes (recorded in the vector *surf*), the current x and y-direction vibrations of the cutter and the current feed ( $f_i \sin \phi$ ) are used to determine the instantaneous chip load. This allows for surface regeneration. The possible non-linearity caused by a tooth jumping out of the cut during large deflections is handled by setting the magnitude of the tangential force equal to zero if a negative value for the instantaneous chip area is calculated. Next, the vector *surf* is updated and the current surface location is recorded provided a tooth is in position 1 (as shown in Figure C-1). The normal force is then calculated (see Equation 4) and the tangential and normal forces resolved into the x and y coordinate directions. This force loop is repeated for each tooth on the cutter and the forces summed. Next the cutter vibrations are calculated by Euler integration (Equation C-8) and the total loop is repeated.

$$x'' = \frac{(F_x - c_x x' - k_x x)}{m_x}$$

$$x' = x'' dt + x'$$

$$x = x + x' dt$$

$$y'' = \frac{(F_y - c_y y' - k_y y)}{m_y}, \text{ where } c_i = \text{damping coefficient}, m_i = \text{modal mass} \quad (\text{C-8})$$

$$y' = y'' dt + y'$$

$$y = y + y' dt$$

Experimental Method

An experimental part geometry was chosen, the CNC code written and down milling tests completed on a horizontal spindle 3-axis CNC machining center. The workpiece (7075-T6 aluminum) dimensions were measured using a coordinate measuring machine (CMM). The part geometry is shown in Figure C-13. This particular geometry doubles the sensitivity to surface location errors because the measurements D1 and D2 each contain two passes which contribute, theoretically, the same surface error. The surface errors, E1 and E2, can then be calculated according to Equation C-9. In this equation, a positive error indicates an undercut surface, while a negative error denotes an overcut surface. The commanded values of D1 and D2 were 95.174 mm (3.747") for a 12.776 mm (0.503") diameter cutter.

$$E1 = (D1 - 95.174)/2, \quad E2 = (D2 - 95.174)/2 \text{ (mm)} \quad (\text{C-9})$$

The first step in completing the cutting tests was to find the system natural frequencies and modal values using the impact test. A rather flexible nominally 12.7 mm (0.5") diameter, 4 flute, high speed steel (HSS) helical end mill with an 82.55 mm (3.25") overhang was chosen. The system direct transfer functions were obtained by attaching an accelerometer to the end of the tool, striking the tool in the direction of the accelerometer with an instrumented hammer and recording the two signals simultaneously. The fast Fourier transform (FFT) was calculated for each signal and the acceleration over force transfer function obtained by performing the complex division of the accelerometer FFT

over the hammer FFT. The displacement over force transfer functions were then obtained by converting the acceleration to displacement. This conversion (dividing by  $-\omega^2$  (in rad/s) at each point in the frequency domain) is shown in Equation C-10. The displacement over force transfer functions and the linear best fit for the x and y coordinate directions are shown in Figure C-14. These transfer functions show nearly identical tool modes in both directions with a stiffness of  $3.7e5$  N/m, a natural frequency of 883 Hz and a damping ratio of 0.012 (1.2%).

$$A = s^2 X, \text{ where } s = j\omega, \text{ therefore, } A = -\omega^2 X \quad (\text{C-10})$$

Once the dominant natural frequency of the tool was known, it was possible to select the experimental spindle speeds. In the case of high-speed machining, the spindle speed selected for maximum MRR would be near the system natural frequency. For this spindle speed, there is one wave of vibration per tooth ( $f_{tooth} = f_n$ ). The resonant spindle speed is selected by Equation C-11 with the number of waves set equal to one. The lower bound for the spindle speed could then be selected for two waves of vibration per tooth, or  $2f_{tooth} = f_n$ . For this range of spindle speeds, the full range between undercut and overcut would be expected for the dimensions D1 and D2.

$$\text{Spindle speed} = f_n * 60 / (vm) \text{ (rpm), where } f_n = (\text{Hz}) \quad (\text{C-11})$$

v = waves per tooth  
m = number of teeth on cutter

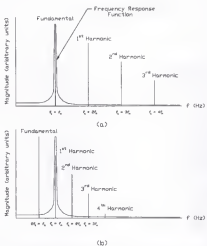


Figure C-11: Undercut/Overcut/Undercut Transition

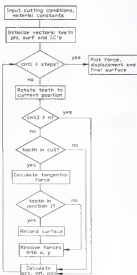


Figure C-12: Simulation Flow Diagram

For the measured natural frequency of 883 Hz, this gives a resonant spindle speed of 13245 rpm, well within the range of today's high speed/high power spindles and the proper speed to select for maximum MRR in high-speed machining. However, the CNC machine tool available for this research had a top spindle speed of 5000 rpm. In order to maximize the spindle speed and cover the full range from undercut to overcut, it was decided to select an array of 11 spindle speeds between 2.65 and 3.65 waves per tooth. The chosen spindle speeds and corresponding linear feed rates for a chip load of 0.095 mm/tooth are shown in Table C-1. This feed per tooth was chosen to maximize the available linear feed of 3 m/min at the top spindle speed.

Table C-1: Selected Speeds/Feeds

Test Number	Spindle Speed (rpm)	Linear Feed (m/min)
1	4998	2.95
2	4861	2.87
3	4724	2.80
4	4587	2.72
5	4450	2.64
6	4313	2.56
7	4177	2.48
8	4040	2.36
9	3903	2.28
10	3766	2.20
11	3629	2.13

This research was primarily concerned with finish machining operations when surface accuracy is of prime importance. The radial depth of cut for the cutting tests was therefore chosen to be 0.127 mm (0.005"), a typical finishing pass radial depth of cut in end milling operations. This corresponds to a 1% radial immersion for a nominal 12.7 mm (0.5") diameter cutter. Since the purpose of this research was to evaluate the error of

surface for stable machining, it was also necessary to choose the maximum stable depth of cut for chatter-free operation at all selected spindle speeds. A commercially available software package, which produced a peak-to-peak (PTP) force diagram, was used to select this maximum allowable depth of cut [42][44]. The resultant PTP diagram is shown in Figure C-15. The PTP diagram plots the cutting force for lines of constant axial depth of cut over a selected range of spindle speeds. Abrupt discontinuities in the force along these lines signify the onset of instability, or chatter. In Figure C-15, the top line denotes an axial depth of cut of 0.50 mm (0.0118"). Each of the lower lines represents an axial depth of cut reduced by 0.02 mm. The maximum allowable stable depth of cut over the full spindle speed range is shown to be approximately 0.28 mm. An axial depth of cut of 0.254 mm (0.010") was chosen for the cutting tests.

The CNC part program used to cut the test parts was written to minimize both controller and reversal errors and, therefore, isolate the cutting force errors. For a square path with motions in only directions parallel to the machine tool axes, the dominant controller error is overshoot or undershoot in cornering operations. In an x-y corner motion, the inherent steady-state positional error, or velocity lag, allows the x motion time to decelerate and stop prior to the start of y motion. This effectively eliminates overshoot for low controller gains, but can round the corner at higher velocities. Reversal error is caused by friction in the leadscrew and produces a positional error, or dead zone, due to a force discontinuity when the direction of motion is reversed [21].

The part program chosen minimizes the effects of both these errors by dwelling for a short period before changing cutting directions and preloading the commanded axes

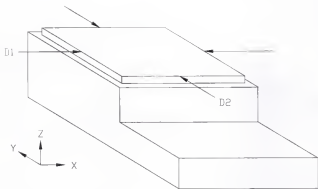


Figure C-13: Part Geometry

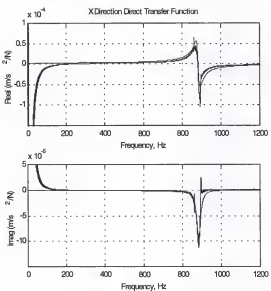


Figure C-14a: X Direction Direct Transfer Function

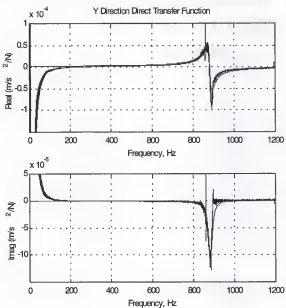


Figure C-14b: Y Direction Direct Transfer Function

before changing the direction of motion. Figure C-16 shows the path followed by the cutter for down-milling. The dwells, shown after moves 5 and 6, were implemented to remove the cornering dynamics and moves 1-4 and 8-11 represent the reversal preloads. The total NC program included two nested loops. The first, inner loop repeated the path shown in Figure C-16 a total of 7 times with a step over of 0.127 mm (0.005") in both the x and y directions between each step. The second, outer loop repeated the inner loop 12 times while increasing the axial depth of cut in the z direction by 0.254 mm (0.010") each repetition.

Another potential source of error is asynchronous error motions of the machine tool spindle and structure. If the asynchronous errors were larger than the surface location error due to cutter vibration, the cutting tests described previously could yield seemingly random results. The results would still be deterministic, however, since the spindle motions would, in this case, mask the cutting errors and produce the seemingly random results. Therefore, the grease pencil test (or single spot asynchronous motion test), a common procedure used to measure these error motions, was completed on the spindle to be used in the cutting tests [45]. In the grease pencil test, a rotating reference surface (such as a workpiece, chuck or the spindle nose) is selected. A displacement transducer, such as a capacitance probe, is then mounted perpendicular to the reference surface and fixed to ground. A high or low point (e.g., the mark left by a grease pencil) disrupts the dielectric between the probe and measurement surface once per revolution. For a perfect spindle, the capacitance voltage would be the same for each revolution. In reality, the maximum change in the peak voltage over several revolutions represents the asynchronous error at a specific angular location.

Care must be taken in digitally recording the data to prevent aliasing. The sampling rate must be at least twice the highest expected frequency (or twice the bandwidth of the displacement indicator). For these tests, a 15.011 kHz sampling rate yielded an approximate radial asynchronous error motion of 1.78  $\mu\text{m}$  (0.070e-3"). The digital record of the calibrated capacitance output is shown in Figure C-17. In this case, the asynchronous error magnitude is much smaller than the expected error due to cutter vibrations and may be neglected. However, in other situations, as noted previously, this error could completely conceal the cutting force errors.

Once the part was machined at a given spindle speed, it was removed from the machine and placed in a thermally stable environment ( $68^\circ \pm 0.2^\circ \text{ F}$ ) to soak overnight. The following day, a direct computer-control part program was executed on the CMM to measure the 2-D distances D1 and D2. The program first allowed the user to align the CMM local measurement axes with those of the part, then probed five points along each of the edges of the part to determine D1 and D2 using a 2 mm diameter probe. Direct computer-control allows the CMM controller to select the normal to the probing surface and approach each measurement point with a constant velocity. This effectively reduces the uncertainty of the measurements. Additionally, the CMM measurement program was executed sequentially 12 times. The high and low values were rejected and the other 10 averaged. A standard deviation of less than 1  $\mu\text{m}$  was typical.

#### Experimental Results

The machining and measurement of 11 total parts corresponding to the spindle speeds/feeds shown in Table C-1 were completed. The error of surface location was then

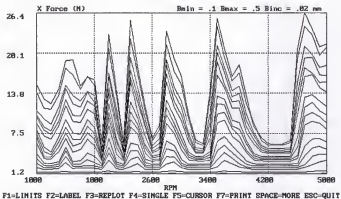


Figure C-15: PTP Force Diagram

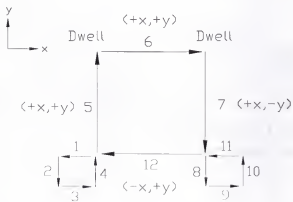


Figure C-16: NC Path

calculated according to Equation C-9. Additionally, the simulation previously described was executed for the same speeds/feeds to find the predicted error of surface location. A comparison of the experimental and simulated results for both the D1 and D2 surfaces is shown in Figure C-18.

It can be seen from Figure C-18 that the simulation results match well with the experimental data at speeds of 4313 rpm and above. The predicted overcut to undercut can be seen in both the simulated and D1 surface data with the maximum undercut at 4450 rpm (near the second harmonic of resonance). The D2 surface data shows a probable anomaly at the 4450 rpm spindle speed, but good agreement with the D1 data otherwise. The good experimental agreement between the two surface errors is reassuring since the x and y-direction system dynamics were equal, so the errors should be the same. The discrepancy between the simulated and experimental results at spindle speeds below 4313 rpm (which appears to be a simple offset except at 3766 rpm) could have resulted from several procedural limitations. First, only one part was machined at each spindle speed so the process uncertainty is unknown. Second, only one part was machined per day over an 11 day period. The total shop temperature variation (for the machining environment) was significant over this time period, but the measuring environment was kept at a constant temperature of 68° F. Finally, the end mill was removed after each test, so the part could be faced with a separate tool (to limit wear). Therefore, the positioning repeatability of the spindle collet becomes a factor.

Although the simulation and experimental results do not match perfectly, a large variation in the surface location error is recognized over the range of spindle speeds tested in both data sets. A total experimental variation in surface location error of 50  $\mu\text{m}$

(0.002") is shown over the range of spindle speeds for the surfaces under identical cutting conditions using the same NC program. In certain finish machining applications, this is an unacceptable error magnitude. It can also be seen that at spindle speeds of 3770 and 4520 rpm for D1 and 3890 and 4300 rpm for D2 there is no error. Selection of these speeds would produce a part with no error of surface introduced by the cutting operation, even for this flexible tool.

In order to see the effect of spindle speed over a larger range, simulations were executed using the same cutting conditions, tool dynamics, and an assumed spindle speed range of 1000-15000 rpm. These results are shown in Figure C-19. The periodic variation of overcut to undercut can be seen in the figure. The forcing function harmonics are also marked (i.e., 2 represents the second harmonic where  $3f_{\text{root}} = f_a$ ). It is important to note the magnitude of change in surface location possible by a simple change in spindle speed. For a change in spindle speed from 1950 to 6623 rpm, for example, a change in surface location error of 70  $\mu\text{m}$  (0.0028") is predicted. This result may be equal to or bigger than the effect of typical individual error sources (i.e., geometric and thermal errors). Perhaps more importantly, it can be seen in Figure C-19 that at tooth passing frequencies near harmonics of the system natural frequency, a small change in spindle speed results in a large change in surface location error. For example, a change in spindle speed from 6623 (first harmonic) to 7200 rpm will cause a change in surface location error of 53  $\mu\text{m}$ . Both speeds provide stable cutting conditions. However, due to a change in the phasing of the cutter vibrations, the surface location varies significantly.

As noted, the cutting tool used in this research was quite flexible. In other situations, a less flexible tool, with a different frequency response function, might be used.

As an example, consider a 4 flute, 0.75" diameter, helical HSS end mill with a 1.5" overhang and a higher natural frequency than the previous tool (1200 Hz), approximately three times the stiffness (1e6 N/m) and 1% damping in both the x and y directions. The simulations shown in Figure C-19 were once again executed, but with these new modal values for the machine/tool system. The results are shown in Figure C-20. Once again, the periodic undercut/overcut variation can be seen, but now at different harmonic frequencies. It can also be seen that the overall magnitude of undercut to overcut is now smaller due to the less flexible tool.

### Conclusions

The effect of spindle speed and the system frequency response function on the surface location error in finish machining has been explored. Cutting tests have been performed over a range of spindle speeds corresponding to a full range of surface location errors from overcut to undercut ( $2.65f_{loop} = f_a$  to  $3.65f_{loop} = f_b$ ) for a given tool and stable cutting conditions. Simulations have also been completed and good agreement found between the simulated and actual data over a limited spindle speed range. Further cutting tests, which include several tools and various materials and cutting conditions, will be necessary to fully explore this phenomenon. Although not a definitive work, this research demonstrates a significant dependence of the surface location error on spindle speed. Furthermore, it has been observed that a relatively small change in spindle speed can produce a large variation in the final surface location (and part dimensions), especially at speeds near integer multiples of the system natural frequency. This research shows that both system natural frequency and flexibility are important considerations, especially in

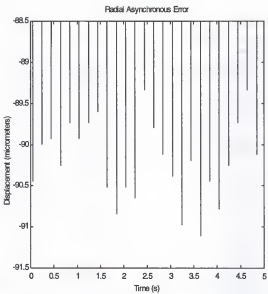


Figure C-17: Radial Asynchronous Error

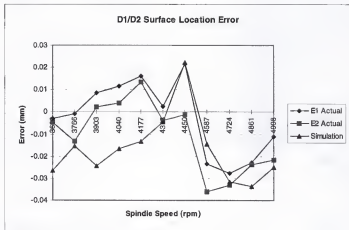


Figure C-18: D1/D2 Surface Location Error

high-speed machining where the tooth passing frequency is set near the natural frequency (resonance) to maximize the stable depth of cut.

Although this research concentrated on the surface location error due to cutter vibrations, this is only one error source within the machining process. Other sources, such as geometric, thermal or hysteresis errors, may dominate in a given situation. For example, in the machining center used in this research, a large reversal error was present in the x-axis while virtually no reversal error occurred for the y-axis (controller compensation was turned off for the experiments). If the NC path included an x-direction reversal without a corresponding preload to remove this error, the x reversal error would have increased the D1 surface dimension by the magnitude of this error. Additionally, for a non-symmetric part, thermal growth of the spindle in the radial direction would affect the part's final dimensions. Finally, although the dynamics of the cutting process have been modeled and tested, material removal also introduces heat into the system. Therefore, thermal effects are not easily decoupled from the cutting process. In short, all errors in the machine tool, including the dynamic cutting errors, must be accounted for and compensated if highly accurate parts are to be manufactured.

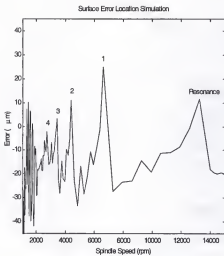


Figure C-19: Full Range Simulation (0.5" diameter tool, 3.25" overhang)

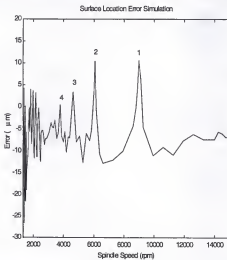


Figure C-20: Full Range Simulation (0.75" diameter tool, 1.5" overhang)

## REFERENCES

1. Bothe, D. Measuring Process Capability. New York: McGraw-Hill, 1997.
2. Kotz, S., and N. Johnson. Process Capability Indices. New York: Chapman & Hall, 1993.
3. Ziegert, J.C., and C.D. Mize. "Laser ball bar: A new instrument for machine tool metrology." *Precision Engineering* 16, no. 4 (October 1994): 259-67.
4. Mize, C.D., J.C. Ziegert, R. Pardue, and N. Zucker. "Spatial Measurement Accuracy Tests of the Laser Ball Bar." Final Report for CRADA No. Y-1293-02244 between Martin Marietta Energy Systems and Tetra Precision, Inc. August 1994.
5. ASME B5.54. "Methods for Performance Evaluation of Computer Numerically Controlled Machining Center." New York, 1992.
6. Kulkarni, R. "Design and Evaluation of a Technique to Find the Parametric Errors of a Numerically Controlled Machine Tool Using a Laser Ball Bar." M.S. thesis, University of Florida, Gainesville, FL, 1996.
7. Srinivasa, N. "Modeling and Prediction of Thermally Induced Errors in Machine Tools Using a Laser Ball Bar and a Neural Network." Ph.D. dissertation, University of Florida, Gainesville, FL, 1994.
8. Schmitz, T. "Machining Virtual Test Parts." M.S. thesis, University of Florida, Gainesville, FL, 1996.
9. Postlethwaite, S., D. Ford, and D. Morton. "Geometric errors from dynamic data- a novel calibration technique." *Laser Metrology and Machine Performance* 2 (1995): 139-48.
10. Postlethwaite, S., D. Ford, and D. Morton. "Dynamic calibration of CNC machine tools." *International Journal of Machine Tools and Manufacturing* 37, no. 3 (1997): 287-94.
11. Rehsteiner, F., and S. Wiekert. "Analysis of tool trajectories (2D paths) in machine tools." Proceedings of the ASPE 1996 Annual Meeting, Monterey, CA (1996): 288-93.

12. Zirn, O., and S. Weikert. "Dynamic accuracy monitoring for the comparison and optimization of fast axis feed drives." *Proceedings of the ASPE 1997 Annual Meeting*, Norfolk, VA (1997): 323-27.
13. Chen, J., and C. Ling. "Improving the machine accuracy through machine tool metrology and error correction.", *International Journal of Manufacturing Technology* 11, no. 3 (1996): 198-205.
14. Hong, S., Y. Shin, and H. Lee. "An efficient method for identification of motion error sources from circular test results in NC machines." *International Journal of Machine Tools and Manufacturing* 37 (1997): 327-40.
15. Musinski, D. "Interferometric metrology: linear and angular displacement." Tutorial at the 1997 Annual Meeting of the American Society for Precision Engineering, Norfolk, VA (October 1997).
16. Sears, F., M. Zemansky, and H. Young. College Physics. 7<sup>th</sup> ed. New York: Addison-Wesley, 1991.
17. Pedrotti, F., and L. Pedrotti. Introduction to Optics. 2<sup>nd</sup> ed. Englewood Cliffs, NJ: Prentice-Hall, 1993.
18. Feynman, R. QED The Strange Theory of Light and Matter. Princeton: Princeton University Press, 1985.
19. Selberg, L. "Interferometric Metrology: An Introduction." Tutorial at the 1994 Annual Meeting of the American Society for Precision Engineering, Cincinnati, OH (October 1994).
20. Johnson, B. Optics and Optical Instruments. New York: Dover, 1960.
21. Slocum, A. Precision Machine Design. Englewood Cliffs, NJ: Prentice-Hall, 1992.
22. Thomson, W. Mechanical Vibrations. 2<sup>nd</sup> ed. Englewood Cliffs, NJ: Prentice-Hall, 1958.
23. Beckwith, J. Personal conversations at Lawrence Livermore National Laboratory, Livermore, CA (May-August, 1997).
24. "Projects in Fiber Optics: Companion Applications Handbook." Newport Model #FKP, Newport Corporation, Irvine, CA, 1988.
25. Sezerman, O., and G. Best. "Accurate alignment preserves polarization." *Laser Focus World* 33, no. 12 (December 1997): S27-S30.

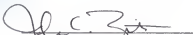
26. Srivastava, R. "EEL 4445: Class Notes." University of Florida, Gainesville, FL, Spring 1998.
27. Mize, C.D. "Design and Implementation of a Laser Ball Bar Based Measurement Technique for Machine Tool Calibration.", M.S. thesis, University of Florida, Gainesville, FL, 1993.
28. Steinmetz, C. "Sub-micron position measurement and control on precision machine tools with laser interferometry.", *Precision Engineering* 12, no. 1 (January 1990): 12-24.
29. Elden, B. "The Refractive Index of Air." *Metrologia* 2, no. 2 (1966): 71-80.
30. Operating Manual for the PTB100A Analog Barometer (PTB100-U157en-1.1). Vaisala Inc., Helsinki, Finland. December 1995.
31. Axiom 2/20 Laser Measurement System Operation and Reference Manual OMP-0220G. Zygo Corp., Middlefield, CT. September 1991.
32. Avallone, E., and T. Baumeister. Marks' Standard Handbook for Mechanical Engineers. 9<sup>th</sup> ed. New York: McGraw-Hill, 1987.
33. Boresi, A., R. Schmidt, and O. Sidebottom. Advanced Mechanics of Materials. 5<sup>th</sup> ed. New York: John Wiley, 1993.
34. Shigley, E. Mechanical Engineering Design. 2<sup>nd</sup> ed. New York: McGraw-Hill, 1972.
35. Mize, C.D. "Automatic Tool Trajectory Assessment and Correction System." National Science Foundation Phase I Final Report, Award #III-9360797 (June 1994): 18-20.
36. Schmitz, T. "Ball-Socket Joint Coefficient of Friction Measurement." Proceedings of the 1997 ASME Southeast Region XI Graduate Student Technical Conference, University of South Alabama, Mobile, AL (May 16-17, 1997): 12-14.
37. Thusty, J. "Class Notes EML 6934: Fundamentals of Production Engineering Part 2." University of Florida, Fall Semester 1994.
38. ACCOM User's Manual. Heidenhain Corporation, Schaumburg, IL (September 1996): 143-60.
39. Schmitz, T., and J. Ziegert. "Premachining Computer Numerical Control Contour Validation." *Precision Engineering* 22, no. 1 (January 1998): 10-18.
40. Chau, W. "Accuracy of Milling Operations Based on Dynamic Models and Simulations." M.S. thesis, University of Florida, Gainesville, FL, 1992.

41. Smith, S. "Chatter, Forced Vibrations, and Accuracy in High Speed Milling." M.S. thesis, University of Florida, Gainesville, FL, 1985.
42. Smith, S., and J. Tlusty. "Current Trends in High Speed Machining." *Journal of Manufacturing Science and Engineering* 119 (November 1997): 664-66.
43. Tlusty, J. "Cutting Tests: Report Presented to the ASME B5 Committee." 1990 ASME B5 Committee Meeting (January 15, 1990): 8-9.
44. User's Manual: MILSIM Version 2.0. Manufacturing Laboratories, Inc., Gainesville, FL, 1992.
45. Draft Revision of "ASME/ANSI B89.3.4: Dimensional Metrology - Axes of Rotation Standard." February 1998.
46. Hocken, R. "Machine Tool Metrology." Tutorial at the American Society for Precision Engineering 9<sup>th</sup> Annual Meeting, Cincinnati, OH (October 1994).
47. Blaedel, K.L. "Error reduction." in Technology of Machine Tools. Vol. 5: Machine Tool Accuracy. University of California, Livermore, CA, UCRL-52960-6 (October 1980).
48. "Software Correction of Precision Machines." A Report from the Precision Engineering Laboratory at UNC Charlotte to the National Institute of Standards and Technology. NIST-60NANB2D1214. July 1993.
49. Altintas, Y., and E. Budak. "Analytical Prediction of Stability Lobes in Milling." *Annals of CIRP* 44, no.1 (1995).

### BIOGRAPHICAL SKETCH

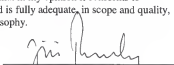
The author was born in El Paso, TX, in 1970. After finishing his high school education in the Midwest, he traveled to North Philadelphia to pursue his undergraduate degree in Mechanical Engineering at Temple University. At Temple, he was a two-time Academic All-American, named to the Inaugural College Football Association Student-Athlete Team and was the top graduate in the TU School of Engineering. After graduation, the author tried his hand at coaching (long hours/little pay) and environmental engineering (surprisingly dirty) before returning to graduate school at the University of Florida in 1994 under a fellowship sponsored by the National Science Foundation. He was awarded his Master of Science degree in 1996 and remained at UF to pursue his Ph.D. His final year of graduate study was funded by the "Integrated Manufacturing Predoctoral Fellowship" sponsored by the Department of Energy/National Academy of Engineering. After his four-plus years as a graduate student, the author plans to return to society and lead a productive life.

I certify that I have read this study and that in my opinion it conforms to acceptable standards of scholarly presentation and is fully adequate, in scope and quality, as a dissertation for the degree of Doctor or Philosophy.



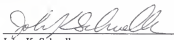
John C. Ziegert, Chairman  
Associate Professor of Mechanical  
Engineering

I certify that I have read this study and that in my opinion it conforms to acceptable standards of scholarly presentation and is fully adequate, in scope and quality, as a dissertation for the degree of Doctor or Philosophy.



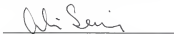
Jiri Tlusty  
Graduate Research Professor of  
Mechanical Engineering

I certify that I have read this study and that in my opinion it conforms to acceptable standards of scholarly presentation and is fully adequate, in scope and quality, as a dissertation for the degree of Doctor or Philosophy.



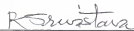
John K. Schueler  
Associate Professor of Mechanical  
Engineering

I certify that I have read this study and that in my opinion it conforms to acceptable standards of scholarly presentation and is fully adequate, in scope and quality, as a dissertation for the degree of Doctor or Philosophy.



Ali Seireg  
Ebaugh Professor of Mechanical  
Engineering

I certify that I have read this study and that in my opinion it conforms to acceptable standards of scholarly presentation and is fully adequate, in scope and quality, as a dissertation for the degree of Doctor or Philosophy.

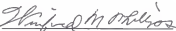


---

Ramakant Srivastava  
Professor of Electrical  
Engineering

This dissertation was submitted to the Graduate Faculty of the College of Engineering and to the Graduate School and was accepted as partial fulfillment of the requirements for the degree of Doctor of Philosophy.

May 1999



---

Winfred M. Phillips  
Dean, College of Engineering

---

M. J. Ohanian  
Dean, Graduate School

, \$355

LD  
1780  
1999

UNIVERSITY OF FLORIDA



3 1262 08554 4749